Anisotropic hard magnetic nanoparticles and nanoflakes obtained by surfactant-assisted ball milling

DISSERTATION

zur Erlangung des akademischen Grades

Doktor-Ingenieur
(Dr.-Ing.)

Vorgelegt

der Fakultät Maschinenwesen der Technischen Universität Dresden

von

Santosh Kumar Pal
geboren am 10.07.1985 in Ghatampur, Indien

Dresden 2015

Gutachter: Prof. Dr. L. Schultz
Prof. Dr. J. Freudenberger

Eingereicht am: 27.08.2014

Tag der Verteidigung: 23.11.2015

Abstract

The research work in this thesis has been devoted to understand the formation mechanism of single-crystalline and textured polycrystalline nanoparticles and nanoflakes of $SmCo_5$ and $Nd_2Fe_{14}B$ prepared by surfactant-assisted (SA) ball milling and to study their microstructural and magnetic properties. The nanoparticles and nanoflakes are promising candidates to be used as hard magnetic phase for the fabrication of high-energy-density exchange-coupled nanocomposite magnets. The influence of a range of different surfactants, solvents and milling parameters on the characteristics of ball-milled powder has been systematically investigated. Small fraction (~10 wt.%) of $SmCo_5$ nanoparticles of average diameter 15 nm along with textured polycrystalline nanoflakes of average diameter 1 μm and average thickness of 100 nm were obtained after SA – ball milling of $SmCo_5$ powder. Isolated single-crystalline particles (200-500 nm) and textured polycrystalline flakes (0.2-1.0 μm) of $Nd_2Fe_{14}B$ have been prepared in bulk amount (tens of grams), after SA – ball milling of dynamic-hydrogen-disproportionation-desorption-recombination (d-HDDR) processed $Nd_2Fe_{14}B$ powder. These single-crystalline $Nd_2Fe_{14}B$ particles are promising for their microstructure for the fabrication of exchange-coupled nanocomposite permanent magnets.

The $SmCo_5$ and $Nd_2Fe_{14}B$ flakes and particles were well aligned in magnetic field: the former showed [*001*] out-of-plane orientation while the latter showed [*001*] in-plane orientation. A maximum degree of texture values of 93 % and 88 % have been obtained for the magnetically-oriented $SmCo_5$ flakes and $Nd_2Fe_{14}B$ single-crystalline particles, respectively. SA – ball milling resulted in an increase of coercivity of $SmCo_5$ particles from 0.45 T for un-milled powder to a maximum value of 2.3 T after 1 h of milling, further milling resulted in a decrease of the coercivity. The coercivity of SA – ball-milled $Nd_2Fe_{14}B$ particles decreased drastically from 1.4 T for un-milled d-HDDR powder to 0.44 T after 0.5 h of milling, isolated single-crystalline particles (200-500 nm size) obtained after 4 h of SA – ball milling showed a coercivity of 0.34 T. The drastic decrease in coercivity of ball-milled $Nd_2Fe_{14}B$ particles is attributed to the morphological change because the demagnetization in $Nd_2Fe_{14}B$ magnets is governed by nucleation mechanism. A remarkable enhancement in coercivity from 0.26 T to 0.70 T for ethanol-milled sample and from 0.51 T to 0.71 T for oleic-acid-milled samples has been obtained after an optimum heat-treatment at 400 ^{0}C. An increase of α-Fe and Nd_2O_3 phase contents and a sharp change of lattice parameter *c* of $Nd_2Fe_{14}B$ was observed when heat-treating above 400 ^{0}C. The change in lattice parameter at higher temperature is thought to be due to partial substitution of carbon atoms present in the surfactant or solvent, for boron atoms.

Kurzfassung

Das Ziel dieser Arbeit ist es, den Mechanismus der Herstellung von einkristallinen und texturierten polykristallinen Nanopartikeln und Nanoflakes aus $SmCo_5$ und $Nd_2Fe_{14}B$ durch Tensid-gestütztes Kugelmahlen zu verstehen. Des Weiteren soll deren Gefüge und magnetische Eigenschaften untersucht werden. Die Nanopartikel sind vielversprechende Kandidaten zur Verwendung als hartmagnetische Phase in hochentwickelten, austauschgekoppelten Nanokomposit-Magneten.

Der Einfluß der Art der verwendeten Tensid, Lösungsmittel sowie Mahlparameter auf die Eigenschaften der kugelgemahlenen Pulver wurde systematisch untersucht. Ein kleiner Anteil (~10 m.%) von $SmCo_5$ Nanopartikeln mit mittlerem Durchmesser von 15 nm zusammen mit texturierten polykristallinen Plättchen mit mittlerem Durchmesser von 1 μm und mittlerer Dicke von 100 nm wurden nach Tensid-gestütztes Kugelmahlen erzeugt. Alleinstehende einkristalline Partikel (200-500 nm) und texturierte polykristalline Plättchen (0,2-1,0 μm) aus $Nd_2Fe_{14}B$ wurden in größeren Mengen (einige 10 g) hergestellt. Das verwendete Ausgangspulver wurde hierbei durch dynamisches-Hydrierung-Disproportionierung-Desorption-Rekombination (d-HDDR) hergestellt und anschließend Tensid-gestütztes Kugelmahlen. Die genannten einkristallinen $Nd_2Fe_{14}B$ Partikel sind ebenfalls vielversprechend als hartmagnetischer Bestandteil von austauschgekoppelten Nanokomposit-Magneten.

Die $SmCo_5$- und $Nd_2Fe_{14}B$-Plättchen und -Partikel wurden alle in einem Magnetfeld ausgerichtet: erstere zeigten aus der Ebende herauszeigende und letztere in der Ebene liegende [*001*]-Orientierung. Ein maximaler Texturgrad von 93% wurde für im Magnetfeld ausgerichtete $SmCo_5$ flakes bzw. 88% für einkristalline $Nd_2Fe_{14}B$ Partikel erzielt. Tensid-gestütztes Kugelmahlen führte zu einem Anstieg der Koerzitivfeldstärke von $SmCo_5$ Partikeln von 0,45 T für ungemahlenes Pulver auf 2,3 T nach einer Mahldauer von 1 h. Weiteres Mahlen führte zu einem Abfall der Koerzitivfeldstärke. Die Koerzitivfeldstärke von Tensid-gestütztes Kugelmahlen $Nd_2Fe_{14}B$ Partikeln verringerte sich stark von 1,4 T von ungemahlenem d-HDDR Pulver auf 0,44 T nach 0,5 h Mahlen. Freistehende einkristalline Partikel (200-500 nm groß), welche nach 4 h Tensid-gestütztes Kugelmahlen erhalten wurden, zeigten eine Koerzitivfeldstärke von 0,34 T. Der starke Abfall der Koerzitivfeldstärke von gemahlenen $Nd_2Fe_{14}B$ Partikeln wird die morphologischen Veränderungen zurückgeführt, da die Ummagnetisierung nukleationsgesteuert ist. Ein bemerkenswerter Anstieg der Koerzitivfeldstärke von 0,26 T auf 0,70 T wurde für eine in Ethanol gemahlene Probe verzeichnet, sowie ein Anstieg von 0,51 auf 0,71 T für eine Probe, welche mit einer Zugabe

von Oleinsäure gemahlen wurde. Beide Proben wurden einer optimierten Wärmebehandlung bei 400°C unterzogen. Bei höheren Temperaturen wurde für $Nd_2Fe_{14}B$ ein Anstieg der Menge an α-Fe und Nd_2O_3 gefunden und eine sprungartige Veränderung des Gitterparameters c der $Nd_2Fe_{14}B$ Phase. Die Veränderung des Gitterparameters wird auf die partielle Substitution von Kohlenstoffatomen des Tensid oder Lösungsmittels gegen Boratome zurückgeführt.

Table of contents

List of symbols and abbreviations

μ_0	vacuum permeability
M_S	saturation magnetization
H_C	coercivity
D	diameter
D_c	critical single domain size
S	domain wall thickness
E_a	magnetocrystalline free energy
E_{str}	stray field energy
V	volume
$\mathcal{H}_C$	coulomb interaction
$\mathcal{H}_{SO}$	spin orbit interaction
$\mathcal{H}_{C\mathcal{F}}$	crystal field Hamiltonian
S	spin angular momentum
L	orbital angular momentum
J	total angular momentum
g	gyromagnetic ratio
γ	domain wall energy
A	exchange constant
K	anisotropy constant
H_{demag}	demagnetization field
$\mathcal{N}$	demagnetization tensor
T	tesla
T_C	curie temperature
T_{SR}	spin reorientation temperature
HDDR	Hydrogen-disproportionation-desorption-recombination
d-HDDR	dynamic-hydrogen-disproportionation-desorption-recombination
RE	rare-earth
RETM	rare-earth transition metal

SA	surfactant-assisted
XRD	X-ray diffraction
SEM	scanning electron microscopy
HRSEM	high-resolution scanning electron microscopy
TEM	transmission electron microscopy
HRTEM	high-resolution transmission electron microscopy
SAED	selected area electron diffraction
FFT	fast furrier transform
VSM	vibrating sample magnetometry
SQUID	superconducting quantum interface device
PPMS	physical property measurement systems

Introduction

High-energy-density permanent magnets are requisite materials for wide range of applications from energy conversion devices (*e.g.* motors, loud speakers, and electric generators and alternators), household appliances and cell phones to recent environmentally-friendly technologies such as hybrid electric vehicles and wind turbines [*Low10, Gut11*]. In addition to the requirement of high-energy-density permanent magnets, there is a great need to minimize the content of critical rare-earth elements in these magnets. The reduction of rare-earth elements is essential because of very limited resources which has resulted in increased and still fluctuating prices of these elements [*Doe11, Eur14*]. Further the processing and purification of ores containing rare-earth elements are very energy consuming and leave some toxic compounds which have serious environmental consequences [*Hur10*]. The nanocomposite exchange-coupled permanent magnets which in principle can be prepared by combining the ultrafine hard magnetic particles (studied in this thesis) with the soft magnetic nanoparticles would be beneficial for both increase of the energy-density of permanent magnets and the decrease of the content of rare-earth elements used in the magnets.

Nanometer-scale materials have attracted considerable interest in the last decade because of their unusual properties. The properties of materials consisting of nanometer-sized particles/grains are significantly different from those of bulk because of size and surface/interface effects. This phenomenon is of significant importance not only for scientific understanding of materials, but also for technological usage to fulfill the requirement for miniaturizing the electrical devices. The size dependence of coercivity of magnetic materials is very interesting. According to this behavior, the coercivity of powdered magnets increases with the reduction of particle size, going through a maximum and finally becoming zero for ultrafine particles due to thermal effects [*Her90, Kod99*].

Recent years saw increasing demand for nanometer-/sub-micrometer-sized single-crystalline or textured hard magnetic particles based on the rare-earth transition metal (RETM) compounds [*Sko93*]. These highly textured ultrafine particles are very good candidates to be used as precursors for the bottom-up fabrication of future high-energy-density anisotropic exchange-coupled nanocomposite permanent magnets, also termed as the next generation permanent magnets [*Had94, Zha07*]. Some bottom-up approaches, *e.g.* gas-phase-condensation and sputtering techniques, have been used to prepare exchange-coupled nanocomposite magnets [*Rui08, Zen02, Cha11*]. However, these methods are suitable only for very small scale manufacturing. Nanocomposite magnets in principle can be fabricated by combining a separately-prepared nanometer-sized magnetically-soft phase with an ultrafine single-crystalline or textured-polycrystalline magnetically-hard phase [*Bal12, Liu11, Lew14*]. Conventional top-down methods such as mechanical alloying, rapid solidification followed by hot-compaction used for the bulk production of permanent magnets do not provide enough control over the texture and distribution of soft and hard phases [*Ron10b, Ron11, Bol02*]. The alternative, a bottom-up approach, which employs the mixture of separately prepared ultrafine single-crystalline and textured hard phase and nanometer-sized soft phase, has a possibility of superior control over phase distribution and texture by using magnetic alignment and hot-compaction.

However, fabrication of nanometer-/sub-micrometer-sized particles with precise control over size, size distribution and phase purity has always been very challenging. Most of the studies published so far on magnetically-hard nanocrystalline intermetallic compounds are focused on polycrystalline samples made *via* mechanical alloying and ball milling [*Kir96, Lee08*]. Chemical solution method, the most versatile way of controlling the size and shape of nanoparticles, is well studied for the preparation of FePt hard magnetic nanoparticles [*Nan07, Wan07a, Elk05*]. But because of the complex crystal structure of RETM and the high reactivity of rare-earth elements, the chemical solution method is not an efficient route for the preparation of RETM nanoparticles. One of the approaches for preparation of hard magnetic nanoparticles is by surfactant-assisted ball milling, which involves milling of RETM powder in the presence of surfactant and solvent [*Akd10, Cui10, Gab10, Cui11, Wan07b, Che11*]. The use of surfactants during ball milling provides a capping layer over the particles which decreases inter-particle friction, reduces the re-welding between particles, and yields particles with high shape and crystalline anisotropy. During the novel surfactant-assisted ball milling process, as soon as the particles and/or fresh surfaces are formed, surfactants are adsorbed on to the surface of the particles, which prevents agglomeration. This action greatly reduces re-welding of crushed particles, which finally allows separated particles with smaller sizes to be formed. The most important factor facilitating the nanoparticle formation is the compatibility of the surfactant used in the ball milling process. Polarity (the dielectric constant) of the liquid environment, type and amount of the surfactants and milling energy are some of the important factors influencing the milling process. Ultrafine single-crystalline particles and textured polycrystalline nanoflakes of RETM intermetallic compounds of size ranging from 10 nm to 3 μm have been prepared by surfactant-assisted ball milling. Nanoparticles and small nanoflakes of various sizes can be separated using a size-selection process by employing ultra-sonication, however, the fraction of these nanoparticles and small nanoflakes obtained after size-selection process is low (< 20 wt.% of the as-milled sample).

This thesis focuses on two RETM intermetallic compounds, $SmCo_5$ and $Nd_2Fe_{14}B$. The powder particles of these compounds were ball-milled with surfactants and/or solvents in an inert gas atmosphere and structural, morphological and magnetic properties were investigated by using different characterization techniques. A detailed investigation of the fabrication mechanism, microstructural and magnetic properties of micrometer-/nanometer-sized single-crystalline and textured polycrystalline particles and flakes of $SmCo_5$ and $Nd_2Fe_{14}B$ produced by a novel technique, surfactant-assisted ball milling, is presented in Chapter 3. Spin reorientation, a temperature induced magnetic phase transition characterized by a temperature where magnetization starts deviating from the easy-axis, is an important property of $Nd_2Fe_{14}B$ magnets. The spin reorientation temperature of surfactant-assisted ball-milled ultrafine $Nd_2Fe_{14}B$ particles and its dependence on the intergrain exchange-coupling is discussed in chapter 3. Chapter 4 is focused on the study of the influence of different milling parameters such as polarity of solvents, type and amount of surfactants and milling energy on structural, morphological and magnetic properties of ball-milled samples. The study in this chapter was performed to optimize the milling parameters to obtain powders of desired properties. Heat-treatment and hot-compaction studies of surfactant-assisted ball-milled powders are discussed in Chapter 5. The study of processing parameters is crucial in order to understand the behavior of SA – ball-milled powders prior to hot-compaction with nanometer-sized hard magnetic particles. Chapter 6 provides a summary and critical assessment of the achievements of this work and suggestions for future work.

Chapter 1

Fundamentals

1.1 Basics of Magnetism

To appreciate magnetism one must first realize the connection between electricity and magnetism. In an electromagnet a magnetic field is created in a coil while a current flows through a wire. In an ordinary bar magnet the magnetic field created is associated with the motions and interactions of its electrons orbiting the nucleus. The electron provides two sources of magnetism in solids, originating from orbital and spin motions [*Cal07, Coe10*]. Thus each electron in an atom may be thought of as being a small permanent magnet having orbital and spin magnetic moments (figure 1.1).

The magnetic moment is quantized in units of the *Bohr magneton (μ_B)* which is the magnitude of the elementary magnetic dipole moment of an orbiting electron with an orbital angular momentum of h/2π.

$$\mu_B = \frac{eh}{4\pi m_e} = 9.274 \times 10^{-24}\ \text{Am}^2 \tag{1.1}$$

For each electron in an atom, the spin magnetic moment is $\pm\mu_B$ (+ for spin up and – for spin down). According to *Pauli's Exclusion Principle,* two identical fermions (particles with half-integer spin) cannot occupy the same quantum state simultaneously. In the case of electrons, it can be stated as follows: it is impossible for two electrons of a poly-electron atom to have the same values of the four quantum numbers (n, ℓ, m_ℓ and m_s). For two electrons residing in the same orbital, n, ℓ, and m_ℓ are the same, so m_s must be different and the electrons have opposite spins [*Kit46*]. The orbital and spin magnetic moments of these anti-parallel electron pairs cancel each other and therefore the net magnetic moment for completely-filled inner electron shells in atoms and pairs of valence electrons in bonds is zero. Solid-state magnetism originates from the partly-filled inner electron shells of transition metal atoms. Of particular importance are the 3*d* iron-series elements, in particular Fe, Co, and Ni, and the 4*f* rare-earth elements, such as Nd, Sm, Gd, and Dy. On the other

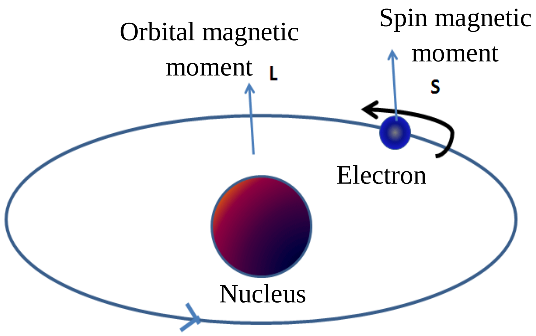

Figure 1.1 Demonstration of orbital and spin motion of an electron in an atom and associated magnetic moments.

hand, 4*d* palladium-series elements, 5*d* platinum-series elements, and actinide elements, such as U, have a magnetic moment in suitable crystalline environments [*Sko01*].

The moments of electrons in a multi-electron atom or ion are coupled by electrostatic interactions and by spin-orbit interactions. These are represented by the single-ion hamiltonians $\mathcal{H}_C$ (Coulomb interaction) and $\mathcal{H}_{SO}$ (spin-orbit interaction) respectively. The ground state is given empirically by *Hund's Rules.* The first rule is the maximization of the spin angular momentum, which yields a total quantum number ***S***. The second rule is maximization of the orbital angular momentum remaining consistent with the first rule so as to yield an orbital quantum number ***L***. Finally, ***L*** and ***S*** couple to form ***J*** (total angular moment), so that $\boldsymbol{J} = \boldsymbol{L} + \boldsymbol{S}$ if the shell is more than half full and $\boldsymbol{J} = \boldsymbol{L} - \boldsymbol{S}$ if the shell is less than half full. The magnetic moment of atom or ion is given by $g\mu_B\boldsymbol{J}$, where, $g = 1.5 + \{S(S+1)-L(L+1)\}/\{2J(J+1)\}$ is called the gyromagnetic ratio. This procedure works well for free ions or atoms. However, when the ion is incorporated in a solid the Hamiltonian has a crystal-field term $\mathcal{H}_{Cf}$ which represents the electrostatic interaction with the surrounding atoms, and can be written as $\mathcal{H} = \mathcal{H}_C + \mathcal{H}_{SO} + \mathcal{H}_{CF}$. For the rare-earth elements, $\mathcal{H}_{SO} >> \mathcal{H}_{Cf}$ so the magnetic ground state is just that predicted by *Hund's Rule* for the free ion. Both the angular and spin moments are incorporated in this case. For the *d*-block elements, the situation is reversed, $\mathcal{H}_{SO} << \mathcal{H}_{Cf}$ and the atomic current loops are disrupted by the electrostatic potential $\mathcal{H}_{Cf}$ whose gradient is the crystal electrostatic field. This disruption means that the angular momentum is quenched and the resulting moment is just due to the unpaired spins [*Sko99*]. As, for example, in Barium hexaferrite ($BaO.6Fe_2O_3$), the most used (by mass) material to make permanent magnets, the orbital magnetic moment is totally quenched. In case of $Nd_2Fe_{14}B$, which has the largest market in permanent magnetic materials, the Nd orbitals magnetic moment survives (is not quenched), but it has only a small contribution to the total magnetic moment of the compound [*Sko99, Chi97, Cul72*].

1.2 Types of magnetic materials

All materials show some type of magnetic behavior; the magnetic behavior depends on the response of electron and atomic magnetic dipoles to the application of an external magnetic field. Major types of magnetism include diamagnetism, paramagnetism, and ferromagnetism; in addition, antiferromagnetism and ferrimagnetism are sub classes of ferromagnetism. Elements classified as ferromagnetic are more commonly known as magnetic materials.

Diamagnetic

A diamagnetic material is a substance that exhibits negative magnetism in response to a positive magnetic field. Even though it is composed of atoms which have no net magnetic moment, it reacts in a particular way to an applied field. Electrons which constitute a closed shell in an atom usually have their spin and orbital moments oriented so that the atom as a whole has zero net moment. Diamagnetic substances show very small negative susceptibility. The monoatomic rare gases He, Ne, Ar etc., most polyatomic gases, such as H_2, N_2, etc., and the ionic solids like NaCl which have closed-shell electronic structures are diamagnetic [*Cal07*].

Paramagnetic

The atoms or molecules of a paramagnetic substance have net orbital or spin magnetic moments that are capable of being aligned in the direction of an applied magnetic field. They therefore have a positive (but small) susceptibility. Paramagnetism occurs in all atoms and molecules with unpaired electrons; *e.g.* free atoms, free radicals, and compounds of transition metals containing ions with unfilled electron shells. It also occurs in metals as a result of the magnetic moments associated with the spins of the conducting electrons. Paramagnetism is the tendency of the atomic magnetic dipoles to align with an external magnetic field. In pure paramagnetism, the external magnetic field acts on each atomic dipole independently and there are no interactions between individual atomic dipoles. Such paramagnetic behavior can also be observed in ferromagnetic materials that are above their Curie temperature *[Web10]*. Beyond Curie paramagnetism, based on the individual atomic magnetic moments, Pauli paramagnetism based on delocalized electrons and van Vleck paramagnetism based on the orbital moments due to the rearrangement of electron orbital in external magnetic field, are other forms of paramagnetism [*Yos96, Kah93*].

Ferromagnetic

Ferromagnetism is a phenomenon in some magnetically-ordered materials in which there is a bulk magnetic moment and the magnetization is large. The electron spins of the atoms in microscopic regions (domains) of the sample are aligned. In the presence of an external magnetic field the magnetization of the domains tends to align with the field. The magnetization is retained even if the field is removed. The retention of magnetization distinguishes ferromagnets from paramagnets. Above the Curie temperature, the ambient thermal motion is sufficient to offset the aligning force and the material becomes paramagnetic [*Cal07*]. The main mechanism behind ferromagnetism is exchange interaction where electrostatic interaction is combined with quantum mechanics (Pauli's Principle) similar as the Hund's-Rule complying in the atoms.

In case of $Nd_2Fe_{14}B$, one of the materials used in this study, the 3*d* electrons of the Fe atoms are strongly coupled by itinerant electron exchange interaction, contributing nearly 90 % to the net magnetization of the compound and resulting in a Curie temperature T_C as high as 312 ^{0}C [*Her91*]. The Fe orbital magnetic moment is mostly quenched. On the other hand, the magnetic moment of most of the Nd localized 4*f* orbitals is not quenched and tends to be aligned by crystalline electric field along the tetragonal *c*-axis (for temperatures above 135 K, which is the spin reorientation temperature). A complicated 3*d*-5*d*-4*f* exchange interaction ferromagnetically couples the Fe magnetic moment to the Nd magnetic moment, transmitting the magnetic anisotropy of the Nd magnetic atoms to form the total magnetization of $Nd_2Fe_{14}B$, with the tetragonal *c*-axis as an easy-axis of magnetization ($T > 135$ K). Thus this mechanism of the exchange-coupling combines the high magnetic moments (also high T_C) of Fe atoms with the large magnetic anisotropy of the Nd atoms.

The most common way to represent the magnetic properties of a ferromagnetic material is by a plot of the magnetization M against the applied magnetic field H. In contrast to the non-hysteretic behavior of paramagnetic materials, which follows the Brillouin function, the magnetization M of a ferromagnetic material exhibits a hysteretic behavior as a function of the applied magnetic field H *[Spa11]*. As ferromagnetic materials are heated the degree of alignment of the atomic magnetic moments decreases due to thermal agitation.

Eventually the thermal agitation becomes so great that the material becomes paramagnetic; the temperature of this transition is the Curie temperature, T_C

Antiferromagnetic

Antiferromagnetic materials are very similar to ferromagnetic materials but the exchange interaction between neighboring atoms leads to an antiparallel alignment of the atomic magnetic moments. Therefore, the magnetic field generated by these atomic moments cancels out and the material appears to behave in the same way as a paramagnetic material. Like ferromagnetic materials these materials become paramagnetic above a transition temperature, known as the Néel temperature, T_N.

Ferrimagnetic

Ferrimagnetism is only observed in compounds, which have more complex crystal structures than pure elements. The ferrimagnets are microscopically similar to the antiferromagnets, in that they consist of two sub-lattices within which the moments are aligned parallel, with the two sub-lattices aligned antiparallel to each other. However, the magnitudes of the magnetic moments in the two sub-lattices are different, so that there is a net magnetization. As a result they behave macroscopically like the ferromagnets, with large positive susceptibility and hysteresis [*Spa11*]. For example, in case of the most used (by mass) permanent magnet, barium hexaferrite ($BaO.6Fe_2O_3$), the unit cell contains 64 ions

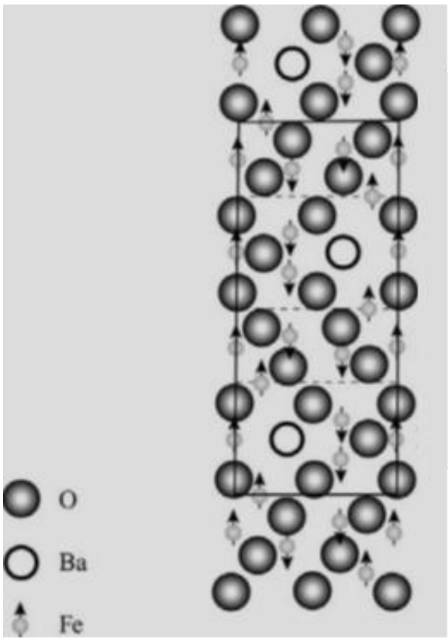

Figure 1.2 Showing magnetic ordering in ferromagnetic barium hexaferrite [*Spa11*].

of which the barium and oxygen ions have no magnetic moment, 16 Fe^{3+} ions have moments aligned parallel and 8 Fe^{3+} aligned anti-parallel giving a net magnetic moment, but with a relatively low magnitude as only ⅛ of the ions contribute to the magnetization of the material (figure 1.2) [*Sko99*].

1.3 Magnetic anisotropy, hysteresis and coercivity

1.3.1 Magnetic anisotropies

Magnetic anisotropy means that the magnetic properties depend on the direction in which they are measured. Some important magnetic anisotropies are as follows:

- Magnetocrystalline anisotropy: The magnetization is oriented along specific crystalline axes.
- Shape anisotropy: The magnetization is affected by the macroscopic shape of the solid.
- Induced magnetic anisotropy: Specific magnetization directions can be stabilized by tempering the sample in an external magnetic field.
- Stress anisotropy (magnetostriction): The displacement of atoms in the crystal strongly affects the interaction between neighboring orbitals and hence the magnetic behavior of magnetic crystals. Vice versa, magnetic properties can alter elastic properties. The responsibility of this interplay is the magnetoelastic interaction.
- Surface and interface anisotropy: For low-dimension systems, the surfaces and interfaces often exhibit different magnetic properties compared to the bulk due to their asymmetric environment.

Basically, magnetocrystalline anisotropy and shape anisotropy are more important for permanent magnetic materials and are discussed as follows.

Magnetocrystalline anisotropy

The magnetocrystalline anisotropy may be regarded as a force which tends to hold the magnetization in certain equivalent crystallographic directions in a crystal. In order to turn the magnetization direction away, the applied magnetic field must do work against the anisotropy force. There must be energy stored in the crystal in which magnetization points in a non-easy direction. This is called the magnetocrystalline energy.

Due to the preferential orientation of the magnetization in the crystal, a part of total free energy, called the magnetocrystalline free energy (or magnetic anisotropy energy, E_a)

depends on the direction of magnetization with respect to different crystallographic directions.

For hexagonal crystals,

$$\frac{E_a}{V} = K_1 sin^2\theta + K_2 sin^4\theta + K_3 sin^6\theta + K_3' sin^6\theta\ cos6\phi \qquad (1.2)$$

and for tetragonal crystals,

$$\frac{E_a}{V} = K_1 sin^2\theta + K_2 sin^4\theta + K_3 sin^4\theta cos4\phi \qquad (1.3)$$

θ is the angle between the *c*-axis and the vector of magnetization, ϕ is the angle between the projection of the magnetization vector in the basal plane of the crystal and one of the a-axes. K_1, K_2, K_3, and K_3' are the anisotropy constants. The anisotropy constants reflect the magnetic anisotropy only phenomenologically and have no direct connection with the physical origin of magnetic anisotropy.

The physical origins of magnetocrystalline energy are electric fields or quantum chemical forces acting on the charge clouds of the asymmetric atoms; in the materials investigated here ($SmCo_5$ and $Nd_2Fe_{14}B$) these are the Sm and Nd atoms. The spin-orbit interaction transfers the orientation direction of the rare-earth orbital momentum to the total momentum $\boldsymbol{J} = \boldsymbol{L} \pm \boldsymbol{S}$ and thus to the magnetization. The basis of the magnetic ordering and the magnetic anisotropy in metallic compounds of rare-earth (RE) metals combined with transition metals (T) are the RE-RE, T-T, and RE-T interactions. Naturally, in a metallic system most of the interactions are mediated by the electrons, especially by the conduction electrons, which means that the full band structure has to be taken into account.

For tetragonal ($Nd_2Fe_{14}B$) and hexagonal ($SmCo_5$) systems the magnetocrystalline energy is related to a cylindrical symmetry up to terms of the second or fourth order, respectively. The magnetocrystalline energy only depends on the angle θ between the magnetization direction and the *z*-axis. Therefore, a uniaxial symmetry exists [*Sko99*]. In $Nd_2Fe_{14}B$ at high temperatures, both the iron and neodymium magnetocrystalline anisotropies are uniaxial and the magnetization points in the [*00l*] direction. The $Nd_2Fe_{14}B$ compound exhibits changes in the easy-axis at a temperature (135 K) known as spin reorientation transition temperature. The spin reorientation transition in $Nd_2Fe_{14}B$, is caused by a temperature induced competition between the contributions to the net anisotropy from different terms of the crystalline electric field acting on the Nd^{3+} ions [*Kou97*]. The easy-axis of $Nd_2Fe_{14}B$ remains in [*00l*] direction between 585 *K* and 135 *K* and tilts away from the [*00l*] direction below 135 *K*. The tilting angle increases with lowering the temperature and reaches about 30° at 4.2 *K* [*Gar00*].

Shape anisotropy

Although most materials show some magnetocrystalline anisotropy, a polycrystalline sample with no preferred orientation of its grains will have no overall crystalline anisotropy [*Get08*]. However, only if the sample is exactly spherical, the same field will magnetize it to the same extent in every direction. If the sample is not spherical, then it will be easier to magnetize it along a long axis. This phenomenon is known as shape anisotropy [*Spa11*]. Figure 1.3 shows the shape anisotropy constant as a function of the *c/a* ratio for a prolate spheroid of polycrystalline Co. The shape anisotropy constant increases as the *c/a* ratio increases, and for a typical *c/a* ratios the shape anisotropy constant is of the same order of magnitude (around 10^6 ergs/cm^3) as the magnetocrystalline anisotropy constant.

The relationship $\boldsymbol{B} = \mu_0(\boldsymbol{H} + \boldsymbol{M})$ holds only inside an infinite system. A finite sample exhibits poles at its surfaces which leads to a stray field outside the sample. This occurrence of a stray field results in a demagnetizing field inside the sample.

The energy of a sample in its own stray field is given by the stray field energy E_{str}:

$$E_{str} = -\frac{1}{2}\int \mu_0 \boldsymbol{M} \cdot \boldsymbol{H}_{demag} dV \tag{1.4}$$

Where, $\boldsymbol{H}_{\text{demag}}$ is the demagnetizing field inside the sample.

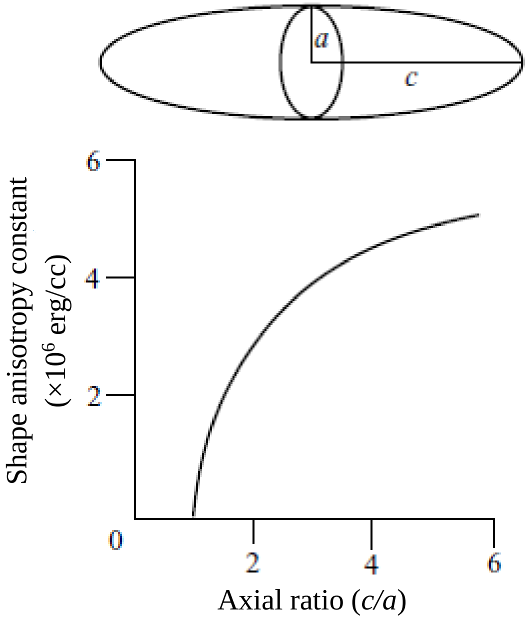

Figure 1.3 Shape anisotropy constant in a prolate spheroid of Co [*Spa11*].

The calculation of the magnetization field is rather complicated for a general shape. It becomes easier for symmetric objects. An ellipsoid possesses a constant demagnetizing field $\boldsymbol{H}_{\text{demag}}$ is given by:

$\boldsymbol{H}_{\text{demag}} = -\mathcal{N}\boldsymbol{M}$, where, $\mathcal{N}$ *is* the demagnetization tensor.

Thus the stray field energy density amounts to:

$$E_{str} = 1/2\,\mu_0 \int \boldsymbol{M}.N\boldsymbol{M}dV = 1/2 \cdot V\mu_0\boldsymbol{M}.N\boldsymbol{M} \tag{1.5}$$

There is not much contribution of the shape anisotropy in the RETM compounds because of the dominating magnetocrystalline anisotropy. The shape anisotropy plays an important role in old permanent magnets *e.g.* steel magnets and AlNiCo and FeCrCo magnets. AlNiCo consists of elongated Fe-Co particles in a Ni-Al matrix. These high-aspect-ratio Fe-Co needles with length of up to 1 μm and diameter tens of nanometers, provides a significantly high shape anisotropy and makes the AlNiCo a suitably good permanent magnet. Some of these systems are actually being investigated again with a focus on enhancing the shape anisotropy of materials, in order to find alternate magnets without rare-earth elements [*Kuz14*].

1.3.2 Hysteresis loop

Ferromagnetic and ferrimagnetic materials have non-linear initial magnetization curves due to the changing magnetic susceptibility with applied magnetic field. An external magnetic field applied to a ferromagnet causes the atomic dipoles in the material to align themselves with it. Even when the field is removed, part of the alignment will be retained: the material has become magnetized. These materials show hysteresis, i.e. the magnetization lags behind the field. The phenomenon of hysteresis in ferromagnetic materials is the result of two effects: rotation of magnetization and changes in size or number of magnetic domains (especially in large (multi-domain) particles). The magnetic state of material, after removal of the applied magnetic field is thermodynamically metastable. These metastable states (magnetized states) are crucially important for permanent magnets.

Figure 1.4 shows a typical initial magnetization curve and a hysteresis loop; both loops (red and black) represent the same data, however, the black loop is the magnetization and the red loop the induction, both plotted against magnetic field. For a demagnetized sample the initial magnetization curve begins at the origin, and, as H is increased, the

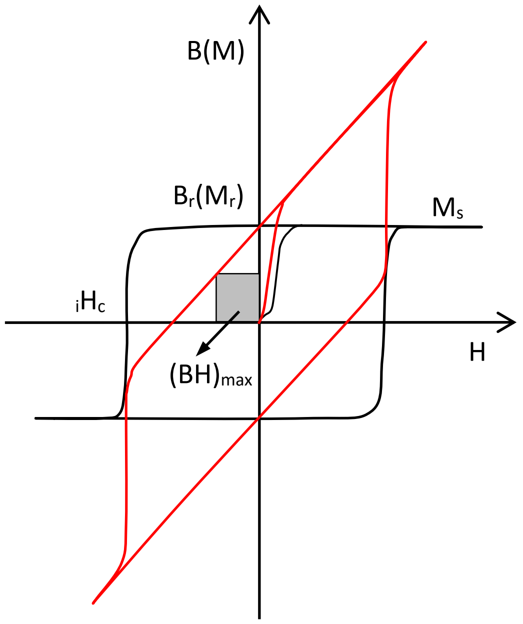

Figure 1.4 A typical hysteresis loop for a ferro- or ferri-magnetic material.

magnetization (*M*) begins to increase slowly, then more rapidly, finally leveling off and becoming independent of *H*. In the case of bulk (multi-domain particles), initially the moments of the constituent domains are randomly oriented such that there is no net *B* (or *M*) field. As the external field is increased, the domains that are oriented in directions favorable to (or nearly aligned with) the applied field grow at the expense of those that are unfavorably oriented. This process continues with increasing field strength until the macroscopic specimen becomes a single-domain, which is nearly aligned with the field. Saturation is achieved when this domain, by means of rotation, becomes oriented with the *H* field. In single-domain particles, the magnetization responds to a magnetic field by rotation [*Coe10*]. This maximum value of magnetization is the saturation magnetization M_s. If the field is reduced the magnetization returns to the y-axis (i.e. $H = 0$). The magnetization remaining in the material without any applied field is the remanent magnetization (M_r). After application of a sufficient negative field the magnetization will become zero and this field is the coercive field ($_iH_c$). Further increase in a negative field will lead to saturation of material in the negative direction. If the applied field is decreased and again applied in the positive direction, the full hysteresis loop is obtained. The area contained within the B-H loop indicates the amount of energy absorbed by the material during each cycle of the hysteresis loop. The maximum energy product is a very important quantity in permanent magnets. The area of largest square in the second quadrant of B-H loop (grey square in figure 1.4) is known as $(BH)_{max}$, which represents the maximum amount of energy stored in the magnet. A square shape of the hysteresis loop is crucial for good permanent magnets; in this case the remanence magnetization is nearly equal to the saturation magnetization [*Sko99*]. The upper limit of $(BH)_{max}$ is given by $\mu_0 M_s^2/4$ with the condition that $H_c \geq \mu_0 M_s/2$. In addition, the shape of the initial magnetization curve can provide information about the magnetic domain behavior within the material.

Generally, magnetic materials are characterized into two categories based on the coercivity and remanence deduced from the hysteresis loop. The materials with high coercivity and relatively large remanence are known as hard magnets (permanent magnets). On the other hand, magnetic materials with small coercivity are known as soft magnets. The soft magnetic materials reach the saturation magnetization at low fields and it is very easy to demagnetize them, whereas hard magnets reach the saturation at high field and achievement of demagnetization requires a higher field [*Cul72*].

1.3.3 Coercivity mechanisms: nucleation and pinning

The coercive field is an important quantity for hard magnetic materials; a ferromagnet can reverse its direction of magnetization either continuously or discontinuously, both through coherent or incoherent rotation processes, and through domain wall motion processes. Coercivity will be determined by the easiest of these processes. To achieve high coercivities, it is therefore necessary (a) to impede magnetization rotation with magnetic anisotropy, usually by employing magnetocrystalline or shape anisotropy, and (b) to impede either the nucleation or the growth of reverse domains (figure 1.5 (a)).

Magnetocrystalline anisotropy is the most effective means of impeding magnetization reversal by rotation processes. It is the main source of coercivity in the materials ($SmCo_5$ and $Nd_2Fe_{14}B$) investigated in this study. It provides an energy barrier resisting departure from the easy-direction of magnetization (low-energy) that impedes both coherent and incoherent rotation processes, independent of volume fraction and particle size. With a uniaxial magnetocrystalline anisotropy energy per unit volume given by $K\sin^2\theta$, and the field applied parallel to the easy-axis, the coercivity predicted for rotation is $2K/M_s$ (where, θ is the angle between the magnetization and the easy axis, K is anisotropy constant and M_s is the saturation magnetization). Experimentally-observed coercivity for crystalline-anisotropy materials is generally far less than $2K/M_s$, in these cases it is clear that magnetization reversal occurs not only by rotation, but by nucleation and growth of reverse domains. The domains can exist in particles which are of sufficiently large size. In the case of spherical non-interacting particles, the critical size of single domain D_C is given by

$$D_C = 72\,\frac{\sqrt{AK}}{\mu_0 M_S^2} \qquad (1.6)$$

where, A – exchange constant, K – anisotropy constant, μ_0 – vacuum permeability, M_s – saturation magnetization [*Kit46*].

In materials consisting of particles separated by paramagnetic phases, the critical value may deviate from equation (1.6) but it may be considered as an accurate approximation for this situation.

Coercivity can be limited either by domain nucleation or by domain growth, whichever is less difficult. Nucleation of reverse domains takes place most likely (a) at surface irregularities with large demagnetizing fields and (b) at chemical or physical defects where the crystal anisotropy is locally lowered. The latter will be more important for materials like the cobalt rare-earth elements based magnets, for which $K >> M_s^2$. In some cases, residual reverse domains may be present because of incomplete saturation. Nucleation-controlled coercivity can be increased by minimizing the density and size of nucleating defects and by subdivision into fine regions, i.e. into small grains, in which the probability of existence of such defects is small [*Coe10, Liv81*].

Growth of reverse domains can be impeded by defects, such as second-phase precipitates, which pin domain walls by locally altering wall energy γ, given in the continuum approximation by $4(AK)^{1/2}$. Most effective are defects with dimensions of the same order as the domain wall thickness δ, given by $\pi(A/K)^{1/2}$ in the same approximation. For very large K, walls become very thin, and even point defects may contribute to pinning [*Hub09, Liv81*]. The difference between pinning-controlled and nucleation-controlled behavior can be seen clearly by observing the initial magnetization behavior of a thermally demagnetized sample (figure 1.5 (b)). Thermal demagnetization generally leaves the sample with several domains per grain. In two-phase pinning-controlled magnets the existing domain walls cannot move easily, and permeability remains low until the applied field approaches the coercive field [*Giv92*]. However, in the single-phase nucleation-controlled magnets the existing walls move easily and initial permeability is high, the magnet approaches saturation at low fields [*Liv81*].

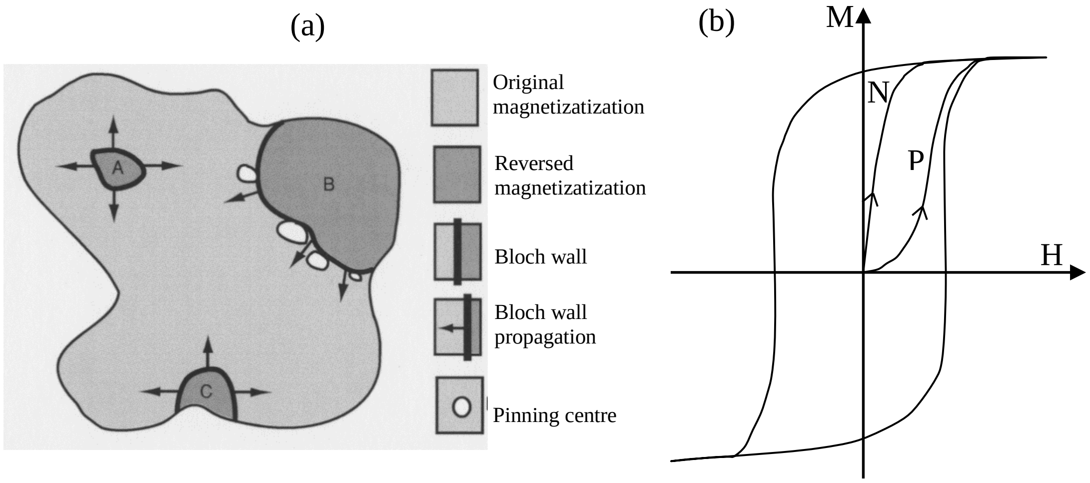

Figure 1.5 (a) Processes involved in magnetization reversal in the second quadrant of the hysteresis loop. A – reverse domain which nucleates in the bulk at a defect, or from a spontaneous thermal fluctuation; B – reverse domain which has grown to the point where it is trapped by pinning centers and C – reverse domain which nucleates at a surface asperity, (b) hysteresis loops showing nucleation (N) and pinning (P) controlled processes in initial magnetization curves [*Coe10*].

In materials consisting of particles of diameter $D < D_C$, a domain structure cannot exist and consequently such systems may not be called nucleation- or pinning-type magnets. In this case demagnetization is governed by certain kind of nucleation of switching magnetization. Nevertheless, there may be domain-like structures (interaction domains where a domain consists of multiple particles) in such systems. The ´´domain-width`` of interaction domains is larger than the group of participating particles [*Gut00, Gut06, Thi12*]. Two or three different modes of reversal can occur in a single-domain particle. First is the coherent rotation mode where the magnetization remains uniform everywhere, and the magnetic moment rotates in unison, increasing the stray field as it flips through a configuration where the magnetization is perpendicular to the easy-axis. Second is the curling mode, which avoids creating a stray field by passing through a vortex state where the magnetization lies everywhere parallel to the surface [*Coe10*]. This mechanism costs exchange energy. The vortex state is the lowest energy state of soft magnetic particles which are larger than the coherence radius. In long prolate ellipsoids, a third reversal mode known as buckling may occur, which is a combination of the other two reversal mechanisms that creates less stray field than coherent rotation.

1.4 Development of permanent magnets

1.4.1 Conventional permanent magnets

One of the earliest observations of magnetism can be traced back to Thales of Miletus who was a Greek philosopher in the 6th Century B.C. [*Coe95*]. He made the first definitive statement around 585 B.C., saying lodestone attracts iron because it has a soul. Later on, a Chinese scientist Shen Kuo (1031-1095) wrote about the magnetic needle compass which improved the accuracy of navigation [*Nee62*]. However, the modern understanding of magnetism began only after William Gilbert's publication in *De Magnete* in 1600, which is perhaps the first modern scientific text [*Coe10*].

The development of permanent magnetic materials, which had not significantly advanced since 1601, when Gilbert wrote of blacksmiths making steel compass needles, continued with the development of AlNiCo alloys in 1931 by Mishima [*Mis31*]. As the name suggests these alloys are based on Al, Ni, Co and Fe, with energy products of 88 kJm^{-3} achieved. These magnets have the advantage of having a high Curie temperature (~850 ^{0}C) which allows them to still be used today for high temperature applications or where thermal stability of magnetization is required. The 1950's saw the discovery of hard hexagonal ferrites or ceramic magnets by the Philips Company [*Coc66*]. These materials displayed a far higher coercivity than that had previously been seen (~250 kAm^{-1}), although, when coupled with a low remanence, this leads to an overall low maximum energy product. The key to this high coercivity lies in the presence of uniaxial magnetic anisotropy [*Coe96*].

In the 1960's the RETM compounds $RECo_5$ were discovered in the USA [*Nes59*]. The combination of rare-earth and transition metal is complementary to one another. The rare-earth component provides the magnetic anisotropy to the phase, and the transition metal provides the high magnetization and Curie temperature. It was discovered that $SmCo_5$ magnets could be produced with an energy product of ~160 kJm^{-3} by sintering [*Das69*]. This was the first commercially available RETM permanent magnetic material. The success of these materials was limited due to the high costs associated with the raw materials and their production. These high costs were a driving force behind the discovery of NdFeB based magnetic materials. The fortuitous discovery of such a ternary phase was announced by two groups, working independently, in 1983 [*Cro84, Sag84*]. Croat and co-workers used melt spinning to produce a nanocrystalline coercive Nd-Fe-B alloy which became known by its trade name as MAGNEQUENCH, while Sagawa and co-workers found the hard magnetic

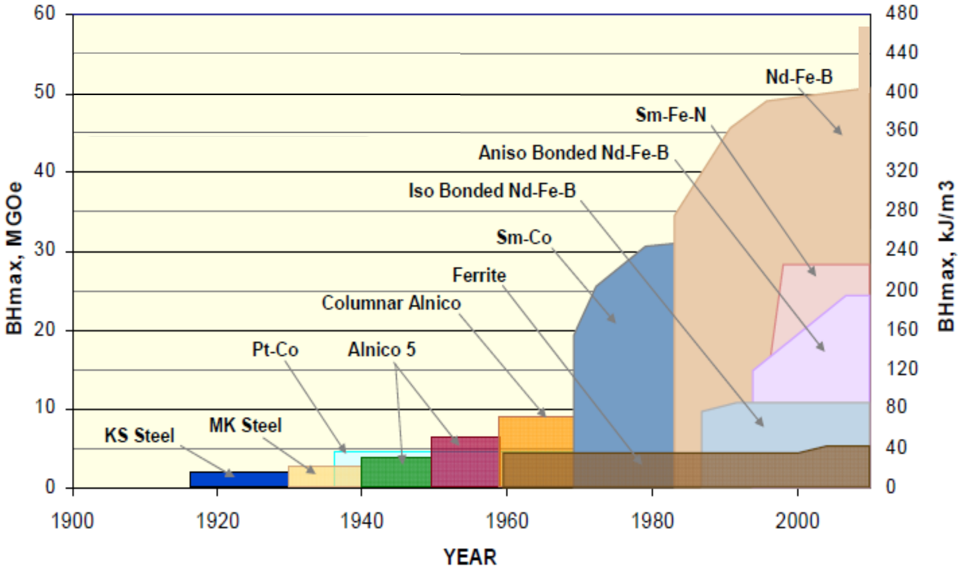

Figure 1.6 Progress in improving $(BH)_{max}$ over the past century. Energy product has increased nearly exponentially. [*Arnold Magnetic Technologies*]

compound by more traditional methods of powder metallurgy and magnetic orientation, and named it NEOMAX. The long process of microstructure optimization led to further doubling of the energy product up to its current record value of 474 kJm^{-3}, for a laboratory magnet [*Mat06*]. The optimization of the material has proceeded to the point where the best values of $(BH)_{max}$ are very close to the maximum calculated $(BH)_{max}$ (512 kJ m^{-3}) for the phase. A progress in the improvement of $(BH)_{max}$ value over the past century is shown in figure 1.6.

1.4.2 Next generation of permanent magnets

1.4.2.1 Rare-earth free permanent magnets

Magnets based on a composition containing rare-earth and transition metal elements have some drawbacks. The main drawback is that it contains rare-earth elements like Sm, Nd, Dy, Pr and even though rare-earth elements are not that rare, they are mined only in certain places of the world. Most easily-exploitable ores are found in China, and the current sources of the heavy rare-earth elements such as dysprosium and terbium are almost exclusively Chinese. The price of neodymium oxide for the last few years has increased significantly and is still fluctuating [*Eur14*]. Many monazite and bastnaesite ores rich in light rare-earth elements are slightly radioactive, due to the presence of thorium. In addition the production and processing of rare-earth elements are very energy consuming and also cause environmental issues [*Hur10*]. Keeping the rare-earth crisis and environmental issues in mind, the current research focus is moving toward the rare-earth reduced/free permanent

Table 1.1 Properties of some uniaxial ferromagnets [*Coe12*]

	MnAl	**MnBi**	**Mn_2Ga**	**$Y_2Fe_{14}B$**	**α'' $Fe_{16}N_2$**	**Fe_3C**	**YCo_5**
M_s (MAm^{-1})	0.60	0.58	0.47	1.10	1.92	1.09	0.85
K_1 (MJm^{-3})	1.7	0.90	2.35	1.1	1.0	0.45	6.5
T_C (K)	650	628	>770	590	810	56	987
K	1.95	1.46	2.35	0.85	0.43	0.55	2.7

M_s - satruration magnetization
K_1 - anisotropy constant
T_c - Curie temperature
K - hardness parameter

magnets. Table 1.1 summarizes the properties of a few interesting uniaxial ferromagnetic compounds which are in the current research focus. It is possible to achieve any individual target value, but no material quite manages to combine the required T_C, M_s, K and energy product so far.

For a permanent magnetic material equivalent to $Nd_2Fe_{14}B$, a magnetization value of 1.26 MAm^{-1}, K_1 of 2 MJm^{-3} and T_C of 550 K is required. The magnetization of the selection of materials in table 1.1 shows that the target value of 1.26 MAm^{-1} may be achievable, provided not too much of the nonmagnetic partner element is present. The tetragonal $L1_0$ structure is potentially interesting, but if only half the atoms in the alternating layers is magnetic, as in carbon-stabilized τ-MnAl, the magnetization will inevitably fall short of the target. Tetragonal MnAl is a permanent magnet material but $(BH)_{max}$ is only 112 kJm^{-3} and the achievable energy product is much less. A particularly interesting example of an $L1_0$ compound is τ-FeNi. It is found in iron meteorites which have had billions of years to reach thermal equilibrium [*Lew14a*]. The value of T_C is only 320 ^{0}C [*Kub82*]. The phase has been prepared by neutron irradiation of fcc FeNi [*Nèe64*]. Severe tetragonal distortion of the cubic Heusler structure in DO_{19}-type MnGa is a good example, but unfortunately the magnetic structure is ferrimagnetic, suffering from the tendency of manganese atoms to couple antiferromagnetically. For α''-$Fe_{16}N_2$, an interstitial compound that is only stable at low temperature and is very difficult to prepare in bulk in single-phase form [*Coe94, Tak00*], but which has a magnetization approaching 2 MAm^{-1}.

1.4.2.2 Nanocomposite exchange spring permanent magnets

The exchange spring behavior was first described by Schneider *et al.* in 1990 in NdFeB system [*Sch90*]. However, Coehoorn *et al.* already reported the two-phase system of $Nd_2Fe_{14}B$ and Fe_3B in 1988 [*Coe88*]. Later the findings were explained by Kneller and Hawig [*Kne91*] and since then much focus has been given on the development of high-energy-density nanocomposite permanent magnets. The idea of exchange spring magnets is that the hard and soft magnetic phases can be exchange-coupled in an appropriate nanostructure in such a way that the composite as a whole exhibits hard magnetic properties. The name exchange spring stands for the largely reversible ''spring-like'' magnetic interaction that takes place between the constituent magnetic components under the application and removal of an applied magnetic field. The one-dimensional model for nanocomposite exchange spring magnet proposed by Kneller and Hawig is shown in figure 1.7. The interphase interfacial magnetic exchange-coupling yields a composite system that benefits from the best attributes of the constituent phases. The magnetically-hard phase provides high anisotropy and accompanying high coercivity, while the magnetically-soft phase provides a large saturation magnetization. As a combined result the energy-density value of composite magnets surpasses the energy-density value of both the individual constituent phases.

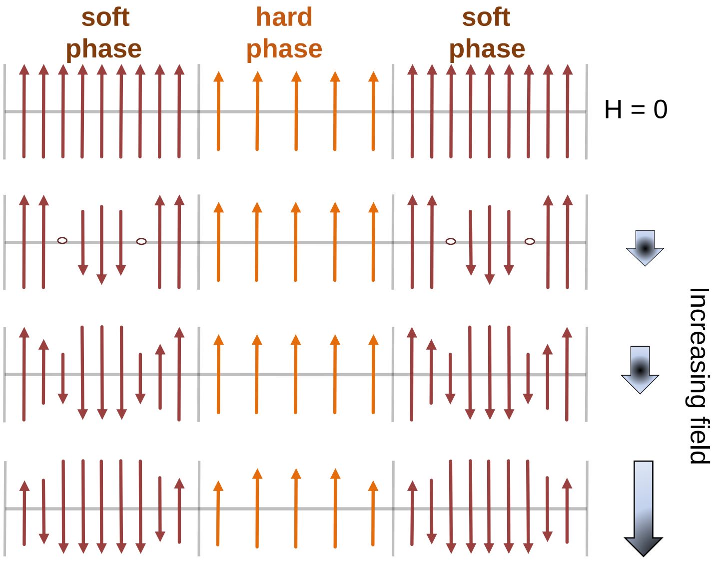

Figure 1.7 Schematic one-dimensional model of the microstructure and the micromagnetic structure of the exchange-coupled composite material. The interfacial parts of the soft magnetic phase are coupled with the hard magnetic phase even at higher reversal field.

The concept of exchange spring magnet was further developed by Skomski and Coey [*Sko93*] who showed that the length scale of the soft phase should be of the order of the exchange-length of the hard phase (a few nanometers) and they suggested that it may be possible to achieve an energy product in excess of a megajoule per cubic meter in an optimized hard/soft nanocomposite. There has been progress in demonstrating the exchange spring concept experimentally in model systems, where energy products in excess of that of the hard phase have been achieved [*Saw11*, *Cui12*]. Techniques used to produce the nanocomposites, recently reviewed by Liu *et al.* [*Liu11*], include melt spinning, bilayer or multilayer thin film deposition, core-shell nanoparticle assembly, mechanical alloying, surfactant-assisted ball milling, warm compaction, explosive compression, and shear extrusion.

The energy product of the nanocomposite may be as much as three times that of the isotropic hard phase [*Saw11*]. However, it will be necessary to achieve a considerable degree of orientation of the hard nanocrystallites if progress is to be made in advancing the record. As suggested by Coey, if competitive bulk magnets are ever to be produced using this approach, it will be necessary to devise a cost-effective manufacturing procedure for creating a thermally stable, oriented nanostructure, perhaps analogous to the procedure used to create oriented AlNiCo, but on an even smaller scale [*Coe11*].

Various schemes for exchange coupled nanocomposite structures composed of nanostructured hard and soft phases are illustrated in figure 1.8. For ideal exchange-coupling, the magnetic reversal of the hard and soft phases must occur simultaneously in

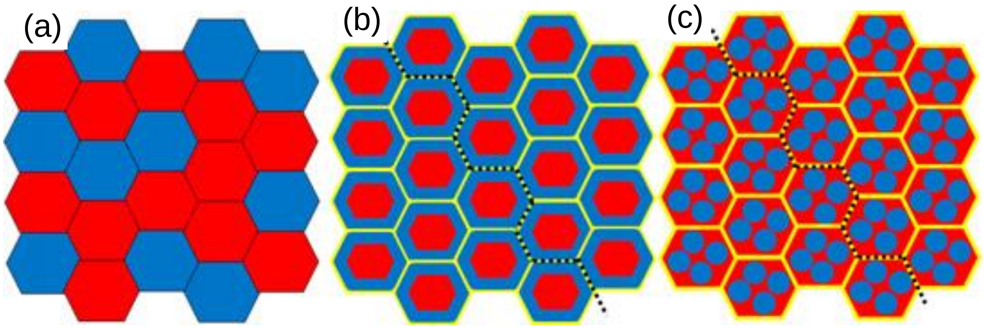

Figure 1.8 Various schemes for exchange-coupled nanocomposite structures composed of magnetically-hard (red) and soft (blue) nanoparticles: (a) conventional structure with soft and hard nanoparticles; (b) core–shell hard–soft nanoparticles and (c) nanocomposite particles with a non-magnetic layer (yellow), where the pinning of domain walls is indicated by black-dotted lines. [*Bal12*]

nanocomposites [*Bal12*]. The nanocomposite structure as illustrated in figure 1.8 (a) is similar to the chemically prepared FePt-Fe_3Pt and compacted $SmCo_5$:$Fe_{65}Co_{35}$ nanocomposites [*Lyu05, Zen02, Ron10b, Zha10*]. If the dimension of the soft phase is too large, magnetic reversal initiates in the soft magnetic phase, owing to its lower anisotropy. This process leads to the propagation of domain walls and results in a reduction in coercivity and remanent magnetization at a large fraction of soft phases. Thus, developing a nanostructure as schematically shown in figure 1.8 (b) and (c), which inhibits domain expansion by pinning of domain walls using a non-magnetic layer around the nanocomposite particles, would significantly improve the magnetic properties by maintaining coercivity at high soft magnetic-phase fractions.

In general, the processing of nanocomposite magnets is mainly based on melt spinning and mechanical alloying utilizing FePt, $Nd_2Fe_{14}B$, and $SmCo_5$ as the hard phase and Fe_3Pt, Fe_3B, Fe, and FeCo as the soft phase; however, these methods produce only isotropic materials. Good texture has been obtained in the case of thin films and nanoparticles prepared by gas phase condensation but these methods are not suitable for large scale synthesis of materials. There is a need to develop methods for large scale material synthesis which possibly can be achieved by chemical and/or surfactant-assisted ball milling processes. There is a possibility of an alternate route to make bulk nanocomposite permanent magnets by combining separately prepared nanostructured textured hard and nanometer-sized soft phases. The preparation routes of nanometer-sized soft phases (*e.g.* Fe, FeCo) with high magnetization values, using chemical solution methods have been developed [*Yan08, Pal10, Cha07a*]. On the other hand it is challenging to prepare the hard magnetic RETM nanometer-sized particles in bulk amount using chemical routes. Recently, there has been some interest in preparing nanometer- or micrometer-sized RETM particles using surfactant-assisted ball milling. This method is very useful to obtain nanometer- or micrometer-sized single-crystalline and highly textured polycrystalline particles in bulk amount. This thesis is focused on the fabrication and characterization of ultrafine hard magnetic RETM ($SmCo_5$ and $Nd_2Fe_{14}B$) particles obtained by a novel surfactant-assisted ball milling process.

1.5 Literature review on surfactant-assisted ball milling

Due to the limited success of the chemical solution method for synthesis of RETM nanoparticles, the surfactant-assisted (SA) ball milling technique, which has long been used for making ferro-fluids [*Ros85, Ode02*]. The presence of surfactants during ball milling process provides a capping or coating layer over the particles and prevents re-welding between the particles during milling and thus allows the grinding down to nanometer size. The SA – ball milling was employed for the first time by Chakka *et al.* for the fabrication of RETM nanoparticles [*Cha06*]. Since then this method has been in focus for studying different RETM materials to obtain nanometer size particles.

In the 1990s, Campbell *et al.* and Kaczmarek *et al.* used surfactants during wet milling of barium ferrite and observed a rapid decrease in the powder particle size and a homogenization with increased milling time [*Cam94, Kac95*]. In 1996 Kirkpatrick *et al.* reported that the particle size obtained by ball milling of Sm-Co powder with surfactants was smaller compared to that of particles milled without surfactants [*Kir96*]. Additionally, when surfactants were used along with a solvent during milling of the magnetic powders a non-transparent nanoparticle solution was obtained along with coarse particles as slurries which quickly sedimented to the bottom of the milling vials. Surfactants used during milling are adsorbed by the fresh surface of particles crushed during the ball milling, leading to a surface modification for the ground particles. Oleic acid and oleylamine have been mainly used as surfactants in preparation of Sm-Co and Nd-Fe-B nanoparticles. Other surfactants such as trioctylamine, octanoic acid myristic acid, stearic acid, palmitic acid, undecanoic acid and valeric acid have also been tried to fabricate nanoflakes and nanoparticles [*Zhe10, Cro12*]. The particles obtained after SA – ball milling consist of a wide size distribution ranging from several nanometers to micrometers. A size-selection process is necessary to obtain nanoparticles with the desired size range [*Wan07b, Pou10*]. Wang *et al.* developed the size-selection process based on a sophisticated control of the ‘settle-down’ time of the nanoparticle solutions and a proper use of centrifugal separation to obtain nanoparticles of different sizes [*Wan07b*]. It was found that the as-milled particles had irregular shapes and a wide size distribution from several nanometers to larger than 50 nm and the sedimented particles were in the micrometer range.

Chakka *et al.* first reported the preparation of Fe, Co, FeCo, SmCo and NdFeB nanoparticles employing SA – ball milling on starting 10-μm- to 45-μm-sized particles in the presence of solvent n-heptane and surfactants oleic acid and oleylamine [*Cha06*]. It was observed that the nanoparticles of Fe and FeCo were close to spherical shape, whereas those of Co, SmCo and NdFeB showed an elongated rod-like shape. All the nanoparticles showed superparamagnetic behavior at room temperature. Very low coercivities (< 100 Oe) and low M_r/M_s values were obtained for $SmCo_5$- and Sm_2Co_{17}-based powders. Surprisingly, the compositions of FeCo, SmCo and NdFeB nanoparticles prepared by SA – ball milling were found to deviate from the starting powder. While the magnetic properties were far below the characteristic values but the success of nanoparticle preparation by SA – ball milling was demonstrated.

Poudyal *et al.* investigated particle size and composition effects on coercivity of the Sm-Co nanoparticles [*Pou10*]. The nanoparticles were prepared by SA – ball milling of $SmCo_x$ (x = 3.5-10) starting alloys and nanoparticles with different size (8-140 nm) were separated using the size-selection process. It was observed that the $SmCo_x$ nanoparticles become structurally unstable and free cobalt was observed with increasing Sm content [*Pou10*]. It was also observed that the coercivity of the $SmCo_x$ nanoparticles increased with Co content and particle size. The room-temperature coercivity ranged from 0.5 to 3 kOe for nanoparticles of 8 to 140 nm in size which indicates a complex effect of the particle size and the composition on magnetic hardening of the hard magnetic nanoparticles. In a similar study, Yue *et al.* investigated the effect of particle size on coercivity of Nd-Fe-B nanoparticles obtained by SA – ball milling [*Yue09*]. It was observed that the nanoparticles were partially amorphous. The room-temperature coercivites of 10- and 100-nm-sized particles were 0.1 and 1.5 kOe, respectively. Furthermore, it was also found that the coercivity of the 100 nm particles increased by 50% as the measuring temperature dropped down to 200 K due to the enhancement of the magnetocrystalline anisotropy of the $Nd_2Fe_{14}B$ phase in the particles. However, a similar increase in coercivity was not detected for the 10 nm particles, indicating that the small particles are more prone to amorphization and oxidation.

Micrometer- or sub-micrometer-sized Sm-Co and Nd-Fe-B flake-like particles (nanoflakes/nanochips) with high aspect ratios (10-1000) have been obtained by SA – ball milling. In all cases, it was observed that Sm-Co and Nd-Fe-B tend to form flakes after SA – ball milling. The dependence of the magnetic properties on the thickness and crystallinity of $SmCo_5$ flakes was studied by Knutsan *et al.* and Chen *et al.* [*Knu11, Che11*]. The coercivity of these flakes was found to increase at the beginning of milling to a peak value (~20 kOe) and then decreased with decreasing flake thickness or increasing milling time. $Nd_2Fe_{14}B$ flakes were similar as those of $SmCo_5$ in terms of morphology but the coercivity values were much less (< 5 kOe) as compared to those of sintered magnets [*Akd10, Cui12a*]. Experimentally it is found that the anisotropic $SmCo_5$ nanoflakes have their *c*-axis perpendicular to the plane of the flakes whereas $Nd_2Fe_{14}B$ flakes have their *c*-axis along the plane of the chips [*Cui11, Pou11*]. Formation mechanisms of the anisotropic flake-like particles are not fully understood, which might be related to fracture along some preferred crystalline orientation during high-energy ball milling in the presence of the surfactants [*Cui11*]. Introduction of lattice defects, such as edge dislocations, may play a role in the formation of anisotropic particles [*Yam02*]. Materials such as hexagonal $SmCo_5$ and tetragonal $Nd_2Fe_{14}B$ with a low symmetrical structure easily form plate-like structures, which upon further milling would result in the formation of anisotropic particles.

There are some reports on the preparation of textured micrometer- or sub-micrometer-sized flakes by SA – ball milling in presence of a magnetic field [*Ron10a, Sar07, Pou04*]. The surfactants help to reduce the particle size, while the magnetic field improves the grain alignment of the particles. On comparison, it was observed that the field-milled nanoflakes have an increased M_r/M_s ratio and a decreased misalignment, better than those without a field. It was observed that when the milling process is carried out in a magnetic field, the flakes got magnetized and formed chains with their surfaces perpendicular to the magnetic field direction. The *c*-axis of the chips was found to be in the direction of the magnetic field. Without a magnetic field, the long-range chains do not form. The improved alignment is associated with a better orientation of each flake with its *c*-axis in the chain-axis direction (perpendicular to the flake plane in the case of Sm–Co materials).

In last couple of years, the SA – ball milling has been used to prepare micrometer-sized flakes and nanoparticles of rare-earth transition metal compounds. However, the reports showed that there was significant distribution in the size of flakes varying from 2 μm to 10 μm. Nanoparticles with a small size distribution were separated from the mixture of flakes using a size-selection process, but the yield of the nanoparticles was very low (only few milligrams). The flakes and nanoparticles are formed after ball milling in presence of surfactants. There is a lack of reports on systematic studies of formation mechanism of flakes and nanoparticles and the development of texture during SA – ball milling. The formation mechanism and evolution of texture can be understood by studying the influence of different milling parameters on the microstructure of flakes and particles. Considering this, a systematic study on the influence of different ball milling parameters, *e.g.* type of solvent and surfactant, amount of surfactant, milling energy for the preparation of $SmCo_5$ and $Nd_2Fe_{14}B$ particles and flakes is carried out in this dissertation and the formation mechanism of micrometer-/sub-micrometer-sized single-crystalline and textured polycrystalline particles and flakes and nanoparticles is studied. By choosing dynamic-hydrogen-disproportionation-desorption-recombination (d-HDDR) processed Nd-Fe-B particles as starting material, it was possible to fabricate ultrafine (200-500 nm) single-crystalline $Nd_2Fe_{14}B$ particles in bulk amount (tens of grams). The nanoparticles prepared using SA – ball milling must be subjected to high temperature processing to make nanocomposite magnets. However, the high temperature processing of these flakes or nanoparticles has not been investigated in detail, although this study is crucial to understand the behavior of thermally treated particles and flakes. In this thesis, a detailed investigation on heat-treatment and hot-compaction of the chosen $Nd_2Fe_{14}B$ single-crystalline particles and studies on the microstructural and magnetic properties is reported.

Chapter 2

Experimental techniques

2.1 Starting materials

2.1.1 $SmCo_5$ powder

$SmCo_5$ powders, prepared by the co-reduction process, were purchased from Great Western Minerals Group Ltd [*Gwm*]. The manufacturing of Sm-Co alloys *via* co-reduction of an oxide mix is a specialized process yielding very fine-grained high performance alloy powders. The co-reduction method developed by Herget and Domazer [*Her75*] employs the reduction of a mixture of oxides of Sm and Co with Ca at high temperature (see equation 2.1). CaO obtained after reaction can be washed away with water. This method has now become the industry standard for $SmCo_5$ production.

$$R_2O_3 + nCo_3O_4 + (10-3n)Co + (4n+3)Ca \xrightarrow[3\ hours]{1000\ ^0C,\ vacuum} 2RCo_5 + (4n+3)CaO \qquad (2.1)$$

$$n = 0 \ldots\ldots \frac{10}{3}$$

The as-obtained $SmCo_5$ powders (~ 200 μm) were ground down to 40 μm size prior to SA – ball milling.

2.1.2 d-HDDR $Nd_2Fe_{14}B$ powders

$Nd_2Fe_{14}B$ powders (with initial composition $Nd_{28.78}Fe_{bal}B_{1.1}Ga_{0.35}Nb_{0.26}$) used for SA – ball milling were prepared by K. Güth *et al.*, using the d-HDDR process [*Güt11*]. The HDDR process was first reported for NdFeB magnets by Takeshita and Nakayama [*Tak89, Tak90*], and the principle reaction mechanisms involved were clarified by McGuiness *et al.* [Mc*G90a*, *McG90b*] and Harris *et al.* [*Har90*]. A schematic illustration of the conventional HDDR process is shown in figure 2.1. In this process, a NdFeB ingot is heated to 800-900 ^{0}C and kept at this temperature under hydrogen (which is often accompanied by the decrepitation of the ingot into powder), and then heat-treated under vacuum. After cooling under vacuum, a coercive powder is obtained. This process consists of four steps:

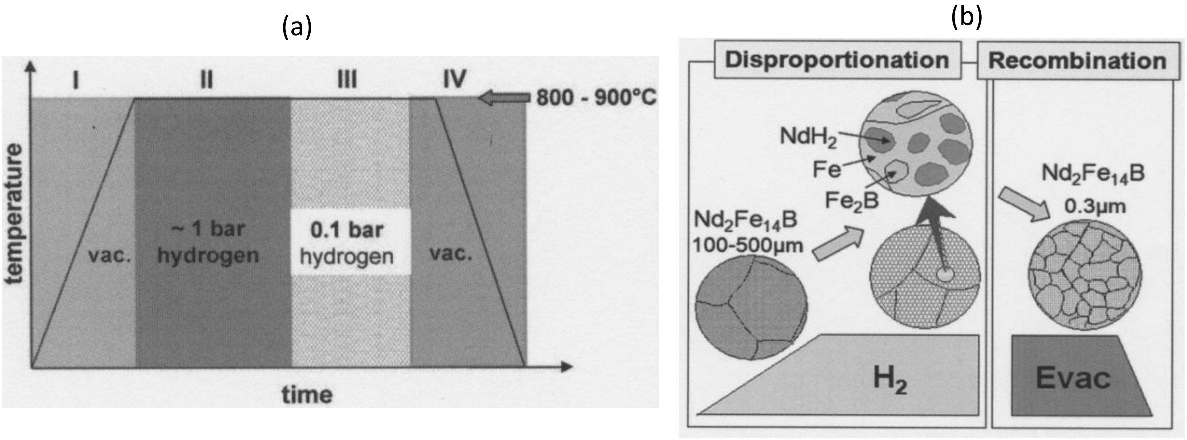

Figure 2.1 (a) Schematic illustration of the HDDR process in NdFeB: I – heating in vacuum, II – disproportionation, III – recombination and IV – desorption, (b) morphological development during desorption and recombination process in NdFeB [*Gut00, Sug06*].

hydrogenation of $Nd_2Fe_{14}B$; disproportionation of $Nd_2Fe_{14}B$ into $NdH_{2+\delta}$, α-Fe, and Fe_2B (see equation 2.2); desorption of hydrogen gas from $NdH_{2+\delta}$; and finally, recombination to the $Nd_2Fe_{14}B$ phase. During this process grain refinement occurs, resulting in a coercive powder that contains $Nd_2Fe_{14}B$ grains of 300 nm average size which is close to the single domain size for the $Nd_2Fe_{14}B$ phase.

$$Nd_2Fe_{14}B + (2\pm x)H_2 \Leftrightarrow 2NdH_{2\pm x} + 12Fe + Fe_2B \pm \Delta H \qquad (2.2)$$

The term “dynamic” is used to describe the dynamic control of the (low) hydrogen pressure and temperature during the disproportionation and recombination steps, where the reaction is exothermic and endothermic, respectively. The role of hydrogen partial pressure in changing the thermodynamic phase equilibrium of disproportionation and recombination has been described by Sugimoto *et al*. [*Sug97*]. Under optimal conditions, the final grains within one particle show a strong preferential orientation which is explained by the texture memory effect (TME) model [*Gut03*]. In the TME model, the orientation of the parent particle is transferred to the final grains *via* a textured intermediate phase (Fe_2B) during the d-HDDR process of Nd-Fe-B. Fe_2B is the only tetragonal disproportionation product, in addition to face-centered cubic NdH_x and body-centered cubic Fe.

2.2 Surfactant-assisted ball milling

Surfactant-assisted ball milling is similar to conventional ball milling except that the ball milling is performed in presence of surfactants (surface active agents) and/or carrier liquids (solvents). In conventional dry ball milling of metallic systems, usually only a sub-micrometer minimum average particle size is obtained even for an extended milling time

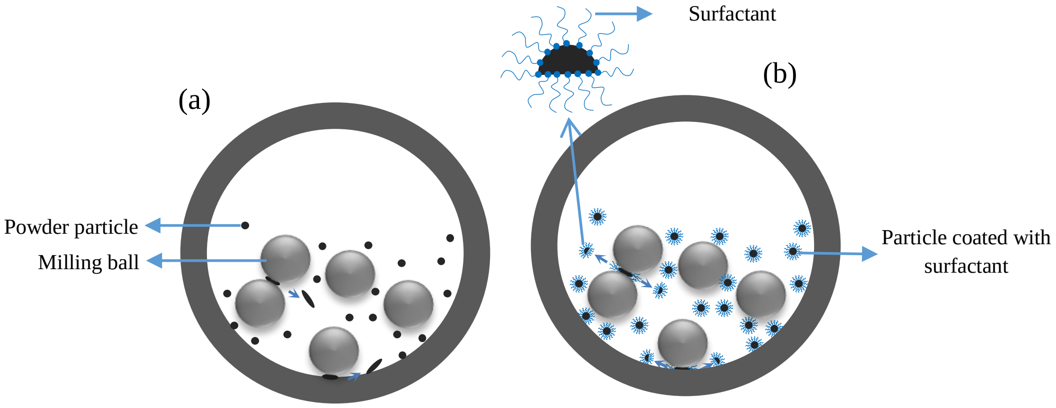

Figure 2.2 Schematic illustration of (a) dry and (b) SA - ball milling process. In dry ball milling particles re-weld and form agglomerates after impact with milling balls, whereas in SA – ball milling a particle coated with surfactants breaks into two separate particles and the broken surface gets coated with the surfactant. The surfactant coating prevents the re-welding of the particles.

because the crushed fine particles can be re-welded during ball milling [*Sur01*]. Addition of surfactants along with organic solvents improves the milling efficiency and prevents the re-welding during ball milling. As a result, particles down to nanometer size can be obtained. The function of the surfactants during ball milling is multifold:

I. The surfactants prevent the re-welding of the crushed particles during ball milling; thus fine nanoparticles can be obtained.
II. The surfactant-induced surface modification can significantly enhance the dispersion of nanoparticles in a solvent, leading to a size-dependent settling time in the solutions that provides good opportunities for size selection of the nanoparticles.
III. Surfactants coated on the surfaces also act as lubricants on particle surfaces which results in a particle fracture behavior that is different from the situation without surfactants. This phenomenon likely helps the formation of high-aspect ratio nanoparticles and flakes.
IV. The surfactant coating of particles reduces the friction and thus to some extent the surface damage of particles.
V. The surfactants act as protection layers on the particle surfaces and thus reduce contamination from the milling ball and vials.

During the milling process, as soon as the particles and/or fresh surfaces are formed, the surfactants are adsorbed through the polar head groups on to the surface of the particles [*Yan07*, *Gab10*]. A comparison of FTIR spectra of PrCo5 samples milled with and without oleic acid, reported by Gabay *et al.* [*Gab10*] is shown in figure 2.3 (a). Importantly, the peak at 1705 cm^{-1} in the FTIR spectra (figure 2.3 (a) (i)) is dramatically suppressed compared to

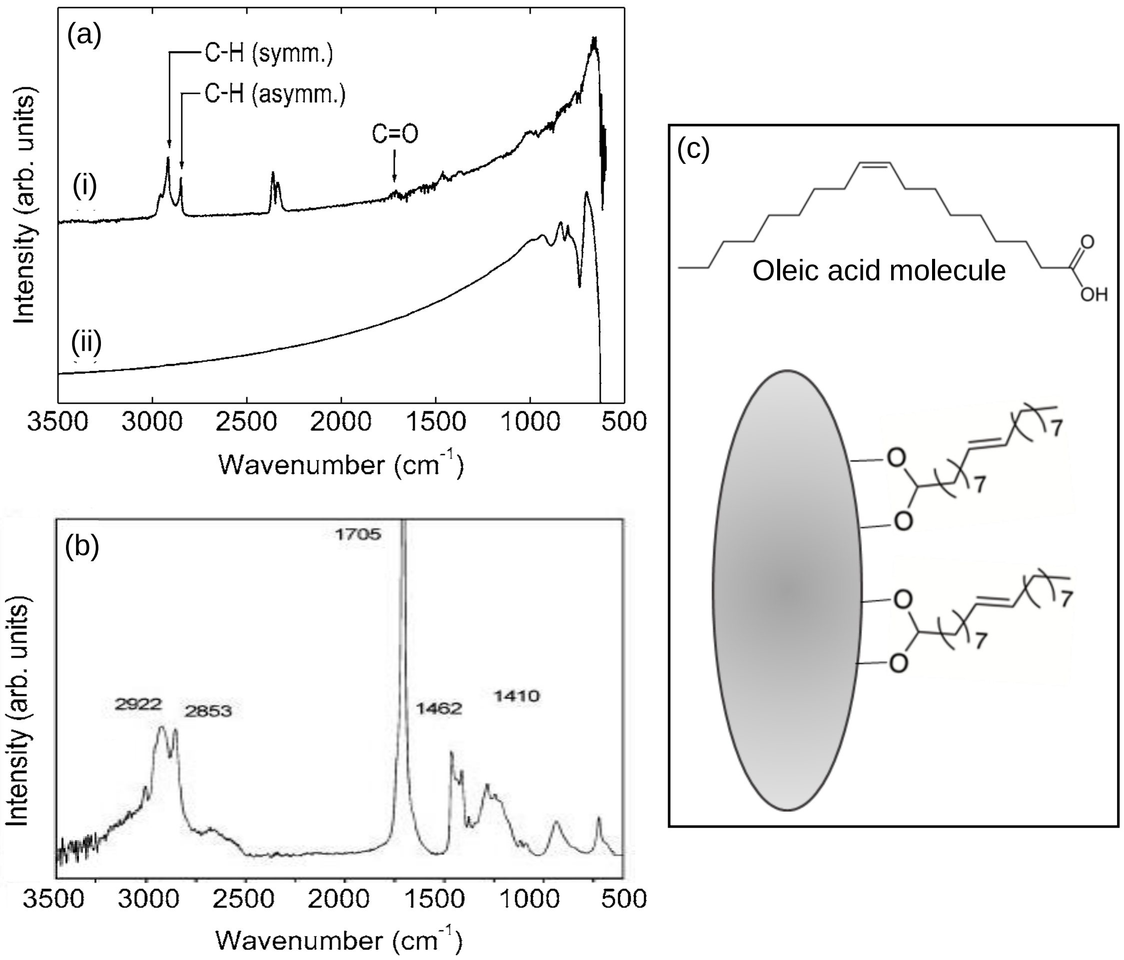

Figure 2.3 (a) Fast fourier transform infrared (FTIR) spectra of PrCo$_5$ powders milled for 60 min in heptane (i) with oleic acid and (ii) without oleic acid, (b) FTIR spectra for pure oleic acid, and (c) leic acid molecule and an schematic showing the attachment of oleic acid molecules onto the particles surface [*Gab10, Jai05, Her14*].

the spectrum of pure oleic acid (figure 2.3 (b)) indicating that the C=O bond is broken. This suggests that, during the SA – ball milling, the oleic acid molecule is attached to the particle in carboxylate form [*Gab10*] (see figure 2.3 (c)).

The long hydrocarbon tails of surfactants, which repel each other, help to prevent the re-welding or agglomeration. Therefore, after the SA – ball milling, ultrafine particles are obtained and a black colored liquid containing a dispersion of nanoparticles is observed along with coarse micrometer-sized particles and/or flakes (slurry particles), which immediately settle down at the bottom of the milling vial.

2.3 Sample preparation

Samples were prepared by ball milling of $SmCo_5$ and d-HDDR processed $Nd_2Fe_{14}B$ powders in the presence of surfactants and/or solvents given in table 2.1. The ball milling was performed employing a Fritsch Premium7 planetary ball mill using tempered steel milling vials of 80 ml volume and tempered steel milling balls of 5 and 10 mm diameter. The number of ball of 5 mm and 10 mm diameters were the same. The milling system is shown in figure 2.4. Oleic acid (90 %) and polyvenylepyrrolidone were used as surfactants along with n-heptane (99.8 %) and ethanol (99.9 %) solvents, respectively. The fabrication mechanism of nanoflakes and nanoparticles were studied for samples ball-milled with 10 wt.% (of powder weight) oleic acid and 60 wt.% (of powder weight) n-heptane. In order to study the effect of the amount of surfactants on the ball-milled samples, the amount of surfactant was varied from 5 to 50 wt.% of the starting powder weight while keeping the solvent amount at 60 wt.% of the powder weight. In addition, the $SmCo_5$ and $Nd_2Fe_{14}B$ powders were ball-milled in the presence of n-heptane and absolute (*abs.* hereafter) ethanol to study the influence of polarity and chain length of solvents on the microstructural and magnetic properties of ball-milled samples. For comparison, the samples were prepared using dry ball milling as well. In case of planetary ball mill, the milling energy depends on the powder-to-ball weight ratio and on the rotational speed of the mill [*Sur04*]. The influence of the milling energy was studied by varying the rotational speed of the mill from 200 to 800 rpm while keeping the powder-to-ball weight ratio constant. It is easy to realize that the faster the mill rotates the higher will be the energy input into the powder. However, depending on the design of the mill, there are certain limitations to the maximum speed that

Figure 2.4 Fritsch Premium7 planetary ball mill and tempered steel vial set consisting of vial, lid, O-ring and balls.

could be employed during the process. For example, in a conventional ball mill increasing the speed of rotation will increase the speed with which the balls move. Above a critical speed, the balls are pinned to the inner walls of the vial and do not fall down to exert any impact force [*Sur01*]. Therefore, the maximal speed should be just below this critical value so that the balls fall down from the maximal height to produce the maximal collision energy. Powder-to-ball weight ratios of 1:10 and 1:15 were used for SA – ball milling of $SmCo_5$ and $Nd_2Fe_{14}B$, respectively. The samples were ball-milled for different times ranging from 0.5 to 80 hours. The details about milling parameters are listed in table 2.1. The milling vials were gas tight and sealed inside an Ar-box to protect the powder from contact with air. The powder samples were handled in Ar-box later after milling. The samples obtained after SA – ball milling were washed several times with n-heptane and ethanol to remove the excess amount of surfactant and then dried in vacuum. A size-selection process was employed to

Table 2.1 Milling parameters used for the preparation of $SmCo_5$ and $Nd_2Fe_{14}B$ ultrafine particles and flakes.

Starting powder	**Surfactant**		**Solvent**		**Milling time^b (h)**	**Milling speed^c (rpm)**	**PBR^d**
	Type	**Amount (wt.%)^a**	**Type**	**Amount (wt.%)^a**			
$SmCo_5$	oleic acid	5	n-heptane	60	12	800	1:10
		10					
		50					
		10	n-heptane	60	12	400	
					80	200	
	polyvenylpyrrolidone	10	ethanol	60	12	800	
			ethanol	100	6	400	
d-HDDR $Nd_2Fe_{14}B$	oleic acid	50	n-heptane	60	14	400	1:15
						800	
			n-heptane	100	3	400	
			abs. ethanol	100			
			acetone	100			
	dry milling						

[a] weight percent of starting powder weight

[b] maximum milling time used

[c] rotational milling speed

[d] powder-to-ball weight ratio

separate nanoparticles and smaller flakes from the large micrometer-sized flakes. The SA – ball-milled samples were ultra-sonicated in heptane for around 15 minutes, the large particles and flakes (1-3 μm) were allowed to settle down on the bottom of the bottle. The upper portion of the solution containing nanometer-sized particles and flakes was transferred into another bottle. The new solution was further ultra-sonicated for 30 minutes and then centrifuged. Smaller nanoparticles floated in the upper part of the solution while larger nanoparticles and nanoflakes settled on the bottom.

Samples obtained after SA – ball milling were processed using heat-treatment and hot compaction. The heat-treatments were performed using a tube furnace under high vacuum (~10^{-4} mbar) at a heating rate of 10 K/min and the samples were allowed to cool in air. In some cases the samples were degased at around 200 ^{0}C using a turbo-pump to evaporate the surfactants and then heated to the required temperature for heat-treatments. Selected samples were hot-compacted using an in-house-built hydraulic hot press. The samples for hot-pressing were prepared using a graphite die of 5 mm diameter. The die filling and sealing was done in the Ar-box to protect the samples from air exposure. The hot compaction was performed at a pressure of 300 MPa at different temperatures in the range 400 to 750 ^{0}C. The density of hot-compacted samples was measured by pycnometer using distilled water as working liquid.

2.4 Structural characterization

The structural properties of starting, as-milled and heat-treated powders and hot-compacted samples were studied by X-ray diffractometry and electron microscopy.

2.4.1 X-ray diffraction

Phase identification, composition and structural parameters of the powder samples were investigated by X-ray diffractometry. Measurements were performed by using two types of X-ray diffractometers; Philips X'Pert PRO operating in reflection mode with Co K_α (weighted average wavelength $\lambda_{K\alpha}$ = 1.7902 Å) radiation equipped with a graphite monochromator, and a StoeStadi P system operating in the transmission mode with Mo $K_{\alpha 1}$ (λ = 0.7093 Å) radiation equipped with a curved Ge (*111*) monochromator. The measurements were performed at room temperature. A schematic representation of both reflection and transition modes is shown in figure 2.5.

The samples were prepared by spreading the powders on double-sided carbon tape and then covering them with a thin Kapton foil to prevent an air contact during measurement

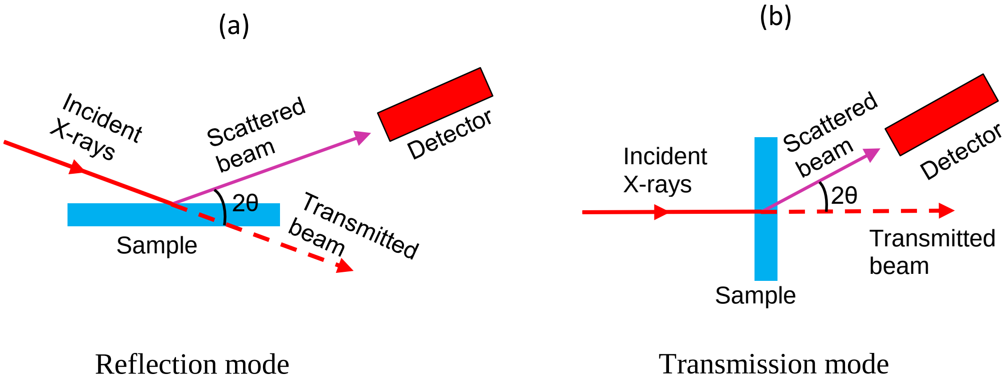

Figure 2.5 Schematic representations of (a) reflection and (b) transmission modes of X-ray diffraction.

in case of reflection mode. Magnetically-oriented samples were prepared by embedding the powders in a two-component Epofix resin. The embedded mixture was filled in a capsule and then oriented using an electromagnet with a magnetic field of 2 T. The embedded mixture was dried in presence of the applied magnetic field to lock in the orientation. Glass capillaries of inner diameter 0.2 mm and wall thickness of 0.01 mm were used to prepare samples for XRD measurements in transmission mode. The glass capillaries were filled and sealed in Ar-box to prevent any air contact.

Diffraction peaks in XRD patterns result from the crystallographic planes which are irradiated by the X-ray beam. The diffraction intensities occur at beam angles defined by Bragg’s law of diffraction:

$$2 \cdot d \ \cdot sin\theta = n \cdot \lambda \qquad (2.3)$$

where, d – spacing between crystallographic planes; θ – diffraction angle; n – integer and λ – wavelength.

The angle between the transmitted beam and the scattered beam is defined as 2θ. A XRD pattern is generated by plotting the intensity of scattered radiation as a function of 2θ. The XRD patterns are used for phase identification, grain size calculation, and lattice parameter estimation [*Cul01*].

The phase analysis was performed by using the PDF-2 powder diffraction database. In addition to phase analysis, Rietveld analysis [*Rie69*, *You93*] was also performed. In Rietveld analysis a model for the structure is built and the parameters in that model are refined to fit the measured pattern by the method of least squares. The procedure of model fitting is continued until the best fit between the model and the calculated pattern is obtained in an iterative process. Using this method, the weight fraction of the phases, their lattice parameters, crystallite size and strain can be calculated. The refinements were made using the X'Pert HighScore Plus software developed by PANalytical BV [*Hsp*]. The Scherrer formula was used to calculate the grain size based on the broadening of the peak. In this work the Willianson-Hall method was used which is based on the Scherrer equation and additionally takes into account the lattice strain effect which also influences the peak broadening [*Wil53*]. This method is expressed by:

$$B \cdot cos\theta \ = K \cdot \lambda / D + 2 \cdot \varepsilon \cdot sin\theta \qquad (2.4)$$

where, B – full width at half maxima (FWHM); K – Scherrer constant; D – crystallite size; λ – wavelength of x-ray irradiation, ε – lattice strain and θ – Bragg's angle.

In this method, $B \cdot cos\theta$ is plotted against $2 \cdot sin\theta$ applying a linear extrapolation. The particle size is calculated from $K \cdot \lambda / D$ which is given by the extrapolation at $B \cdot cos\theta$ = 0. The slope of the linear extrapolation gives an estimation of the lattice strain [*Kim99*]. This method was used to calculate the grain size and lattice strains of differently milled and heat-treated samples.

The XRD patterns of magnetically-oriented samples were used to determine the texture values of ball-milled $SmCo_5$ and $Nd_2Fe_{14}B$ sample. The texture values were determined by calculating the ratio of integrated intensities I_{002}/I_{111} for $SmCo_5$ and I_{006}/I_{105} for $Nd_2Fe_{14}B$ samples. The diffraction peaks (*002*) and (*111*) for $SmCo_5$ and (*006*) and (*105*) for $Nd_2Fe_{14}B$ were chosen for the texture determination for their high intensity in the case of magnetically-oriented samples.

2.4.2 Scanning electron microscopy

Scanning electron microscopy (SEM) provides higher resolution as compared to optical microscope. The resolution is a function of wavelength of the beam of the microscope: for an optical microscope this is 4000 Å, whereas for a SEM it is 50-200 Å. In SEM the electron beam interacts with the specimen and is scattered by different parts of the specimen in different ways producing secondary electrons, back scattered electrons, Auger electrons, cathodoluminescence or X-rays.

The SEM investigations were performed using a field emission gun scanning electron microscope, FEG-SEM LEO Gemini 1530 equipped with energy dispersive X-ray (EDX) analysis. The secondary electron (SE) and the backscattered electron (BSE) modes were used to study the morphology of the powder particles and bulk hot-compacted samples. The use of backscattered electrons allows to detect the contrast between areas with different chemical compositions.

The samples for the SEM analysis were prepared by spreading the powder particles on double sided conducting carbon tape. The hot-compacted samples were ground on sand paper and polished on a cloth-covered wheel using diamond paste with water-free lubricant for SEM analysis. The samples were sputtered with Au/Pd alloy to make them electrically conductive.

2.4.3 Transmission electron microscopy

Transmission electron microscopy (TEM) yields morphological, compositional and crystallographic information of a specimen on the nanometer scale. In TEM, electrons from the emission gun are transmitted through a very thin sample and generate an image of the internal structure of the sample. Thicker areas and areas containing heavier elements appear darker due to more intense scattering by the elements. In addition, diffraction from crystal planes leads to a diffraction pattern characteristic for the crystal structure and provides the orientation of the imaged grains. Depending on whether the transmitted or diffracted beam is chosen, the resultant image is called a bright-field or a dark-field image, respectively. The size and shape of nanometer-sized particles and flakes were studied. High-resolution (HR) TEM imaging provides information about the crystal orientation and interplanar spacing in the crystals.

TEM was used to obtain electron diffraction (ED) patterns of selected samples. The ED patterns result from the elastic scattering of electron beam by the sample lattice obeying the Bragg's law [*Wil09*]. The ED patterns from selected regions of the sample known as selected area electron diffraction (SEAD) patterns can be used to identify single-crystalline, polycrystalline and amorphous regions of the samples generating bright spots, small spots making a ring and diffuse ring, respectively. The SAED patterns in form of rings consisting of small arcs instead of spots are obtained for a textured-polycrystalline sample [*Ege05*]. Additionally, diffraction patterns can be formed by applying fast Fourier transformation (FFT) to a high-resolution TEM image (lattice image) [*Wil09*]. The FFT patterns were used to observe the misorientation of nanometer-sized grains in the polycrystalline flakes in this work.

The TEM investigations were performed to study the morphological and crystallographic characteristics of nanoparticles and flakes prepared by SA – ball milling. The TEM samples were prepared by dispersing the nanoparticles and nanoflakes in solvents (ethanol or heptane) and dropping one or two drops of the dispersion onto carbon-coated copper grids. The TEM samples with large micrometer- or sub-micrometer-sized particles and flakes were prepared by mixing the powder particles with TiN nanoparticles (size < 15 nm). The TiN nanoparticles were used to provide a support media between sample particles and the resin which reduces the fast milling of the rather weak resin. The mixture was embedded in resin, and small balls of around 3 mm diameter were formed. The embedded sample was cut in form of small slices which were thinned using diamond polishing and then ion-milled to be electron transparent. A FEI Technai G2 20 microscope operated at 200 kV was used in this work.

2.5 Magnetic characterization

Magnetic properties of different samples were studied by vibrating sample magnetometry (VSM) and superconducting quantum interference device (SQUID). Specimens were produced by mixing the powder particles with paraffin wax and melting the mixture at around 60 ^{0}C in an acrylic capsule and cool later to solidify the wax. The paraffin wax was able to inhibit any movement of the particles during the measurement in presence of a strong magnetic field up to room temperature. Hysteresis loops of the samples were measured using VSM and SQUID (Quantum Design MPMS-5S) with a maximum applied field of 9 T and 4.5 T, respectively. The powder particles were oriented in a 2 T magnetic field using an electromagnet. Capsules containing paraffin wax and powder were heated to melt the wax and then cooled in presence of an applied magnetic field. Hysteresis loops of the oriented samples were recorded in both parallel and perpendicular directions of the orienting magnetic field in order to determine the degree of texture or degree of orientation.

The spin reorientation transition temperature was determined from ac-susceptibility measurements using the physical property measurement system (PPMS) device. AC-susceptibility (χ') was measured as a function of temperature in the temperature range of 10-300 K, and the spin reorientation temperatures were determined from the peak values of $d\chi'/dT$ *vs* T curves.

Chapter 3

Fabrication mechanism of flakes and nanoparticles

In the last couple of years, there has been some interest in the processing of hard magnetic RETM nanoparticles and nanoflakes for their potential use in making future high-energy-density textured nanocomposite magnets or as an attractive component with superior magnetic properties for advanced permanent magnet applications [*Cui11, Cha06, Pou13, Lew12*]. Alongside with various potential applications and the industrial need for hard magnetic nanoparticles made from Sm-Co and Nd-Fe-B alloys, it is of great scientific interest to study and understand the fundamental properties of these nanometer-size objects. This chapter is focused on understanding the fabrication mechanism of micrometer- and nanometer-sized particles and flakes of $SmCo_5$ and $Nd_2Fe_{14}B$ obtained by the novel technique of surfactant-assisted ball milling.

3.1 Morphological and structural evolution

Ball milling is basically used for mechanical alloying and grinding of powder particles. In usual grinding processes the particle size decreases at the start of the process and prolonged milling results in agglomeration and re-welding of the particles [*Sur01*]. Thus there is a critical lower limit of the particle size. The use of surfactants during milling is beneficial to reduce the particle size even further by preventing re-welding and agglomeration. Surfactants provide a capping layer over the particles and reduce the friction between particles and thus prevent the re-welding. As a result, micrometer- or nanometer-sized flakes and particles can be obtained using SA – ball milling. The evolution of morphology and structural properties of flakes and particles of $SmCo_5$ and $Nd_2Fe_{14}B$ are discussed in this section.

3.1.1 $SmCo_5$ nanoflakes and nanoparticles

The starting $SmCo_5$ powders of particle size ranging from 2 to 40 μm are shown in figure 3.1. These fine-grained particles were prepared by the co-reduction method. Figures 3.2 (a-d) show the morphological evolution of $SmCo_5$ nanoflakes obtained after SA – ball milling with 10 wt.% oleic acid and 60 wt.% n-heptane at 800 rpm. As shown in figure 3.2 (a), after 0.5 h of SA – ball milling, the initially 2-40 μm large particles are crushed down to particles of 3 μm average diameter. This size reduction was made possible *via* intergranular fracture of fine-grained starting $SmCo_5$ powder. Some of these particles transformed to flakes and broke into smaller particles (< 2 μm) as well. The thickness of the flakes formed after a 0.5 h of milling was around 500 nm. Further milling resulted in flaking of small particles and a decrease in the size of previously-formed flakes (figures 3.2 (b) and (c)). It was observed that almost all the particles transformed to flakes with a diameter ranging from 100 nm to 2 μm and a thickness of around 20 nm after 5 h of milling. For comparison the flakes obtained in the current work were smaller in diameter and thickness than those reported by Poudyal *et al.* [*Pou11*] and Cui *et al.* [*Cui11*] who obtained $SmCo_5$ flakes of 5 to 10 μm diameter with average thickness of 50 nm under similar ball milling conditions. Prolonged ball milling results in a decrease of the size and thickness of the flakes. As shown in figure 3.2 (d), the flakes obtained after 12 h of milling were arranged face-to-face and form a ring structure which is possible due to the crystallographically anisotropic nature and magnetostatic interaction between the flakes. The face-to-face arrangement of flakes indicates the presence of an out-of-plane crystallographic texture in the flakes.

The presence of surfactants during ball milling facilitates the formation of flakes. The particles are covered with a surfactant layer as soon as the freshly-fractured surfaces are formed; the surfactant molecules get adsorbed on to the new surfaces of the particles. The adsorption or attachment of the surfactant occurs through a chemical bonding between the oxygen of polar head groups and the particle surfaces [*Yan07*, *Gab10*] (see figure 2.3).

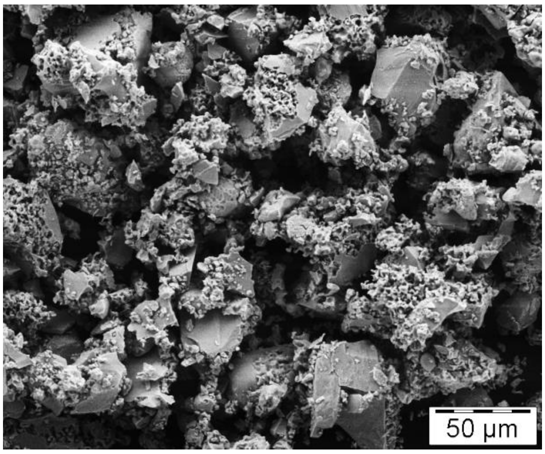

Figure 3.1 Secondary electron SEM image of starting $SmCo_5$ powder.

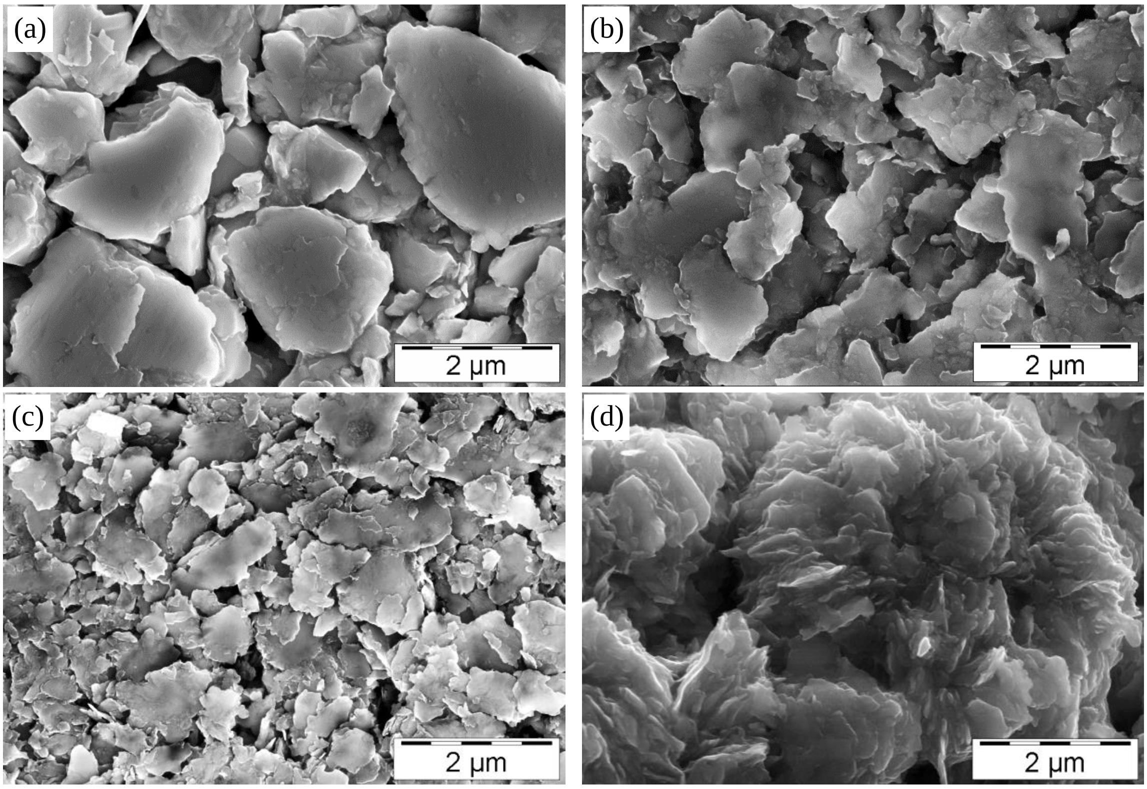

Figure 3.2 Secondary electron SEM images showing the morphological evolution of $SmCo_5$ flakes obtained after SA – ball milling for (a) 0.5 h, (b) 2 h, (c) 5 h and (d) 12 h in 10 wt.% oleic acid and 60 wt.% n-heptane at 800 rpm.

Due to the coating of surfactant and repulsion between hydrocarbon tails of the surfactant molecules, the re-welding of the crushed particles is greatly reduced which allows the formation of smaller and separated particles.

The samples obtained after SA – ball milling had a significant size variation consisting of 2 μm average diameter of flakes to 15 nm of nanoparticles. It is very difficult to completely separate the small flakes and nanoparticles from the mixture because of the strong magnetostatic interaction between the textured flakes and the nanoparticles. An attempt was made to separate the small flakes and nanoparticles *via* the size-selection process using ultra-sonication. The sample was ultra-sonicated in n-heptane in a glass bottle for 10 minutes. The ultra-sonication resulted in a dispersion of the nanoparticles and small flakes in the solution. Large micrometer-sized flakes settled very quickly on the bottom of the bottle due to gravitational force, some nanoparticles and small flakes also settled down with the big flakes due to the magnetostatic attraction. The upper part of solution containing a small amount of nanoparticles and small flakes was transferred into another bottle and was ultra-sonicated again for 5 minutes. The small flakes settled down after 30 seconds, whereas

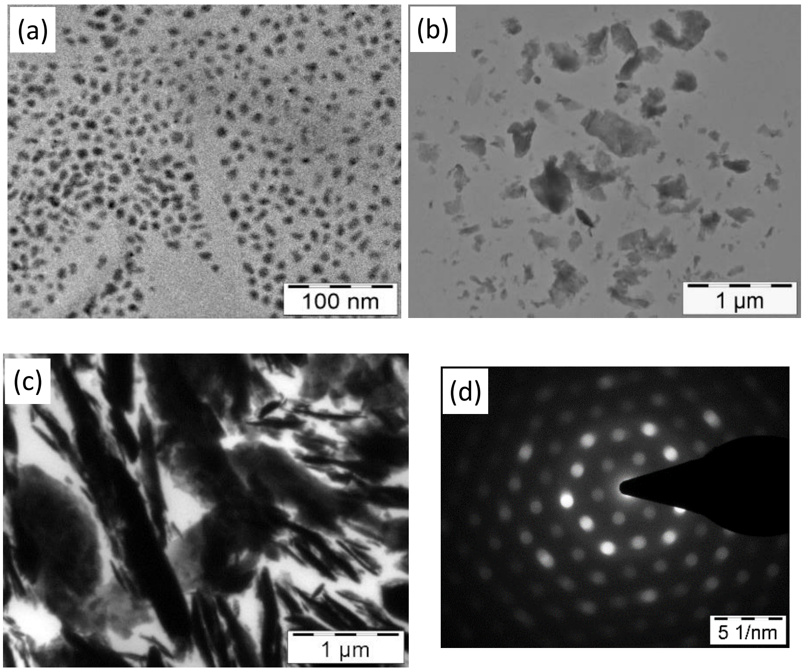

Figure 3.3 Bright field TEM images of $SmCo_5$ nanoparticles and flakes obtained after the size-selection process. (a) Nanoparticles, (b) smaller (100-500 nm) flakes (c) sediment particles and (d) nanobeam diffraction pattern from single-crystalline flakes in (c).

the nanoparticles were dispersed in the solution which was taken out into another bottle. Using this size-selection process, it was possible to separate a small amount of small flakes and nanoparticles from the mixture of micrometer-sized flakes. The fraction of nanoparticles and small flakes in the ball-milled sample depends on the milling time and the milling energy. An increase of the fraction of nanoparticles and small flakes was observed with increasing milling energy and milling time. As a rough estimate, the fraction of nanoparticles and small flakes was approximately 10 and 20 wt.%, respectively, of the slurry sample obtained after SA – ball milling of $SmCo_5$ powder at 800 rpm for 12 h. One or two drops of the blackish solutions containing nanoparticles and small flakes were put on carbon-coated Cu grids for TEM analysis. As shown in figures 3.3 (a) and (b), nanoparticles of average diameter 15 nm and nanoflakes of diameter 100-500 nm were obtained using this size-selection process. The sedimented particles were washed and then embedded in resin to prepare TEM samples by polishing and ion milling. Figure 3.3 (c) shows nanoflakes with a diameter ranging from 100 nm to 2 μm and an average thickness of 20 nm. It was also observed that micrometer and sub-micrometer flakes were polycrystalline on the edges, but single-crystalline or with preferred *c*-axis out-of-plane orientation in the middle. The nano-beam diffraction pattern in figure 3.3 (d), which comes from different inner regions of a micrometer-sized flake, shows a single crystal diffraction pattern with (*001*) zone axis.

TEM investigations were performed on the SA – ball-milled flakes of $SmCo_5$ in order to understand the flaking mechanism and the formation of anisotropic nanoparticles. Smaller flakes (< 500 nm) were separated from a 12 h milled sample using the size-selection process and some of the flakes were analyzed with the help of high-resolution TEM imaging and SAED patterns. Figures 3.4 (a) and (b) show TEM images of two different polycrystalline flakes. The polycrystallization of initial single-crystalline flakes occurs possibly due to deformation and introduction of dislocations (crystallographic defect or irregularity within a crystal structure) caused by the repeated high impact collisions between the flakes and milling balls [*Sur01*]. It can be assumed that after continued milling, the average atomic level strain increased due to an increasing dislocation density, and at a certain dislocation density within these heavily-strained regions the crystal disintegrated into sub-grains that are separated by small-angle grain boundaries [*Fec95*, *Vas04*]. This phenomena can result in a decrease of the lattice strain. The sub-grains formed this way had nanometer dimensions, often between 10 and 50 nm. On further processing, the grain size of thin flakes decreases steadily and the small-angle grain boundaries are transformed to large-angle grain boundaries by grain rotation. The grain boundary region gets amorphized and becomes weaker during this process, continued SA – ball milling can result in breaking of the individual grains along the grain boundaries into anisotropic nanoparticles. As can be seen in figure 3.4 (c), the size of nanoparticles corresponds to the grain size of the thin flake in figure 3.4 (b). HRTEM image in figure 3.4 (d) shows nanometer-sized grains having a small-angle misorientation. A FFT image of the selected region in the inset shows a slightly shifted spot pattern indicating an in-plane rotation of nanometer-sized grains. It is evident in figure 3.4 (e) that for a longer milled and thinner flake the spread in the spots of FFT pattern is relatively increased, confirming that the small-angle grain boundaries transform into large-angle grain boundaries after successive milling. The SAED pattern of a single sub-micrometer-sized flake, which consists of many nanometer-sized grains, shows an arc-pattern (figure 3.4 (f)). The six-fold symmetric arc patterns with missing (*00l*)-type diffractions represent an in-plane texture and a preferential *c*-axis out-of-plane orientation.

The formation of flakes and nanoparticles can be understood as follows: In the beginning of SA – ball milling, big isotropic polycrystalline $SmCo_5$ particles (2-40 μm) fragment into micrometer-sized single crystal irregular particles by fracturing and crushing. Successive milling results in a further breaking of the single-crystalline irregular particles. These particles transform into flakes *via* cleaving along the easy-glide (*001*) basal planes (figure 3.5) to form micrometer-sized flakes. The continuation of crushing and cleavage along (*001*) planes results in a decrease in flake size and thickness. Furthermore, a lot of defects and dislocations are introduced in the flakes during this process. The defect and dislocation density increase with successive milling which results in the development of

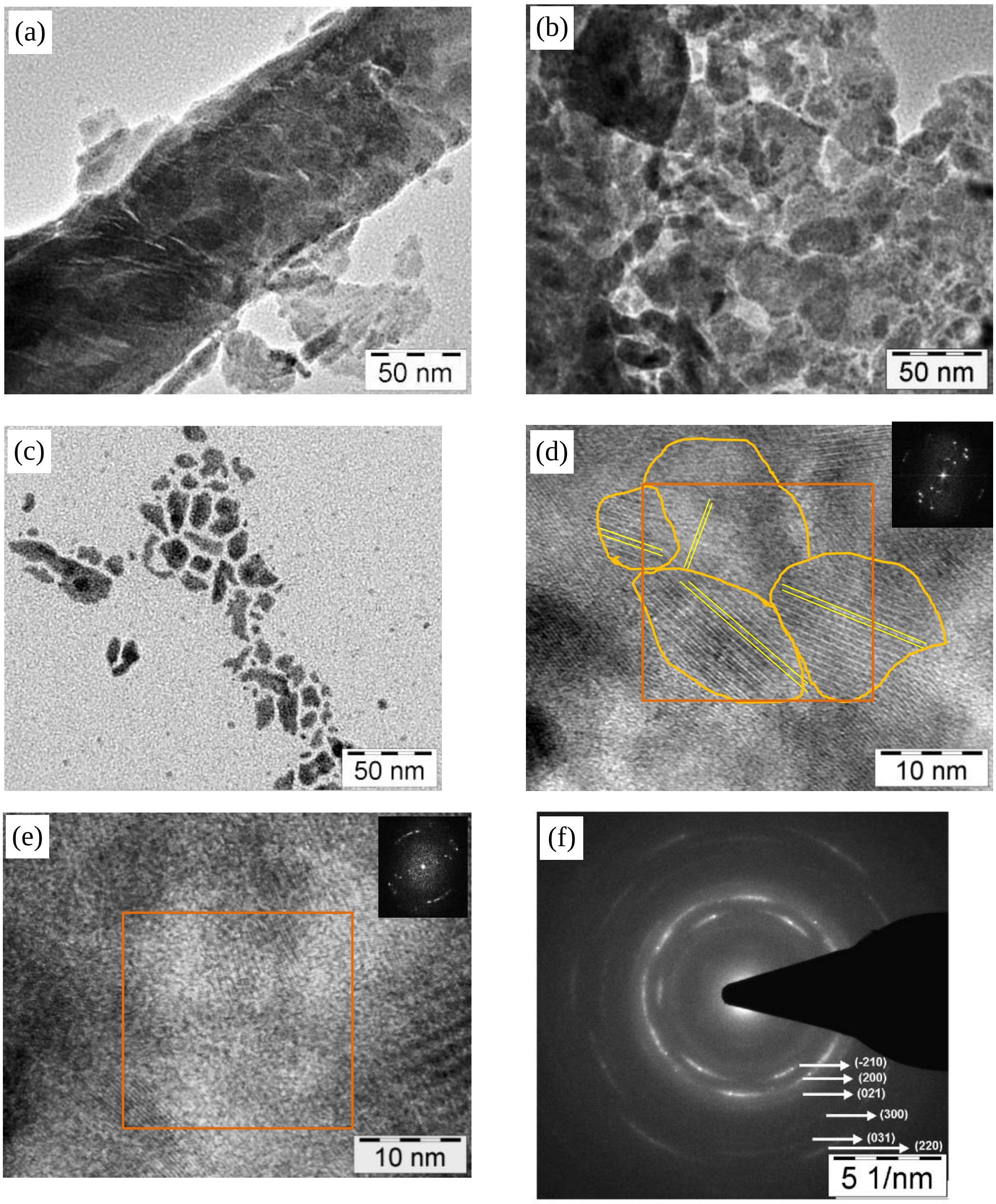

Figure 3.4 Bright field TEM images of (a) sub-micrometer long flake, (b) sub-micrometer long flake with increased number of defects and dislocations, (c) isolated anisotropic nanoparticles after breaking the crystals of flakes in (b), HRTEM image of a flake showing (d) grains of ~15 nm size with small-angle grain boundaries, the inset is the FFT image from a selected region showing slightly shifted spots, (e) HRTEM image of a thin flake with smaller (5 nm) grains, the inset FFT image shows a broader distribution of spots, (f) SAED pattern from a single polycrystalline flake showing in-plane texture with preferred *c*-axis out-of-plane orientation of nanometer size grains.

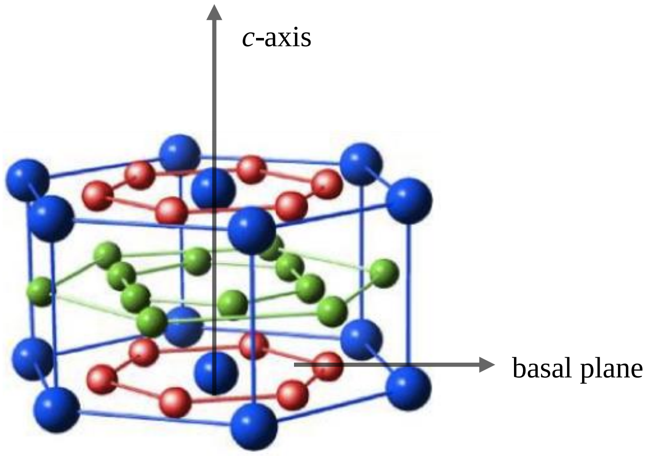

Figure 3.5 Crystal structure of hexagonal $SmCo_5$ showing atomic positions and basal plane [*Mpi*].

small-angle grain boundaries in the micrometer- or sub-micrometer-sized flakes. With continued ball milling, the diameter and thickness of the flakes become smaller and nanometer-sized grains are formed continuously through in-plane rotation of different parts of the bigger grains *via* recrystallization [*Vas04*]. Consequently, the resulting polycrystalline flakes have a well-preserved crystal order and a strong (*00l*) out-of-plane texture inherited from its single-crystal precursors. Finally, textured polycrystalline $SmCo_5$ nanoflakes are formed. The continuous decrease in thickness of the polycrystalline nanoflakes during the ball milling is believed to be mainly due to an enhanced ductility exhibited by brittle materials in a nanocrystalline state [*Jia04*] rather than a basal cleavage of the easy-glide (*00l*) planes which dominates in the stage of formation of single-crystal micrometer- and sub-micrometer-sized flakes. The polycrystalline flakes break along the grain boundaries of the nanometer-sized crystals and thus the nanoparticles are formed.

The X-ray diffraction patterns of SA – ball-milled $SmCo_5$ powders shown in figure 3.6 (a) reveal that all the as-milled samples preserve the standard $CaCu_5$-type crystal structure. It is evident from the plot that no peaks from oxides or pure cobalt are detected in the diffraction patterns, indicating that the SA – ball-milled powders have been effectively protected by surfactant coating. The diffraction patterns also confirm that no detectable contamination or decomposition has occurred during the milling process. It is clear from the XRD patterns that the peak intensity decreases and the peak broadening increases with increasing milling time, which indicates an increase in induced micro-strain, a decrease in grain size and an increase in the degree of amorphization. Size/strain analysis was performed on different samples using the X'Pert HighScore Plus software. Micro-strain values of

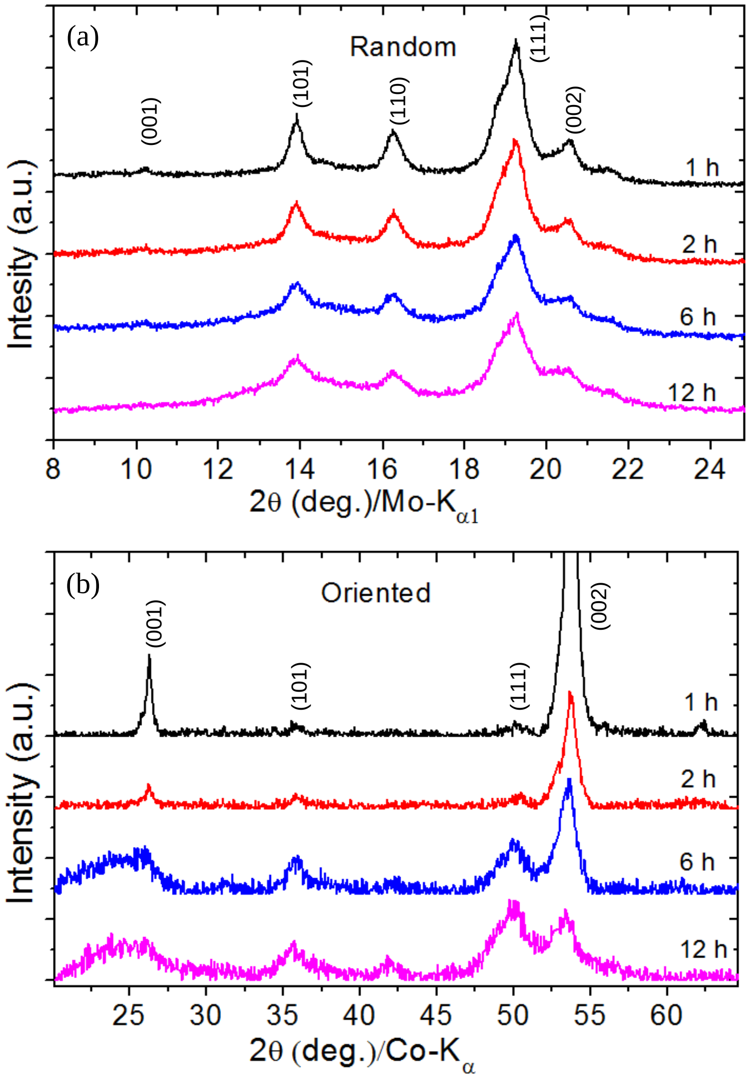

Figure 3.6 XRD patterns of (a) random and (b) magnetically-oriented $SmCo_5$ flakes obtained after SA – ball milling with 10 wt.% oleic acid + 60 wt.% n-heptane at 800 rpm.

0.52(4)%, 0.70(6)%, 0.89(3)% and 1.12(9)% were obtained for 1 h, 2 h, 6 h and 12 h milled samples, respectively. The grain sizes were calculated as 16(1) nm, 13(1) nm, 9(2) nm and 5(2) nm for 1 h, 2 h, 6 h and 12 h milled samples, respectively (values within the parentheses represent the standard deviations). SA – ball-milled samples were embedded in resin and then oriented in a 2 T magnetic field. The XRD patterns of oriented samples were recorded on the surface perpendicular to the applied magnetic field. The diffraction patterns show strong *(00l)-type* peaks for the oriented samples shown in figure 3.6 (b). This shows that flakes obtained after SA – ball milling have a strong *c*-axis texture. The value of texture was determined by calculating the ratio of the integrated intensities of the (*002*) and (*111*) XRD peaks for magnetically aligned samples. The value of I_{002}/I_{111} was 0.2 for non-aligned (isotropic) $SmCo_5$ powder. The texture value was found to decrease with increase in milling time; I_{002}/I_{111} values of 37, 9.0, 4.0, 2.3 and 0.9 were obtained for 1, 2, 4, 6 and 12 h ball-milled samples, respectively.

3.1.2 $Nd_2Fe_{14}B$ single-crystalline particles, textured nanoflakes and nanoparticles

Figure 3.7 (a) shows the SEM image of d-HDDR processed $Nd_2Fe_{14}B$ powders of particle diameter 50-200 μm. The magnified image shows that the polycrystalline particles have grains of size ranging from 200 to 500 nm (figure 3.7 (b)). These fine-grained polycrystalline powders were used as precursor material for the preparation of sub-micrometer-sized single-crystalline particles, textured polycrystalline nanoflakes and nanoparticles by SA – ball milling.

The starting powder of 50 to 200 μm particle size was ball-milled with oleic acid (50 wt.%) and n-heptane (60 wt.%) at 400 rpm up to 6 h and then the milling speed was increased to 800 rpm and the powder was further milled up to 14 h. Figure 3.8 shows the morphological evolution of $Nd_2Fe_{14}B$ particles with milling time. In the beginning, after 0.5 h of milling, large polycrystalline particles break down into smaller particles of 1-3 μm in size. Some of these particles contain only a few (*e.g.* <10) grains, while larger particles contain many (~100) grains (figure 3.8(*a*)). Successive milling results in further crushing and breaking of micrometer-sized particles. As shown in figure 3.8 (b), some micrometer-sized polycrystalline particles mixed with isolated sub-micrometer-sized single-crystalline particles with clear edges are obtained. Almost all the particles are single-crystalline with sizes ranging from 200 to 500 nm after a milling of 4 h (figures 3.8(*c*)). Further milling at 400 rpm causes surface damage and an increase in the fraction of nanoparticles of size around 20 nm (figure 3.8 (d)). The milling speed was increased to 800 rpm in order to

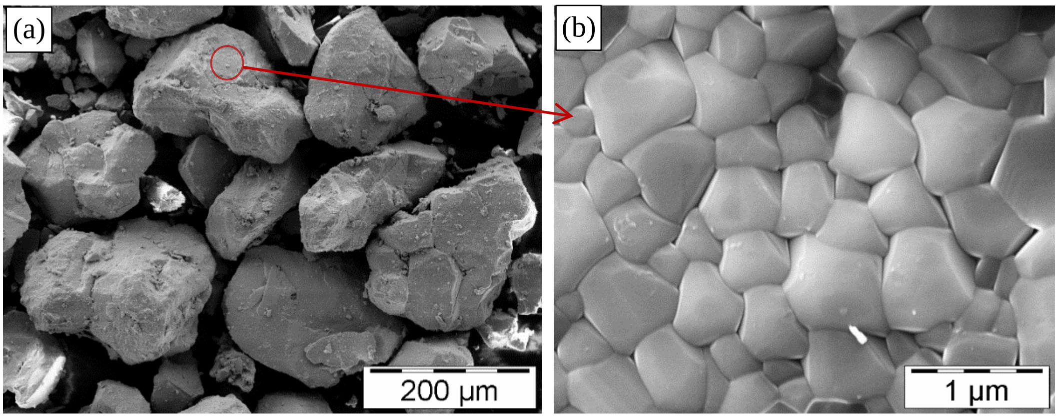

Figure 3.7 Secondary electron SEM images of (*a*) un-milled d-HDDR-$Nd_2Fe_{14}B$ powder and (*b*) high-resolution image of a selected region in (*a*) showing the grain sizes.

increase the milling energy to further break the single-crystalline particles into nanoparticles. The increase in milling energy results in an increase of the impact energy between the particles and milling balls and, because of this increased impact, the single-crystalline particles start transforming to polycrystalline flakes (figures 3.8 (e) and (f))

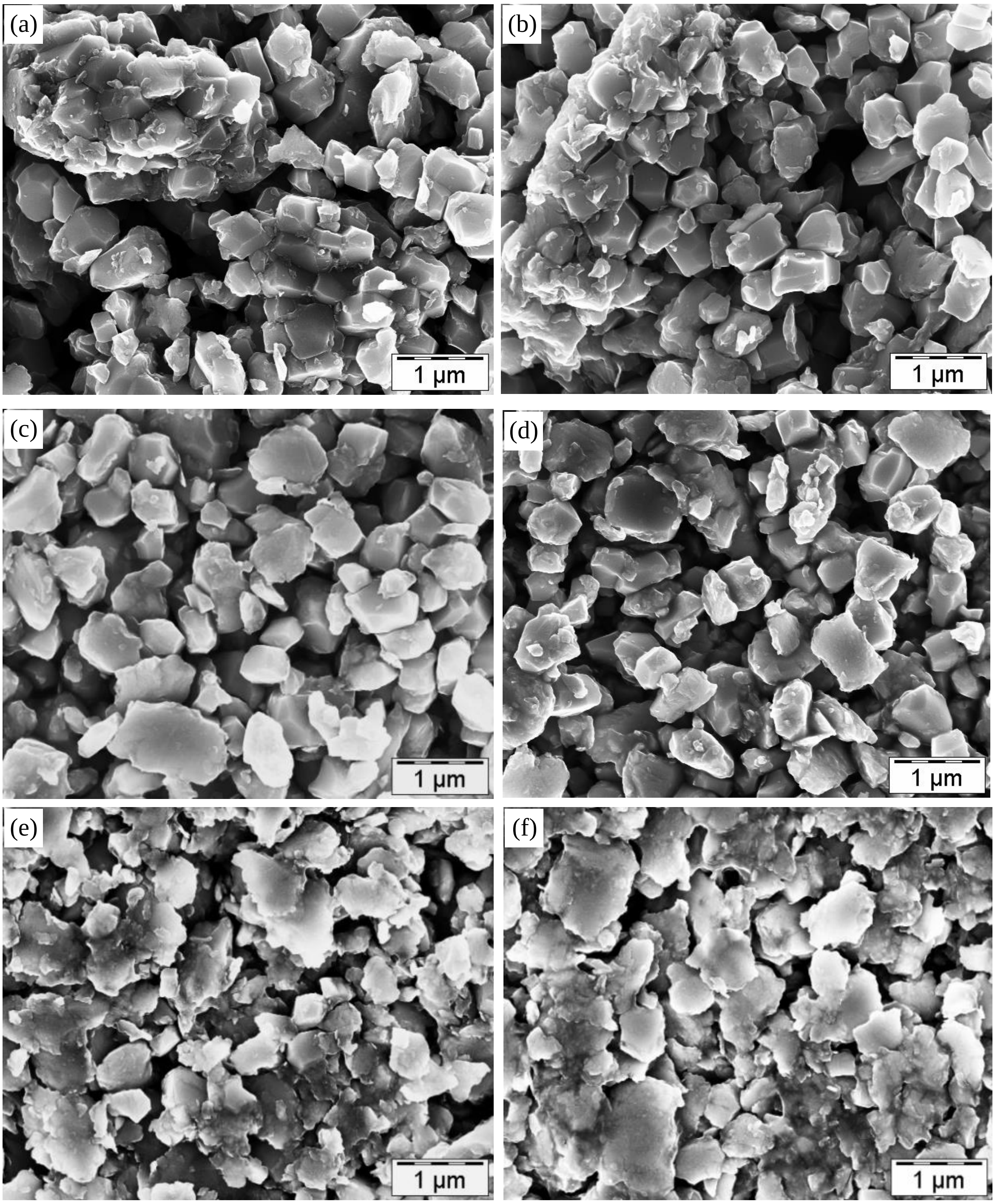

Figure 3.8 Secondary electron SEM images showing morphology evolution of SA – ball-milled d-HDDR-$Nd_2Fe_{14}B$ powder in 50 wt.% oleic acid and 60 wt.% n-heptane for (a) 0.5 h, (b) 2.0 h, (c) 4.0 h, (d) 6.0 h at 400 rpm, and (e) 9 h and (f) 14.0 h at 800 rpm.

instead of nanoparticles. Flakes of 0.5-1.0 μm diameter and 20-100 nm thicknesses were obtained after a milling of 14 h. As reported by Gabay *et al.* [*Gab10*] and Cui *et al.* [*Cui11*], SA – ball milling of arc-melted $Nd_2Fe_{14}B$ resulted in formation of micrometer-sized single-crystalline flakes. The single-crystalline flakes had transformed to micrometer-sized polycrystalline flakes [*Gab10, Cui11*]. Cui *et al.* prepared $Nd_2Fe_{14}B$ particles/flakes of 0.5-35.0 μm diameter by SA – ball milling after processing times ranging from 0.25 to 6 h, where single-crystalline flakes of 1-14 μm diameter and 250-980 nm thickness were obtained for 2 h of milling. In another study, a two-step ball milling was employed to prepare $Nd_2Fe_{14}B$ flakes of 2-20 μm diameter and 25-100 nm thickness [*Akd10*]. In the case of HDDR-processed $Nd_2Fe_{14}B$ powder, SA – ball milling resulted in a separation of individual grains into single-crystalline sub-micrometer particles with a very low particle size distribution (200-500 nm). At higher milling energy these sub-micrometer particles transformed into polycrystalline flakes. The separation of individual grains is attributed to the intergranular fracture mode of $Nd_2Fe_{14}B$ magnets due to the presence of weaker Nd-rich grain boundaries [*Jia01*]. The flaking of single-crystalline particles after high-energy milling is possibly due to the damaged surface and the cleavage along the (*110*) plane of irregular single-crystalline particles [*Cui12a*]. The cleaving along (*110*) plane is deduced by correlating the results from XRD patterns and the SEM images of magnetically-oriented flakes. The SEM image of magnetically-oriented $Nd_2Fe_{14}B$ flakes (figure 3.9) shows edge-

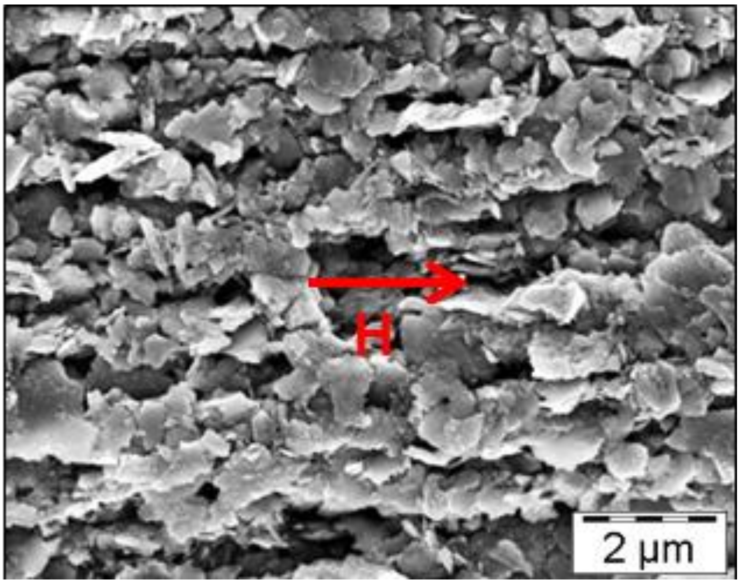

Figure 3.9 Secondary electron SEM image of magnetically-oriented $Nd_2Fe_{14}B$ flakes obtained after 14.0 h of SA – ball milling showing edge-to-edge alignment of the flakes. The arrow indicates the direction of applied magnetic field.

to-edge alignment of the flakes and the XRD pattern (figure 3.12 (b)) recorded on the surface perpendicular to the direction of the orienting magnetic field indicates (*00l*) in-plane texture. These results indicate that the $Nd_2Fe_{14}B$ flakes form by cleavage along the (*110*) plane. Further, the flaking can also be a result of an increased ductility at the nanocrystalline stage.

TEM investigation was performed on single-crystalline particles (4 h) and flakes (14 h) to study the formation mechanism of flakes and nanoparticles. Similar to the case of

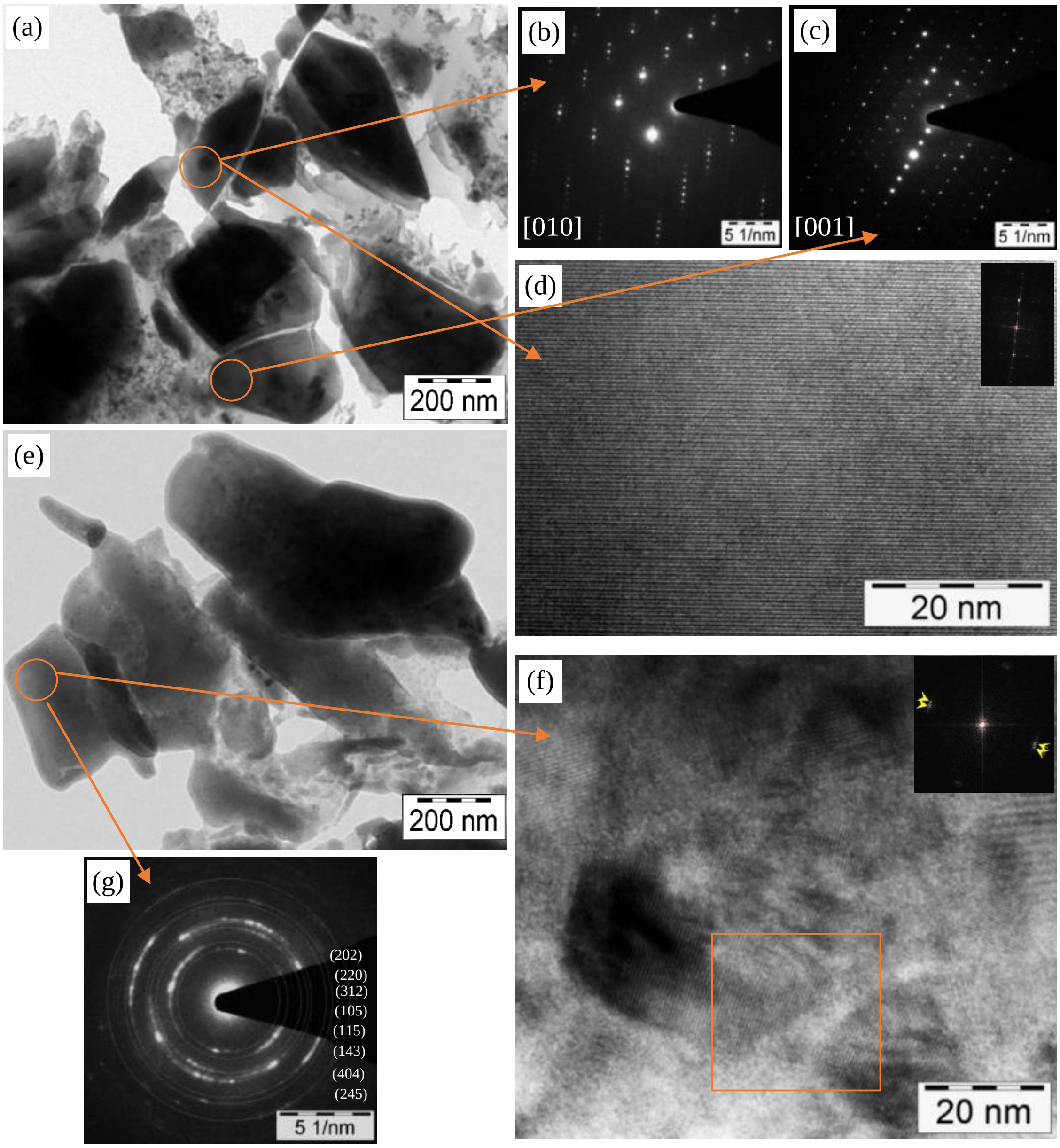

Figure 3.10 (a) Bright field TEM image, (b), (c) SAED patterns, (d) HRTEM image of particles obtained after 4 h of SA - milling (inset is the FFT image), (e) bright field TEM image, (f) HRTEM image and (g) SAED pattern of flakes obtained after 14 h of SA - milling d-HDDR-$Nd_2Fe_{14}B$ powder in 50 wt.% oleic acid and 60 wt.% n-heptane.

$SmCo_5$ samples, it was possible to separate small flakes (20-100 nm) and nanoparticles from the mixture of sub-micrometer flakes. The bright field TEM image in figure 3.10 (*a*) shows ultrafine particles and flakes obtained after 4 h of milling. These particles resemble the grains shown in figure 3.7 (b) and the size of particles is in agreement to those observed with SEM images (figure 3.8 (c)). SAED patterns from different particles shown in figures 3.10 (b) and (c) and the HRTEM image in figure 3.10 (d) (with FFT image inside) confirm the single-crystalline nature of particles obtained after 4 h of SA – ball milling. Figure 3.10 (*e*) shows a bright field TEM image of flakes obtained after 14 h of SA – ball milling. These flakes are similar to the flakes shown in the SEM image in figure 3.8 (e). An HRTEM image (figure 3.10 (f)) from a selected region of the flake shows its polycrystalline nature. The nanometer-sized grains of the flake are misoriented with small angles which are visible in the FFT image (inset of figure 3.8 (f)) in terms of slightly shifted spots. Successive milling result in a formation of large-angle grain boundaries. A SAED pattern of the selected region of the flake is shown in figure 3.10 (g). The SAED pattern consists of circular arcs instead

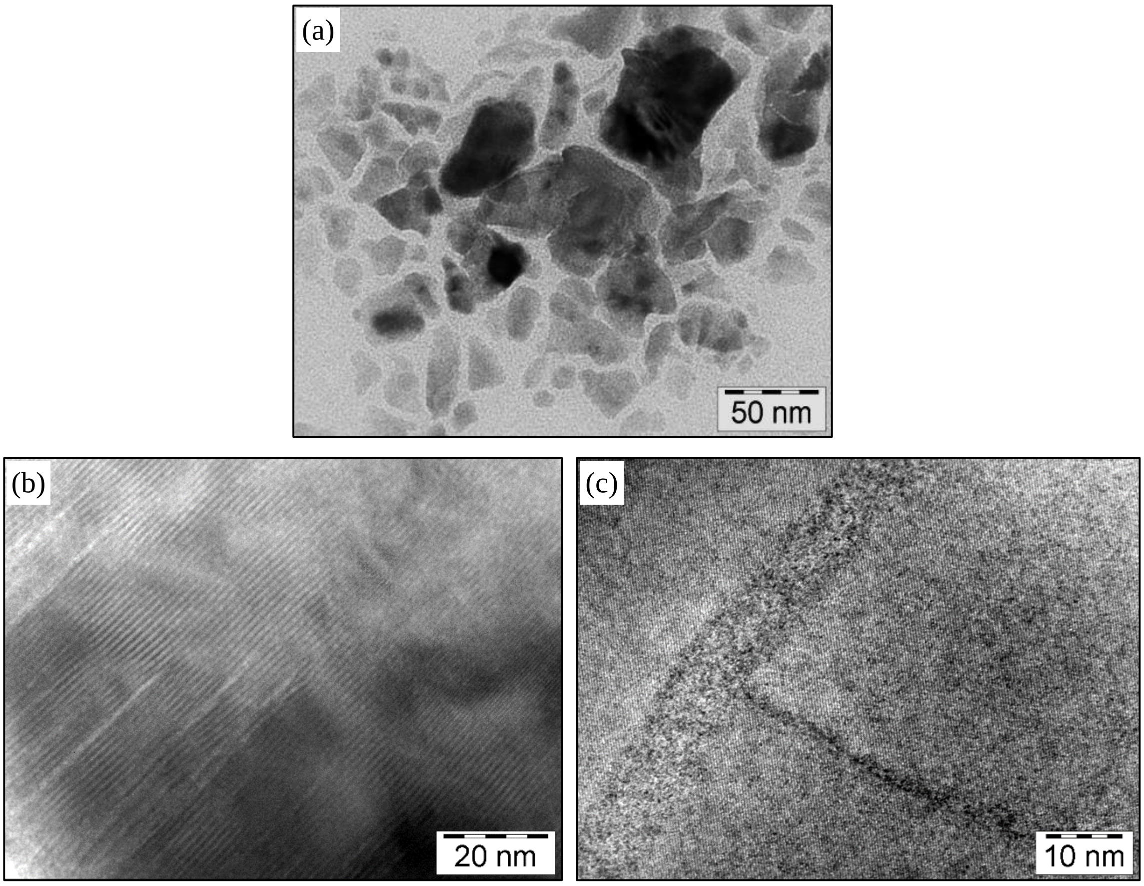

Figure 3.11 Bright field TEM images showing (a) Anisotropic $Nd_2Fe_{14}B$ nanoparticles, (b) and (c) defects observed in the $Nd_2Fe_{14}B$ flakes.

of complete rings or spots. The presence of arcs indicates an in-plane texture of polycrystalline flakes. Small nanometer size (10-500 nm) anisotropic particles and flakes of $Nd_2Fe_{14}B$ were separated from the mixture of 14-h-milled samples using the size-selection process. Figure 3.11 (a) shows the bright field TEM image of such particles and flakes. The formation of these nanoparticles and flakes is possibly due to the breaking of sub-micrometer flakes along the deformed regions [*Mie07, Hua09*]. Further, the breaking of sub-micrometer- and nanometer-sized flakes can occur due to the presence of defects and deformations as shown in figures 3.11 (b) and (c).

XRD patterns of random and magnetically-oriented samples obtained after SA – ball milling for 0-14 h are shown in figures 3.12 (a) and (b). All the as-milled samples preserve the standard tetragonal $Nd_2Fe_{14}B$ crystal structure. No significant difference in the XRD peak profiles in terms of peak broadening is visible for low-energy ball milling (400 rpm) which indicates that there is no significant reduction in grain size. As shown in figures 3.8 (a)-(c), at this milling energy, the large polycrystalline particles (figure 3.7 (a)) fragment into small particles consisting of a few (< 10) grains and then split into isolated single-crystalline particles. The XRD peaks slightly broaden and shift to lower 2θ values in the case of samples milled for 9 and 14 h at 800 rpm. The peak broadening and the shift is assumed to be due to the induced micro-strain and reduction of grain size after high-energy ball milling at 800 rpm. Size/strain analysis was performed on different samples with the help of X'Pert HighScore Plus software. Micro-strain values of 0.08(3)%, 0.09(5)%, 0.14(3)%, 0.15(7)%, 0.57(9)% and 0.75(8)% were obtained for 0 h, 1 h, 4 h, 6 h, 9 h and 14 h ball-milled samples, respectively. The calculated average crystallite size for 9 and 14 h ball-milled samples was 20(1) nm and 12(1) nm, respectively. As it can be seen in the SEM and TEM images crystallite sizes for 0-6 h milled samples are larger than 100 nm and not relevant for the crystallite size determination from XRD peak broadening. High-energy milling at 800 rpm causes rapid crushing of particles and provides high impact energy. As a result, single-crystalline particles get transformed into textured polycrystalline flakes. As shown in figures 3.12 (*a*) and (*b*), after a milling of 9 and 14 h the XRD peak intensities decrease and the become broadened, which is attributed to the formation of fine crystallites in the flakes (discussed earlier in this section), however the tetragonal structure of $Nd_2Fe_{14}B$ is maintained. XRD patterns of magnetically-oriented samples were recorded on the surface perpendicular to the applied magnetic field using Co-K_α radiation in reflection mode. As

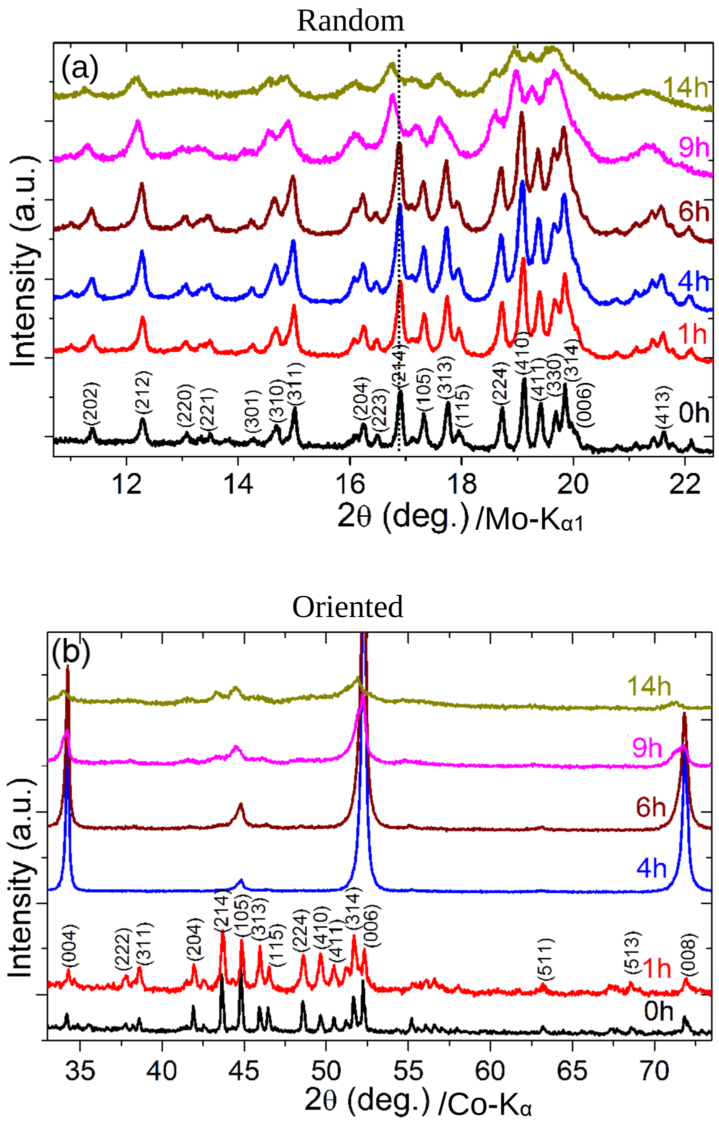

Figure 3.12 XRD patterns of (a) random and (b) magnetically-oriented $Nd_2Fe_{14}B$ particles obtained after SA – ball milling with 50 wt.% oleic acid + 60 wt.% n-heptane at 400 rpm up to 6 h and then at 800 rpm.

shown in figure 3.12 (*b*), an enhanced intensity of (*00l*)-type peaks is obtained for all milled samples of magnetically-oriented particles as compared to that of un-milled samples, indicating that the magnetic easy-axis of the particles and flakes is in *c*-axis direction. The highest intensity (*00l*) peaks for the sample milled for 4 h is signaled by an improved alignment of single-crystalline particles. The texture value for samples of magnetically-oriented particles was determined by calculating the ratio (I_{006}/I_{105}) of integral intensities of (*006*) and (*105*) peaks. For random isotropic powder, the I_{006}/I_{105} value is 0.5, whereas oriented un-milled powder shows a I_{006}/I_{105} value of 0.8, which indicates that 50-μm- to 200-μm-sized particles of the un-milled HDDR powder are textured. The texture value (I_{006}/I_{105}) increases with increase in milling time to a peak value of 48.3 after 4 h of milling and decreases with further milling. The initial increase in texture is due to the breaking of big particles into small ones and separation of single-grain particles. As shown in figures 3.8 (*c*) and 3.10 (a), almost all the particles obtained after 4 h of milling are isolated single-crystalline particles and can easily be aligned in a magnetic field, which results in maximum texture value. The decrease in XRD texture with further milling is a result of polycrystallization, partial amorphization of particles and flakes and an increase in the fraction of nanoparticles in the sample.

3.2 Magnetic characteristics

The effect of reducing the size of materials is of great importance from both fundamental considerations and modern practice. Nanometer-sized magnetic particles exhibit a variety of unique magnetic properties that are drastically different from those of their bulk counterparts [*Cul72, Sch90a*]. Differences in properties have been attributed to size and surface/interface effects. In the case of nanometer-sized particles the surface/volume atom ratio is large (*e.g.* 50 % and 20 % surface atoms for 3 and 10 nm particles, respectively) and broken symmetry at the surface/interface causes changes of band structure, atomic coordination number and lattice constant [*Kel05*]. These changes affect the characteristics of the nanoscale magnetic materials. Coercivity, one of the important extrinsic parameters of permanent magnets, has a striking dependence on the particle size. As the particle size is reduced, there is a critical size corresponding to a transition from multi-domain to single-domain state. The coercivity reaches a maximum just below the single-domain particle size and then decreases with further reduction in particle size, the particles become superparamagnetic below a certain size [*Her90*, *Row76, Ram88*]. Coercivity is also controlled by impurities, defects, and voids etc., which act as nucleation and/or pinning sites [*Zha01, Cam06*]. In this chapter, the change in magnetic properties of $SmCo_5$ and $Nd_2Fe_{14}B$ with respect to size and microstructure will be discussed.

3.2.1 Demagnetization behavior

3.2.1.1 $SmCo_5$ flakes

Demagnetization curves of starting powder and SA – ball-milled $SmCo_5$ powders are shown in figure 3.13. It is evident that the starting un-milled (0 h) powder has a low coercivity of 0.45 T. SA – ball milling with 10 wt.% OA and 60 wt.% n-heptane at 800 rpm results in fast increase of coercivity up to a maximum value of 2.3 T for 1 h of ball milling; further ball milling causes a decrease in coercivity. The coercivity behavior of $SmCo_5$ flakes is similar to the results obtained by Cui *et al.*, with a maximum coercivity value of 1.77 T [*Cui11*]. The fast increase in coercivity is expected to be due to the decrease in grain size and increase in shape anisotropy, the subsequent decrease of coercivity with further milling can be attributed to the partial amorphization and formation of very fine crystallites. As discussed in section 3.1.1 and shown in figure 3.4, the $SmCo_5$ flakes transform to textured polycrystalline flakes and form nanometer size crystallites after prolonged ball milling. The reduction in coercivity of these polycrystalline flakes is possible due to exchange-coupling between the nanometer-sized crystallites [*Her90, Alb78*]. Initial magnetization curves also change after SA – ball milling. As can be seen in figure 3.13, the starting powder shows a steep increase in magnetization at low applied fields. The initial magnetization curves become relatively flat after short SA – ball milling of 0.5 and 1 h. Successive SA – ball milling results in relatively steeper initial magnetization curves, representing an increase in the magnetic susceptibility with increasing ball milling time.

All the SA – ball-milled $SmCo_5$ samples show a kink in the demagnetization curves; the depth of the kinks increases with increasing milling time. A kink in the demagnetization curves often originates from the presence of a soft magnetic surface phase or the presence of soft magnetic phase in the volume along with the hard magnetic phase and also due to the difference in particle size [*Ram88, Zha07*]. As it has been shown in the SEM and TEM images that particles obtained after SA – ball milling have a significant size distribution ranging from flakes of size 2 *µ*m to nanoparticles of size 15 nm. The small flakes and

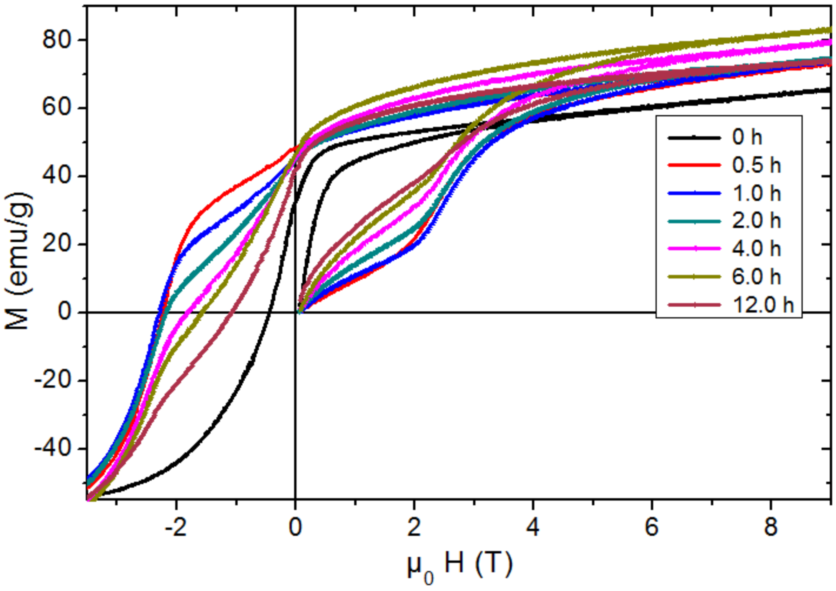

Figure 3.13 Demagnetization curves of $SmCo_5$ samples obtained after SA – ball milling with 10 wt.% OA and 60 wt.% n-heptane at 800 rpm for different milling times.

nanoparticles were separated using size-selection process prior to magnetic measurement but a complete separation is not possible due to residual magnetostatic attraction between the particles. The small flakes and nanoparticles have a relatively low anisotropic field which results in magnetization reversal at low fields. The fraction of small flakes and nanoparticles having relatively low anisotropy field increases with increasing milling time and thus the depth of kinks gets more pronounced. The presence of a kink is also possible due to an increase of free cobalt content in the particles and flakes. The flakes and particles obtained after high-energy ball milling can get partially oxidized on the surface, leaving free excess cobalt. Free cobalt or Sm-oxides were not observed in the X-ray diffraction measurements however, their amount could be below the detection limit (< 5 wt.%) for XRD. It is expected that the amount of surfactants remained in the samples after washing increases with increasing milling time due to reduction in the flake size and, therefore, the magnetization at 9 T should decrease with milling. In contrast to this, the magnetization at 9 T increases with milling up to 6 h which is possibly due to an increase of the cobalt content. The magnetization at 9 T decreases for the 12 h ball-milled sample which can be due to significant amorphization of the flakes.

3.2.1.2 $Nd_2Fe_{14}B$ particles and flakes

The demagnetization curves of SA – ball-milled $Nd_2Fe_{14}B$ powders are shown in figure 3.14. The starting powder (50-200 μm) has a coercivity of 1.4 T. The coercivity dropped very rapidly to 0.44 T after 0.5 h of milling and decreases continuously with successive ball milling. As reported by other groups [*Sim11, Cha07b, Pou11*], the coercivity of nanometer-sized particles obtained after SA – ball milling of $Nd_2Fe_{14}B$ is less (typically below 0.5 T) as compared to bulk sintered magnets. Cui *et al.* [*Cui12a*] observed a first increase in coercivity to a peak value of 0.35 T after milling for 5 h and then a decrease with further milling. The initial increase can be an effect of grain refinement while the decrease may be due to exchange-coupling between fine nanocrystalline grains [*Her90, Alb78*]. In another study by Simeonidis *et al.* [*Sim11*], elongated $Nd_2Fe_{14}B$ nanoparticles of size around 15 nm showed a maximum coercivity of 0.44 T. In the present study, the coercivity drops from 1.4 T to 0.44 T just after 0.5 h of milling and then decreases continuously to a value of 0.11 T after 14 h of milling. It is known that ball milling produces a lot of defects and stress on the particle surfaces [*Sur04*]. In the early stage of milling (0.5 h), the particle size decreases rapidly from around 200 μm to 2 μm. Due to this morphological change the particles become rough and a lot of defects are introduced at the surfaces. The roughness

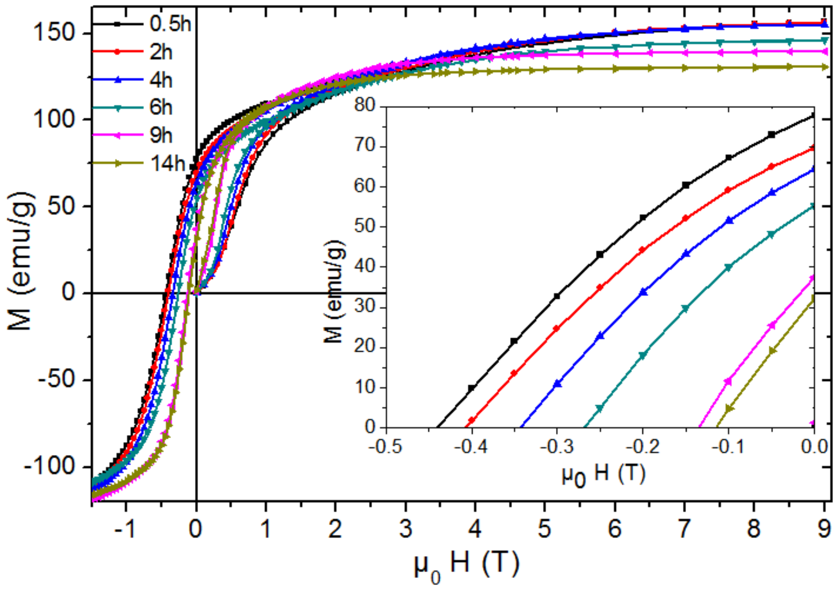

Figure 3.14 Demagnetization curves of $Nd_2Fe_{14}B$ samples obtained after SA – ball milling with 50 wt.% OA and 60 wt.% n-heptane at 400 rpm for different milling times.

and defect sites work as low anisotropic regions and can form reverse magnetization sites which results in the sharp drop in coercivity due to a reverse domain nucleation effect. The decrease in coercivity with further milling from 0.5 to 6 h can be due to an increased surface damage. A slight decrease in coercivity for 9- and 14-h-milled samples is possibly due to exchange-coupling between nanocrystalline grains of polycrystalline flakes [*Her90, Alb78*].

In an ideal case the coercivity should increase for single-domain particles but till now this has not been observed for hard magnetic $Nd_2Fe_{14}B$ particles. The coercivity of bulk sintered $Nd_2Fe_{14}B$ magnets is governed by nucleation of reverse domains [*Liv81, Ram88*] but for nanocrystalline materials or single-domain $Nd_2Fe_{14}B$ particles, the coercivity mechanism, in general, is not fully understood. As shown in figure 3.14, the initial magnetization curves of ball-milled samples are relatively steeper and the steepness increases with ball milling time, which indicates that it is easier to magnetize the smaller particles and that the magnetic susceptibility of longer ball-milled particles is increased. Magnetization at 9 T remains nearly constant at 156 emu/g for samples milled for 0.5 h and 4 h but decreases with further milling. The decrease in magnetization can be due to partial surface oxidation of the flakes. The magnetization at low fields increases rapidly for 9 h and 14 h ball-milled samples which can be possible due to an increased amount of soft magnetic α-Fe left after partial oxidation of Nd. There is no visible kink or shoulder in the demagnetization curves of ball-milled $Nd_2Fe_{14}B$ samples, whereas a significant kink was observed in the case of ball-milled $SmCo_5$ samples (figure 3.13). The kink in case of $SmCo_5$

samples is supposed to be due to the presence of some free cobalt and/or an increased fraction of low coercive nanoparticles, although the cobalt peaks were not observed in the XRD patterns which could be below the detection limit (< 5 wt.%) for XRD. It is possible to have nanoparticles or nanoflakes in the ball-milled $Nd_2Fe_{14}B$ samples but they can have nearly the same coercive field and hence the amount of kinks is insignificant.

3.2.2 Degree of texture

Particles and flakes of $SmCo_5$ and $Nd_2Fe_{14}B$ obtained after SA – ball milling were oriented in the presence of a magnetic field (2 T) and the texture of oriented samples was studied by magnetic measurements. Local texture of individual particles and flakes of $SmCo_5$ and $Nd_2Fe_{14}B$ were studied by HRTEM and electron diffraction and are discussed in sections 3.1.1 and 3.1.2, respectively. The collective (global) texture properties based on the degree of orientation were studied by magnetic measurements and a comparison of results by XRD analysis is presented and discussed in this section.

3.2.2.1 $SmCo_5$ flakes

Figure 3.15 (a) shows the demagnetization curve of a magnetically-oriented $SmCo_5$ sample measured in parallel (//) direction to the orienting magnetic field. In the case of randomly-oriented samples shown in figure 3.13, the coercivity first increases to a peak value and then decreases with further increasing milling time. In contrast to the randomly-oriented samples, the coercivity for textured samples remains nearly constant for 1-6 h of milling. The magnetization at 9 T is not the same for the samples milled for 1-6 h. The lower value of remanence and magnetization at 9 T for longer time milled samples is attributed to the increased amount of surfactants in the samples due to coating on individual smaller particles with increased surface area, and increase of the fraction of smaller flakes and nanoparticles which could not orient in the magnetic field. Figures 3.15 (b)-(d) show the demagnetization curves of 0.5-, 4- and 12-h-milled $SmCo_5$ samples measured in directions parallel (//) and perpendicular (⊥) to the orienting magnetic field. The // and ⊥ direction curves for all the samples show anisotropic behavior and both the curves come closer with increase in milling time, which indicates that the anisotropy of the samples reduces with increase in milling time. The degree of texture (DOT) of the magnetically-oriented samples was calculated using following formula.

$$\mathrm{DOT}\ (\%) = \frac{M_r(//) - M_r(\perp)}{M_r(//)} \times 100 \qquad (3.1)$$

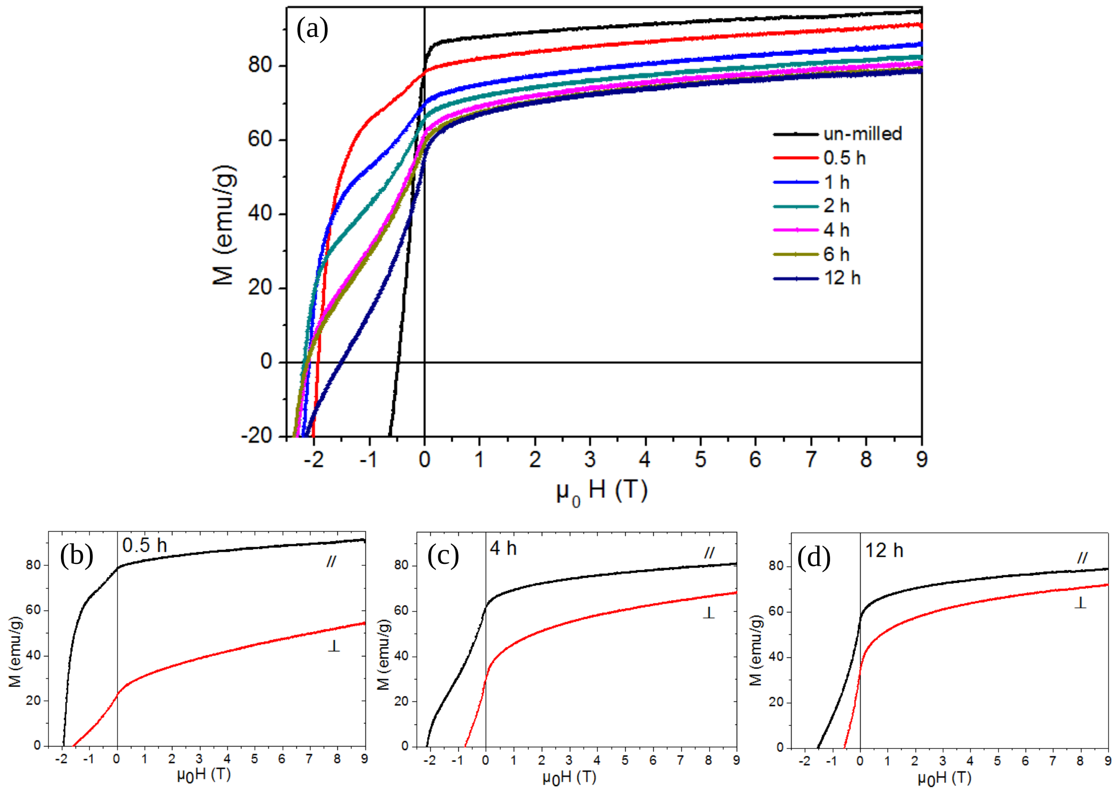

Figure 3.15 (a) Demagnetization curves of magnetically oriented $SmCo_5$ samples measured in the parallel (//) direction of the orienting magnetic field. Demagnetization curves measured in parallel (//) and perpendicular (⊥) directions of samples obtained after SA - ball milling at 800 rpm in 10 wt.% oleic acid + 60 wt.% n-heptane for milling times of (b) 0.5 h, (c) 4h and (d) 12 h.

where, M_r (//) and M_r (⊥) are the remanent magnetization values in parallel and perpendicular directions to the orienting magnetic field, respectively.

A DOT value of 0 % corresponds to isotropic samples, whereas, a DOT value of 100 % represents fully anisotropic samples with the condition of zero remanence in perpendicular direction.

The variation of M_r (//), M_r (⊥) and DOT are shown in figure 3.16. It is evident from this figure that the M_r (//) value decreases, whereas the M_r (⊥) value increases with increase in milling time and the DOT value decreases accordingly. The size of starting powder particles (2-40 μm) is small and most of the particles are close to the single-domain size and so these particles can be very well oriented in magnetic field resulting in high M_r (//) and DOT values. The DOT value drops from 86.6 % for un-milled powder to 71.6 % after 0.5 h of ball milling and decreases continuously with further milling. Ball milling at lower milling speed reduces the milling energy and therefore the crushing is not so extensive. Under controlled SA – ball milling at 200 rpm, it was observed that the DOT reaches to a peak

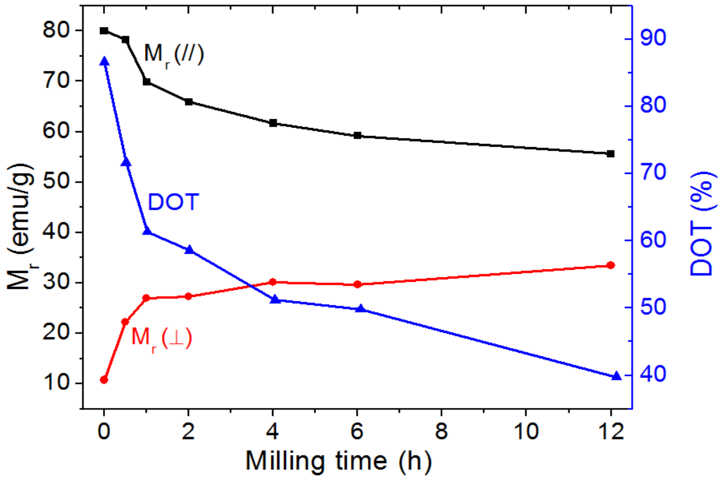

Figure 3.16 Variation of M_r (//), M_r (⊥) and DOT with ball milling time for magnetically-oriented $SmCo_5$ samples obtained after milling with 10 wt. % oleic acid + 60 wt.% n-heptane at 800 rpm.

value of 93 % after 10 h of milling and then decreases with further milling. The breaking up of large single-crystalline particles into single-micrometer-sized textured polycrystalline flakes results in a decrease of DOT. The applied magnetic field may not produce enough torque due to the small particle size and it is relatively hard to align the flakes against mechanical friction. A further decrease in DOT and M_r (//) with prolonged ball milling can be collectively due to an increased fraction of polycrystalline flakes and nanoparticles and nanoflakes (discussed earlier in section 3.1.1) in the samples which prohibits the alignment. As already discussed in section 3.1.1 and shown in figure 3.6, the XRD patterns of textured samples show strong (*00l*)-type peaks. Texture values were estimated by calculating the ratio (I_{002}/I_{111}) of integral intensities of (*002*) and (*111*) peaks. The texture values of 37, 9, 4, 2.3 and 0.9 were obtained for 1, 2, 4, 6 and 12 h ball-milled samples, respectively. The (*111*) peak is invisible in the XRD pattern for the 0.5-h-milled-oriented sample, indicating that the sample milled for 0.5 h is almost single-crystalline. The texture values obtained from the XRD measurements follow the same trend as the DOT obtained from the magnetic measurements of oriented samples.

3.2.2.2 $Nd_2Fe_{14}B$ particles and flakes

Figure 3.17 (a) shows demagnetization curves of magnetically-oriented un-milled and SA – ball-milled $Nd_2Fe_{14}B$ powders measured in the // direction with respect to the orienting magnetic field. The coercivities of magnetically-oriented samples are nearly the same as those of random samples but the remanence in // direction increases sharply from

119.5 emu/g for un-milled powder to 148.1 emu/g after 0.5 h of milling. The increase in remanence value indicates a strong texture in the ball-milled powders. Samples ball-milled between 0.5 and 2 h show almost the same remanence values. Further milling at 400 rpm results in a slight decrease in the remanence value. Intense milling at 800 rpm causes a sharp decrease in the remanence to a value of 92.2 and 77.8 emu/g for 9- and 14-h-milled samples, respectively. The initial increase in remanence value is attributed to breaking of locally textured 50-μm- to 200-μm-sized particles to single-micrometer-sized particles (figure 3.8 (a)). Due to the presence of local texture in the starting d-HDDR processed powder particles, as reported by Güth and Gutfleisch *et al.* [*Güt11, Gut03*]; the small particles containing a few (<10) grains can be highly textured and hence orient very well in a magnetic field resulting in a high remanence. The remanence value is slightly reduced in the case of isolated single-crystalline particles obtained after 4 h of milling as compared to single-micrometer and sub-micrometer-sized particles obtained after 2 h of milling. This decrease can be due to the increased amount of surfactants (which cannot be removed by washing)

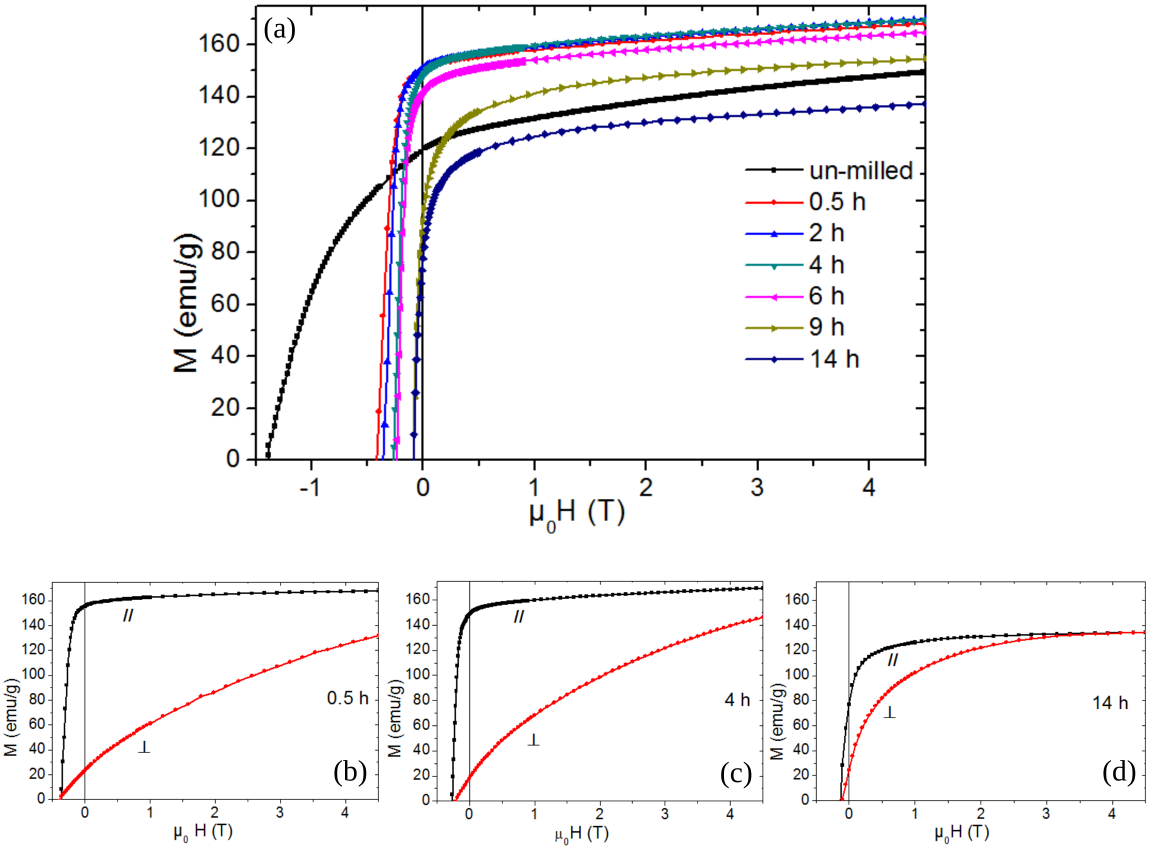

Figure 3.17 (a) Demagnetization curves of magnetically oriented $Nd_2Fe_{14}B$ samples measured in parallel (//) direction, and parallel (//) and perpendicular (⊥) direction measured demagnetization curves for samples milled for (b) 0.5 h, (c) 4 h and (d) 12 h with 50 wt.% oleic acid + 60 wt.% n-heptane at 400 rpm.

present in the sample due to coating on the individual particles. Qualitatively, the amount of surfactants present in the samples increases with decrease in particle size because of the increase in the surface area of the particles. The increased degree of polycrystallization, surface damage, surface oxidation and fraction of small nanoparticles with successive milling (discussed in section 3.1.1) can also be the possible reasons for a decrease in the remanence value. The effect of these parameters can be seen in terms of a sharp decrease in remanence for 9- and 14-h-milled samples. Figures 3.15 (b)-(c) show demagnetization curves measured in (//) direction. Although the remanence value is a little lower when measured in // and ⊥ direction of the orienting magnetic field for samples milled for 0.5, 4 and 14 h. The M_r (//) for 0.5- and 4-h-milled samples is nearly the same, whereas the M_r (⊥) value for the 4-h-milled sample is significantly smaller than that of the 0.5-h-milled sample. This indicates that the 4-h-milled samples are better textured as compared to the 0.5-h-milled sample, which agrees with the SEM and TEM results in figure 3.7 (c) and figure 3.10 (a), showing the single-crystalline nature of particles obtained after 4 h of milling. The M_r (//) value has decreased significantly for the 14 h ball-milled sample and the gap between M_r (//) and M_r (⊥) is very small showing a reduced texture of the sample. As shown in figure 3.18, the DOT, calculated from the M_r (//) and M_r (⊥) values, first increases with increase in milling time or decrease in particle size to a peak value of 87.95% and then decreases with further milling. The initial increase is due to an improved alignment of highly-textured and single-crystalline particles. Almost all the particles can be oriented with the easy axis in the magnetic field direction in the case of 4 h of milling and this results in a maximum DOT. The DOT decreases with further milling because of an increase in the degree of

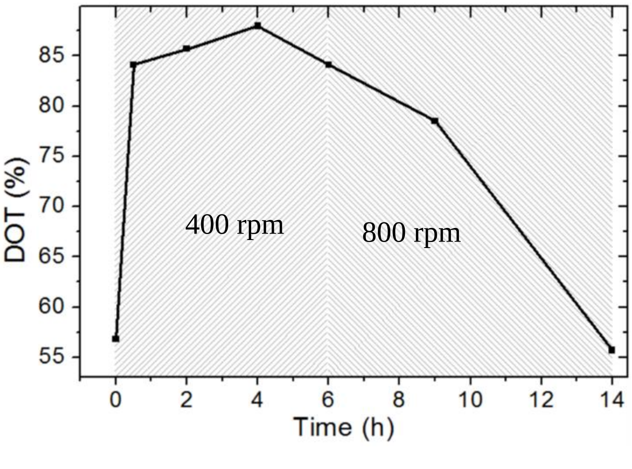

Figure 3.18 Variation of DOT with ball milling time for magnetically oriented $Nd_2Fe_{14}B$ particles (textured samples), prepared by SA – ball milling with 50 wt. % oleic acid + 60 wt.% n-heptane at 400 rpm.

polycrystallinity and the fraction of nanoparticles which cannot be easily aligned in magnetic field and decreases texture. The nanoparticles experience much less torque (as compared to mechanical friction that hinders the alignment) in applied magnetic field due to their small size and thus the alignment is difficult. The texture values calculated by the ratio (I_{006}/I_{105}) of integrated intensities of (*006*) and (*105*) XRD peaks of magnetically-oriented samples (figure 3.12 (b)) show the same trend as the DOT values obtained from the magnetic measurements.

3.2.3 Spin reorientation in $Nd_2Fe_{14}B$: influence of intergrain exchange-coupling

Spin reorientation is a temperature-induced magnetic phase transition characterized by the spin reorientation temperature which is the temperature where the magnetization deviates from the easy-axis. In $Nd_2Fe_{14}B$, the spin reorientation is caused by a temperature-induced competition between the contributions from different terms of the crystalline electric field acting on the Nd^{3+} ions to the net anisotropy. The spin reorientation temperature T_{SR} of $Nd_2Fe_{14}B$ has been determined to be 135 K for single-crystal and for a polycrystal, as well as sintered magnets in which the grain sizes of $Nd_2Fe_{14}B$ are within a few micrometers [*Giv84, Grö86, Grö90*]. The [*00l*] direction of the tetragonal structure is the easy-axis of $Nd_2Fe_{14}B$ from 135 up to 585 K, the latter being the Curie temperature. Below 135 K, the easy-axis tilts away from the [*00l*] direction. The tilting angle increases with lowering the temperature and reaches about 30° at 4.2 K [*Giv84, Hir86*].

The direct way to characterize the spin reorientation is to measure the temperature dependent magnetocrystalline anisotropy constants, which usually requires a very good alignment of particles. It was difficult to align all the particles in the ball-milled samples. Therefore the spin reorientation temperature was determined only by an indirect method after measuring the temperature dependence of ac-susceptibility of different samples. The ac-susceptibility was measured using PPMS in the temperature range from 10 to 300 K at an ac-frequency of 333 Hz and a magnetic field amplitude of 10 Oe. By using this device, the absolute values of the real-component (χ') and the imaginary-component (χ'') of the ac-susceptibility can be determined simultaneously.

Figures 3.19 (a) and (b) show the temperature dependence of the ac-susceptibility on the randomly oriented starting HDDR powder (un-milled) and 1, 4, 9 and 14 h SA – ball-milled $Nd_2Fe_{14}B$ powder samples. The spin reorientation temperature (T_{SR}) was determined to be the temperature where $d\chi'/dT$ reaches a minimum. The plot for $d\chi'/dT$ with

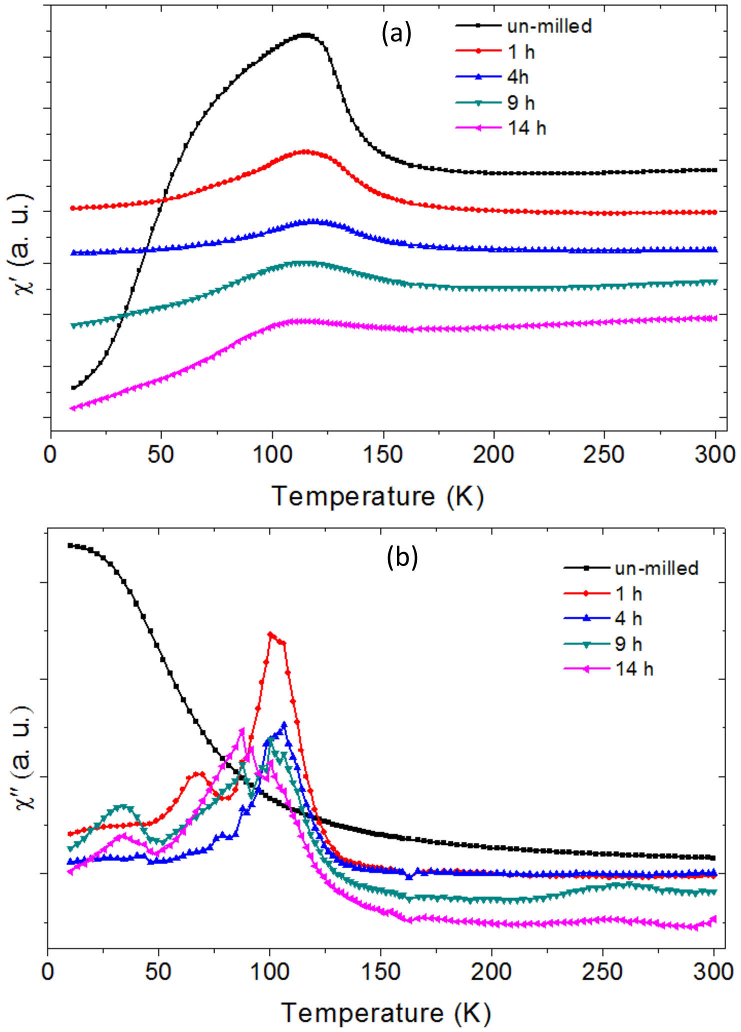

Figure 3.19 Temperature dependence of (a) real-component (χ`) and (b) imaginary-component (χ``) of ac-susceptibility measured on randomly oriented $Nd_2Fe_{14}B$ powder particles obtained after SA – ball milling with 50 wt.% oleic acid + 60 wt.% n-heptane at 400 rpm. The measurement was performed in a magnetic field of 10 Oe.

temperature is shown in figure 3.20 (a) and the variation of T_{SR} with ball milling time is shown in figure 3.20 (b). A spin reorientation temperature of 129 K was obtained for d-HDDR-$Nd_2Fe_{14}B$ powder which is lower than that for single-crystalline or sintered $Nd_2Fe_{14}B$ magnets. The T_{SR} value was increased to 133.8 K for smaller particles (1-2 μm, consisting of < 10 grains) obtained after 1 h of milling. The single-crystalline particles of size 200-500 nm, obtained after 4 h of SA – ball milling, show a T_{SR} value of 136.5 K. The T_{SR} value was slightly increased to 137 K with further SA – ball milling for 9 h. The single-crystalline particles transformed to polycrystalline flakes after 14 h of SA – ball milling and the T_{SR} value decreased drastically to 128.5 K. In the case of single-crystalline and sintered $Nd_2Fe_{14}B$ magnets, in their demagnetized state, the grains are large enough to contain multi-

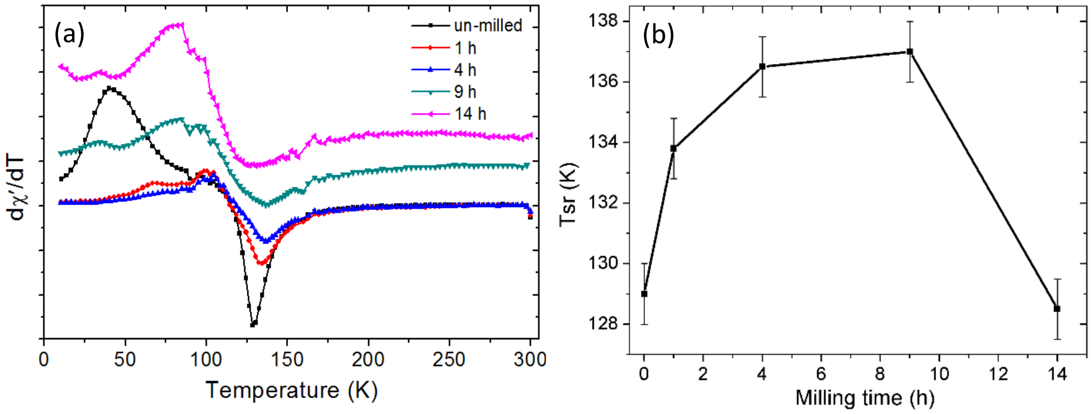

Figure 3.20 (a) Temperature dependence of dχ'/dT, the minima correspond to the spin reorientation temperature (T_{SR}), (b) variation of T_{SR} with milling time for randomly-oriented $Nd_2Fe_{14}B$ powder particles obtained after SA – ball milling with 50 wt.% oleic acid + 60 wt.% n-heptane at 400 rpm.

domains. In this case, the intergrain magnetic exchange-coupling does not exist and therefore has no influence on the spin reorientation temperature [*Kou87*]. In the d-HDDR treated material, the $Nd_2Fe_{14}B$ grains are of mainly single-domain size. The magnetic exchange-coupling among these grains influences the moment arrangement and in turn the spin reorientation temperature [*Kou87*]. Thus the spin reorientation temperature for starting HDDR-$Nd_2Fe_{14}B$ powders is slightly lower (129 K) than that of bulk single-crystalline or sintered magnets (135 K). The spin reorientation temperature was increased to 133.8 K for smaller particles which consist of only a few (< 10) grains. The contribution of magnetic exchange-coupling is reduced for smaller particles with a smaller number of grains (< 10) and therefore the T_{SR} value approaches that of single-crystalline particles. In case of isolated single-crystalline particles of size 200-500 nm obtained after 4 h of SA – ball milling, where the particles are nearly single-domain and a magnetic exchange-coupling can be fully excluded. The spin reorientation temperature increases to 136.8 K which is close to the T_{SR} value of bulk micrometer-sized single-crystalline particles. A further increase of T_{SR} to 137 K was observed for the samples milled for 9 h. As mentioned in section 3.1.2 and shown in figure 3.8 (e), almost all the particles transformed to flakes with average diameter 500 nm and average thickness of 100 nm after 9 h of SA – ball milling. A similarly increased T_{SR} value of 137 K has been reported by Akdogan *et al.* [*Akd10*] for $Nd_2Fe_{14}B$ flakes. The slight increase of T_{SR} as compared to single-crystal particles (135 K) can be due to a size effect and also due to induced strain and defects at the surfaces. However, a decrease of the T_{SR} value with decrease in particle size (< 300 nm) was reported by Rong *et al.* [*Ron10c*] who also ruled out that the size effect is not the major cause for the decrease in T_{SR} value. The induced strains and defects due to intensive ball milling seem to be strong factors influencing the anisotropy constants and hence the spin reorientation temperature.

The spin reorientation temperature decreases drastically to 128.5 K for the flake sample obtained after 14 h of SA – ball milling. These flakes were polycrystalline in nature with average crystallite size of 12 nm. The polycrystalline flakes are textured and the nanometer-sized grains are supposed to be magnetically exchange-coupled to the neighboring grains. The intergrain exchange-coupling can be large enough to influence the magnetic easy-axis of the nanocrystalline grains, and so the easy-axis is now determined not only by the magnetocrystalline anisotropy but also by the intergrain magnetic exchange-coupling. According to the calculations based on a phenomenological model [*Zha98*], the anisotropy constant K_1 is changed due to the presence of the strong intergrain magnetic exchange-coupling. In the case of $Nd_2Fe_{14}B$, the spin reorientation temperature corresponds to the temperature where $K_1 = 0$. According to the calculations, in case of nanocrystalline $Nd_2Fe_{14}B$ the temperature corresponding to $K_1 = 0$ is shifted to a lower value when the intergrain magnetic exchange-coupling is taken into account [*Zha98*]. Here the experimental observations in case of nanocrystalline flakes confirm the strong dependence of the spin reorientation temperature on the magnetic exchange-coupling. In general, the spin reorientation temperature can also differ due to change in composition. In this study the samples were prepared by SA – ball milling. The particle size was reduced through fragmentation of the particles along the grain boundaries, a successive fragmentation due to milling resulted in the formation of the isolated single-crystalline particles (see section 3.1.1). In this process of particles size decrease, a change in the composition of particles is not expected. The initial composition of magnet was $Nd_{28.78}Fe_{bal}B_{1.1}Ga_{0.35}Nb_{0.26}$ (in wt.%) which forms stoichiometric $Nd_2Fe_{14}B$ grains after the HDDR process and the rest of the elements are expected to be present in the grain boundaries. Furthermore the $Nd_2Fe_{14}B$ is a line compound which means no stoichiometric variations are possible and a change in the composition would result in formation of extra phases which was not observed in the XRD patterns of the SA – ball-milled samples (shown in figure 3.12 (a)). So the change in spin reorientation temperature due to compositional change can be excluded in this study.

Chapter 4

Influence of milling parameters

Ball milling is a complex process involving optimization of a number of process variables to achieve the desired properties of the product. The important variables that have a significant effect on the final constitution of the milled powder are as follows: type of mill, milling container, milling energy/speed, milling time, powder-to-ball weight ratio, milling atmosphere and temperature during milling. However, some of these process variables are not completely independent [*Sur01*].

The influence of milling media (*e.g.* solution type, polarity, surfactant amount) and milling energy (in terms of rotational speed) on the structural, morphological and magnetic properties of $SmCo_5$ and $Nd_2Fe_{14}B$ particles and flakes have been investigated. The other influential parameters were maintained constant during the investigation of milling media and milling energy.

4.1 Influence of milling media

In general, ball milling is employed for grinding and mechanical alloying. Ball milling in a protective argon gas atmosphere (dry ball milling) proceeds by successive crushing and re-welding of the particles, leading to a homogeneous powder. A presence of solution (surfactant and/or solvent) during the milling alters the milling energy and milling efficiency and reduces or prevents the coalescencing or re-welding. As a result the morphology is significantly changed from tens of micrometer-sized re-welded irregular particles resulting in the case of dry ball milling to nanometer-sized isolated anisotropic particles resulting in the case of SA – ball milling.

4.1.1 Dry and wet ball milling

Dry and wet ball milling of d-HDDR processed $Nd_2Fe_{14}B$ particles (starting sample morphology is shown in figure 3.7) have been performed to investigate the effects of different solution types on the characteristics of milled powders. The dry ball milling was carried out in a protective argon gas atmosphere, whereas the wet ball milling was performed in the presence of different liquids (n-heptane, acetone, ethanol). In the case of

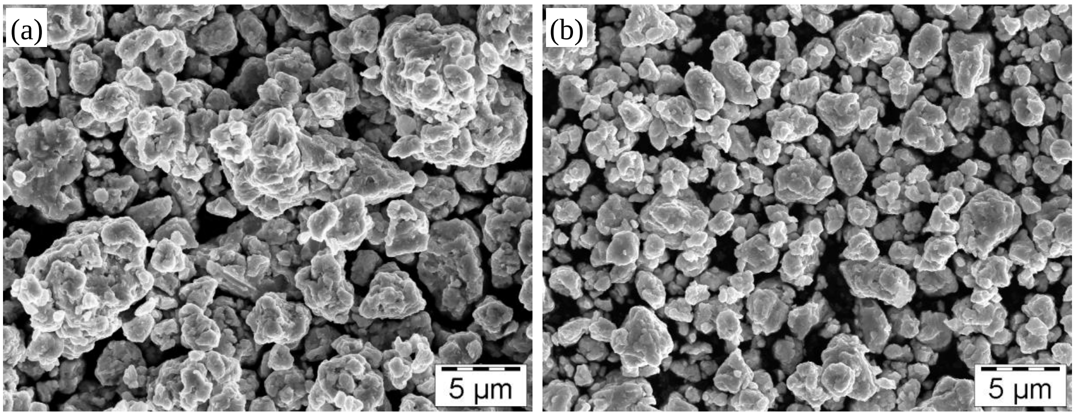

Figure 4.1 Secondary electron SEM images of $Nd_2Fe_{14}B$ particles obtained after (a) dry ball milling and (b) wet ball milling in 100 wt.% n-heptane.

dry milling, it was observed that the hundreds of micrometer-sized particles consisting of 200-500 nm grains break down to tens of micrometer-sized particles just after 0.25 h of milling. Some single-crystalline particles were also present in the samples at this stage. Continued ball milling resulted in crushing of larger particles but the smaller single-crystalline particles coalesced due to re-welding and formed micrometer-sized particles. The range of particle size became narrower with increasing milling time; nevertheless the particles were re-welded and agglomerated. As can be seen in figure 4.1 (a) particles of size ranging from 2 to 10 μm were obtained after 4 h of dry milling. The particle morphology remained almost the same after wet ball milling in presence of n-heptane as that of dry milling, except achievement of a relatively lower particle size distribution (figure 4.1 (b)). It is known that the presence of n-heptane during ball milling reduces the milling energy and also the friction but it is not able to prevent re-welding between the particles [*Kot11*, *Yek01*].

4.1.2 Polarity and molecular chain length of the solution media

The polarity and molecular chain length of the solvent are very important factors influencing the milling process. A non-polar solvent (n-heptane) can wet the surface of particles but doesn't attach to the surfaces through chemical bonding. In contrast, acetone, ethanol and oleic acid are polar solvents with ketone, alcohol and carboxyl functional groups, respectively. The molecular structures of the surfactant and the solvents are shown in figure 4.2. These molecules can attach to the particle surface through chemical bonding with oxygen in their functional groups [*Yan07, Kok11*]. Polar solutions provide a coating layer over the particles which reduces friction and prevents re-welding of the particles during ball milling. It is evident from figures 4.3 (a)-(c) that isolated sub-micrometer-sized

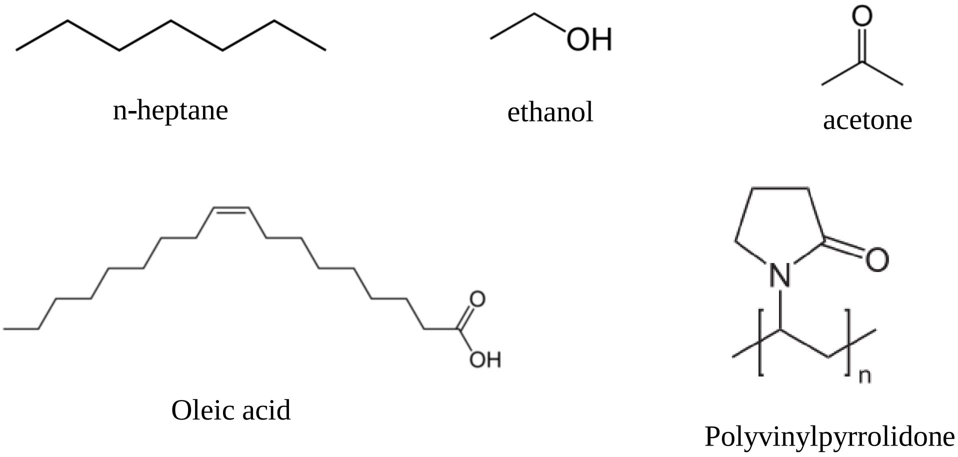

Figure 4.2 Molecular structures of surfactants and solvents used in this study.

particles can be obtained after milling in polar solvents: acetone, ethanol and oleic acid + n-heptane. The particles fracture very rapidly with milling in n-heptane; a significant number of particles consisting of single grain or a few (< 5) grains were obtained after only 0.25 h of milling. Longer time milling causes re-welding and produces micrometer-sized particles (figure 4.1 (a)). In case of wet ball milling with acetone and ethanol, the decrease of particle size with milling time is relatively slow. Longer time ball milling results in fragmentation of large particles down to individual grains or to particles consisting of 2 or 3 grains. It was found that the presence of acetone or ethanol was able to prevent re-welding but the surfaces of particles were damaged and became rough after prolonged ball milling. It was also observed that surface damage and roughness was more pronounced in the case of acetone milling than that of milling in ethanol. The use of surfactants (oleic acid) during milling was very helpful to prevent surface damage; isolated single-crystalline particles with clear edges (shown in figure 4.3 (c)) were obtained by milling in the presence of oleic acid. The polarity of oleic acid is much less compared to that of ethanol and acetone but the molecular chain

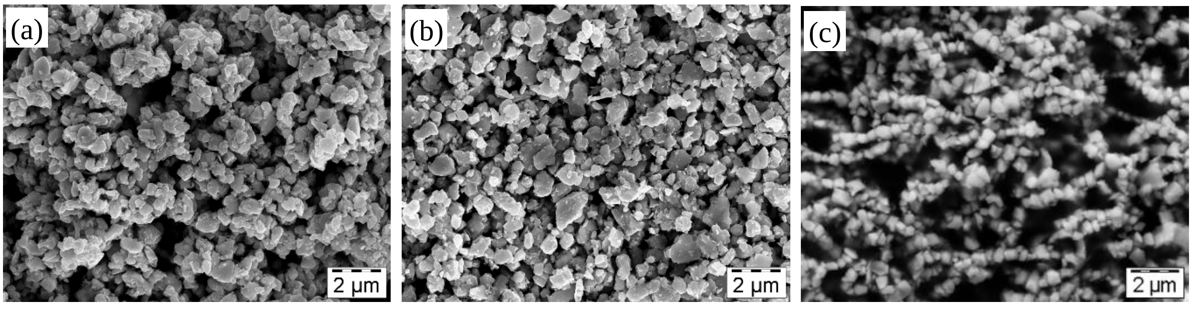

Figure 4.3 Secondary electron SEM images of $Nd_2Fe_{14}B$ particles obtained after ball milling in (a) 100 wt.% acetone, (b) 100 wt.% ethanol and (c) 50 wt.% oleic acid + 60 wt.% n-heptane at 400 rpm.

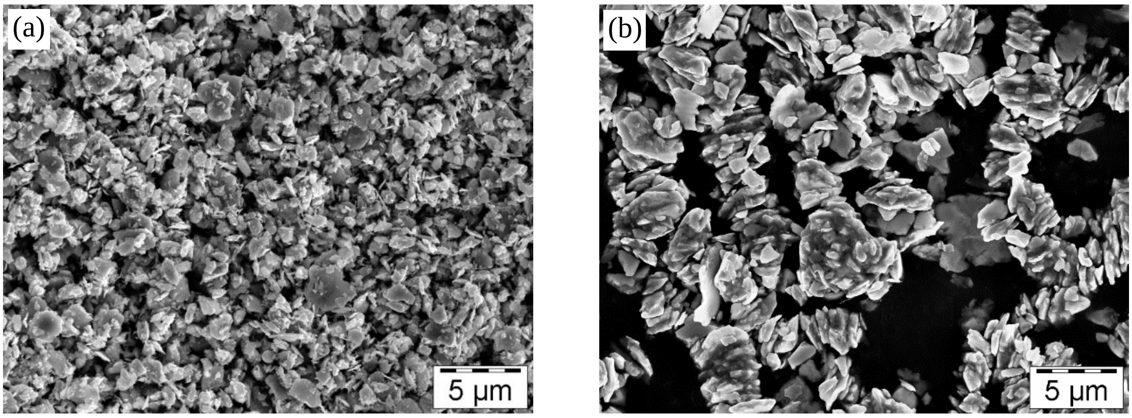

Figure 4.4 Secondary electron SEM images of $SmCo_5$ particles obtained after ball milling in (a) 100 wt.% ethanol and (b) 10 wt.% oleic acid + 60 wt.% n-heptane at 400 rpm.

length is much larger [*Lid09*]. The long molecular chain length is expected to play a critical role in reducing the friction and preventing the surface damage during ball milling [*Sur04*]. The particles were more uniform in size and almost all particles were single-crystalline when ball-milled in oleic acid + heptane (figure 4.3 (c)). However, Crouse *et al.* observed only a small effect of the molecular weight (chain length) of surfactants on the morphology of $SmCo_5$ ball-milled samples [*Cro12*].

Figures 4.4 (a) and (b) show the morphology of $SmCo_5$ powder samples obtained after milling in ethanol and oleic acid + n-heptane. It is evident from the images that milling in ethanol and oleic acid leads to the production of flakes (of average diameter 2 μm), whereas n-heptane milled powder showed re-welded particles of diameter 2-20 μm. The flake size and thickness of the ethanol-milled sample was smaller than that of the flakes obtained by milling in oleic acid. In addition, the relative fraction of small particles (< 500 nm) was increased in case of ethanol compared to that of oleic acid + n-heptane milled powders. It indicates that even with a strong polar nature, ethanol is not as effective as oleic acid to protect the particle surfaces. The longer molecular chain and the presence of two oxygen atoms in the functional group of oleic acid during milling are expected to play an important role in protecting the particle's surfaces and in turn reduce friction and to some extent milling energy.

The effect of molecular weight (chain length) on the flake morphology was investigated by using two different surfactants; polyvenylpyrrolidone (PVP) and oleic acid. PVP is a polymer compound having molecular weight from 2500 g/mol to about 1 million g/mol which is obtained mainly by free-radical polymerization of N-vinylpyrrolidone in water or alcohols with a suitable initiator [*Haa85*]. The average molecular weight of PVP

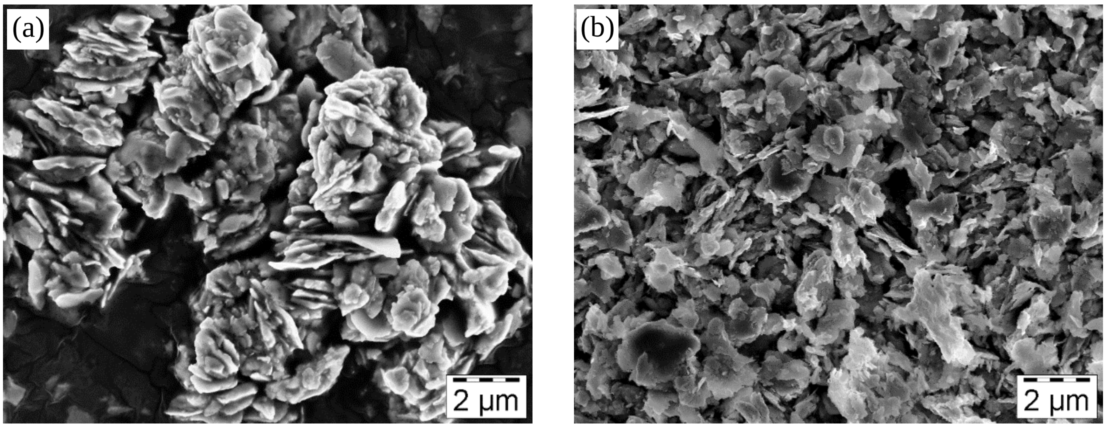

Figure 4.5 Secondary electron SEM images of $SmCo_5$ particles obtained after ball milling at 800 rpm for 7 h in (a) polyvenylepyrrolidone + ethanol and (b) oleic acid + n-heptane.

used was 40 kg/mol, which indicates that the PVP molecules are significantly larger than those of oleic acid that has a molecular weight of 282.46 g/mol. The morphologies of samples ball-milled with PVP and oleic acid are shown in figures 4.5 (a) and (b). The $SmCo_5$ particles transformed to flakes in both cases and the average diameter and thickness was decreased with increase in milling time. It was found that the average diameter and thickness of the flakes obtained after ball milling in oleic acid was smaller than those in the case of PVP and the fraction of nanometer-sized flakes and particles was observed to be higher for the samples milled in oleic acid. For example, flakes of average diameter and thickness of 1.8 μm and 200 nm, respectively, were obtained for PVP-milled samples, whereas the average diameter and thickness of flakes milled in oleic acid was reduced to 1.2 μm and 100 nm, respectively (figure 4.5). This difference in flake size and thickness is assumed to be due to the difference in the molecular chain length of the surfactants. The longer-chained molecules can form a thicker coating layer on the particle surface and hence reduce the milling energy [*Sur04*]. As a result the size and thickness of the particles decrease slowly with milling time for PVP-milled samples than those of oleic-acid-milled samples.

4.1.3 Amount of surfactant

Appropriate amounts of surfactants should be present during the milling process to cover the initial particle surfaces and the newly fractured surfaces, in order to prevent re-welding. It has been observed by Zheng *et al.* [*Zhe11*] that as little as 2 wt.% of surfactants is sufficient to form flakes of $SmCo_5$ and to prevent re-welding effectively. The surface area of particles increases with decrease in particle size, so more surfactant is needed as the particle size decreases. Figures 4.6 (a)-(f) show the effect of the oleic acid amounts (5, 10 and 50 wt.%) on the morphology of $SmCo_5$ flakes obtained after 4 h of milling at 800 rpm. It is clear from the low and high magnification images that the average size of flakes is lower for smaller oleic acid amounts. At lower amount (5 wt.%) of surfactant, ball milling causes a rapid decrease in particle size and flakes were formed at even 0.5 h of milling. The flakes agglomerated into particles of diameter around 4 μm for 5 wt.% oleic acid, whereas well separated flakes were obtained for 10 and 50 wt.% oleic acid (figures 4.6 (a)-(f)). The fraction of nanometer-sized flakes and particles decreases whereas uniformity in flake size increases with increase in amount of surfactant. This is because the increased amount of surfactant provides a better capping over the particles and results in a decrease of impact

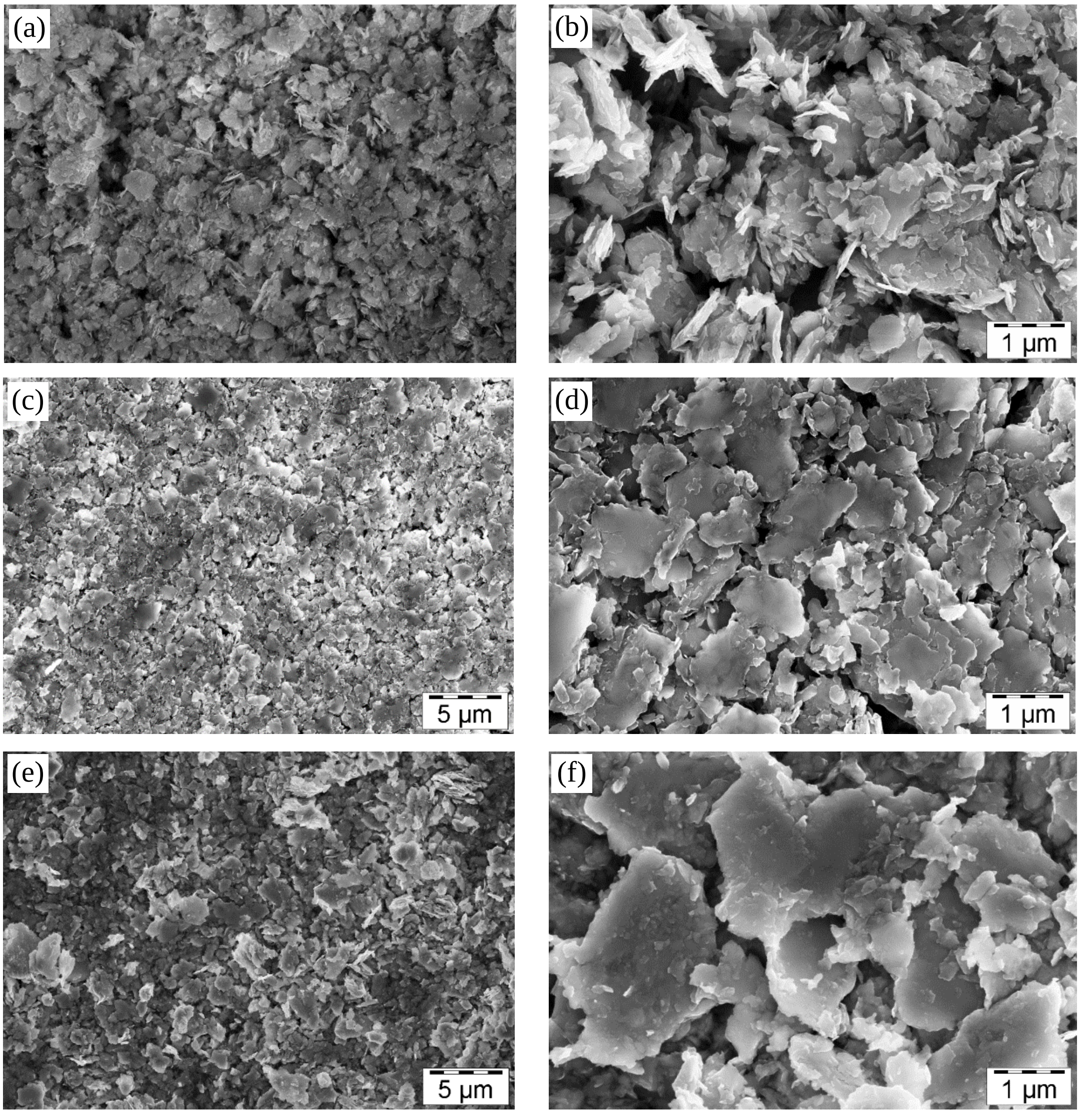

Figure 4.6 Secondary electron SEM images of $SmCo_5$ flakes obtained after 4 h of ball milling with (a) and (b) 5 wt.%, (c) and (d) 10 wt.%, (e) and (f) 50 wt.% oleic acid and 60 wt.% heptane. Left column showing low magnification and right column showing high magnification images.

between balls and powders which lowers the rate of decrease of flake size and thickness with milling time. By using a higher amount of surfactant, thinner flakes without agglomeration or re-welding can be obtained after prolonged milling. In this case the fraction of nanometer-size flakes and particles was increased as compared to that with lower amount of surfactant.

Figure 4.7 (a) shows the average grain size of the $SmCo_5$ powder estimated from Scherrer's formula after SA – ball milling at 800 rpm with 5, 10 and 50 wt.% of oleic acid for 1, 2, 4 and 6 h. It is clear from the graph that the average grain size decreases with increasing milling time. For a fixed milling time the average grain size decreases with decreasing amount of surfactant. This is due to the fact that an increased amount of surfactants provides better coating over the particles and reduces the milling efficiency. Crystallographic texture values were determined after calculating the ratio (I_{002}/I_{111}) of integrated intensities of (*002*) and (*111*) XRD peaks of magnetically-oriented samples. The value of I_{002}/I_{111} was 0.2 for non-aligned (isotropic) $SmCo_5$ powder. Figure 4.7 (b) shows that the texture value (I_{002}/I_{111}) decreases with increasing milling time and decreases with decreasing amount of surfactant. The high texture value for the 1-h-milled sample with 50 wt.% oleic acid is attributed to the mostly single-crystalline nature of the flakes. As shown in figure 4.6, the fraction of nanometer-sized particles and flakes is increased for lower amount of surfactants. Additionally, the flakes with lower amount of surfactant can transform easily into polycrystalline flakes because, as shown in figure 4.7 (a), the flakes with lower amount of surfactant possess a smaller grain size. The orientation of samples containing an increased fraction of polycrystalline flakes and nanometer size particles and flakes is relatively poor in magnetic field and therefore the texture value (I_{002}/I_{111}) decreases

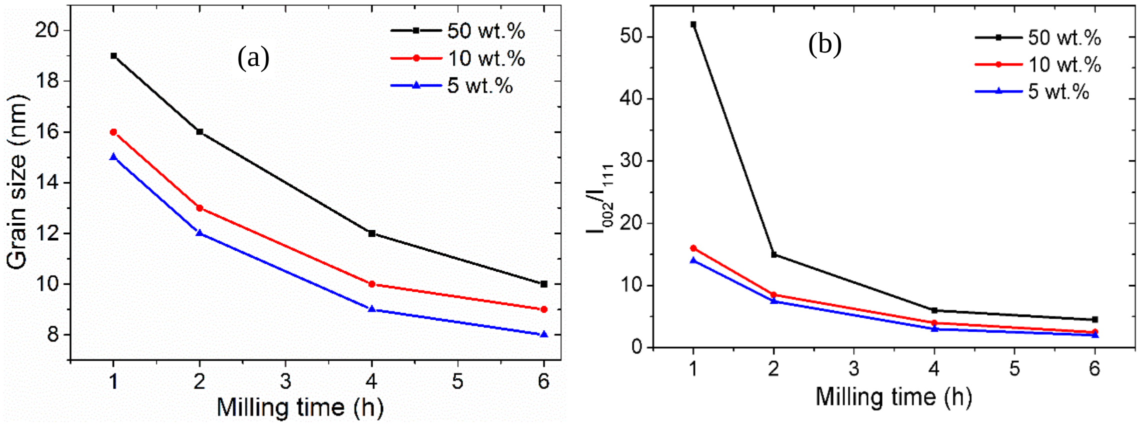

Figure 4.7 Effect of amount of surfactant on (a) grain size and (b) texture value of $SmCo_5$ flakes obtained after ball milling with 5, 10, 50 wt.% oleic acid and 60 wt.% heptane at 800 rpm. The grain size is represented as the coherently/scattered regions for the X-rays.

with decreasing surfactants amount. Another reason for the reduced texture value for lower amount of surfactant could be a partial re-welding of the flakes due to an insufficient amount of surfactants [*Zhe11*].

Figure 4.8 shows the effect of amount of surfactant on coercivity of samples milled with 5, 10 and 50 wt.% oleic acid at 800 rpm. The coercivity is nearly the same for 1-h-milled samples. A distinctive rate of change in coercivity was observed for different amounts after poonged milling. The coercivity drops rapidly from the peak value of 2.27 T for the 1-h-milled sample to 1.13 T for the 6-h-milled sample in case of 5 wt.% oleic acid, whereas in case of 50 wt.% oleic acid the coercivity reaches to the peak value of 2.27 T after 2 h of ball milling and then decreases to 2.05 T after 6 h of milling. The peak in coercivity values is expected to be due to the decreased particle size (discussed in section 3.1.1) which was found to be around 2 μm that is equivalent to the single-domain size for $SmCo_5$ [*Cam05*]. As mentioned earlier in this section, the particle size decrease becomes slower with increasing amount of surfactant. Due to the size effect, the peak values of coercivity shift to higher milling times with increasing the amount of surfactant. The drop in coercivity with further ball milling can be attributed to the partial amorphization and formation of very fine crystallites (discussed in section 3.1.1 and shown in figures 3.4 (b), (d) and (e)). The fine grains in polycrystalline flakes can be exchange-coupled to the neighboring grains which reduces the coercivity [*Giv84, Her90*]. The increased amount of surfactants provides

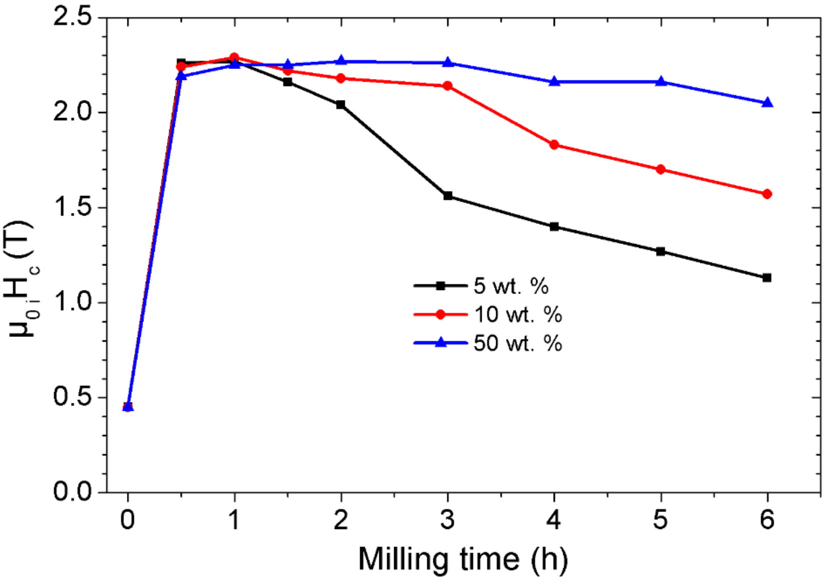

Figure 4.8 Effect of amount of surfactant on coercivity of $SmCo_5$ flakes obtained after SA – ball milling with 5, 10, 50 wt.% oleic acid and 60 wt.% heptane at 800 rpm. The error bars are within the dimension of the symbols.

a better capping of the particles and reduces the milling energy during ball milling. Because of the reduced milling energy the polycrystallization of flakes starts late and is usually less for higher amount of surfactant. As a result, the change of coercivity with milling time is slower for higher amount of surfactant.

4.2 Influence of milling energy

In case of planetary ball mill, the milling energy depends on the powder-to-ball weight ratio and on the rotational speed of the mill [*Sur04*]. The effect of powder-to-ball weight ratio on the morphology of ball-milled powder was reported by Knutson *et. al* [*Knu11*] who observed a decrease of flake thickness with increasing powder-to-ball weight ratio. It is easy to realize that the faster the mill rotates the higher will be the energy input into the powder. This is because of the kinetic energy of the grinding medium ($E = ½ mv^2$, where m is the mass and v is the relative velocity of the grinding medium) is imparted to the powder being milled. Therefore, the kinetic energy supplied to the powder is higher at higher relative velocities of the grinding medium [*Sur04, Cha07b*]. However, as mentioned in section 2.3, there are certain limitations to the maximal speed that could be employed during ball milling. In the present study, the powder-to-ball weight ratio was kept constant and the rotational speed was varied from 200 to 800 rpm to study the effect of milling energy on the properties of the final powder.

Figure 4.9 shows SEM images of magnetically-oriented $SmCo_5$ samples obtained after 4 hours of ball milling at 200, 400 and 800 rpm in 10 wt.% oleic acid and 60 wt.% heptane. It is evident that size and thickness of the flakes decreases with increasing the milling energy. The average diameter and thickness of flakes change rapidly from 200 to 400 rpm but the difference in average diameter and thickness of flakes for 400 and 800 rpm

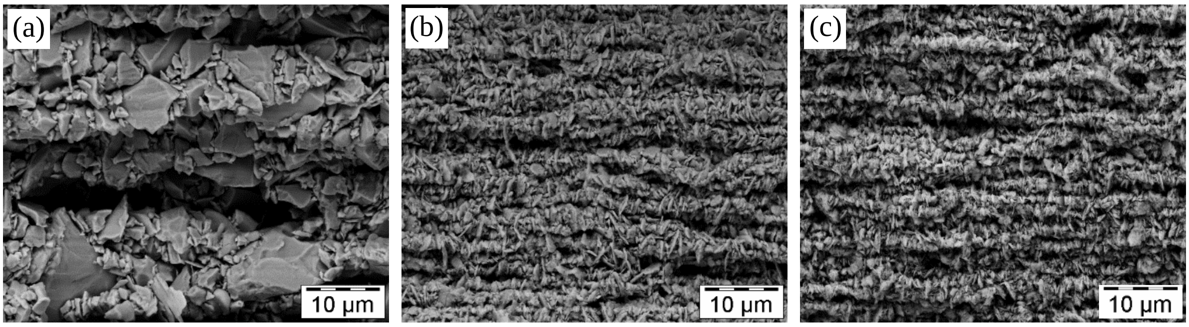

Figure 4.9 Effect of milling energy on morphology (length and thickness) of $SmCo_5$ flakes obtained after 4 h of ball milling with 10 wt.% oleic acid + 60 wt.% heptane at (a) 200 rpm, (b) 400 rpm and (c) 800 rpm.

Table 4.1 Effect of ball milling energy on average grain size of $SmCo_5$ flakes milled with 10 wt.% oleic acid + 60 wt.% n-heptane.

Milling time (h)	Grain size (nm)	
	800 rpm	400 rpm
1	16	35
2	13	26
4	10	15
6	9	11

is not so pronounced. Samples milled at 200 rpm consist of particles of 2-10 μm diameter with a very small fraction of flakes of 1-5 μm diameter and around 500 nm thickness, whereas almost all the particles transform to flakes in case of 400- and 800-rpm-milled samples. A flake diameter in the range of 2-4 μm and an average thickness of 200 nm were obtained for samples milled at 400 rpm. A slight decrease in the diameter (1-3 μm) and thickness (~100 nm) of flakes was observed for samples milled at 800 rpm as compared to that for samples milled at 400 rpm (figure 4.9).

The effect of milling energy on the crystallite size of ball-milled powders was investigated by calculating the average crystallite size from XRD patterns. The average crystallite size was calculated using the Williamson-Hall model [*Wil53*] taking into account the size- and strain-broadening. As shown in Table 4.1, the average crystallite size decreases with increasing milling time and for a given time the average crystallite size is lower for higher milling energy (milling speed). The milling energy has a significant effect on the crystallite size of the flakes; it is clear from Table 4.1 that 1 h of ball milling at 800 rpm is nearly equivalent to 4 h of ball milling at 400 rpm, both producing flakes of nearly the same average crystallite size around 15 nm. The impact energy generated by 200 rpm milling speed was far less compared to 400 and 800 rpm, as a milling time of 35 h is needed to produce the average crystallite size of 17 nm. The difference in the rate of change of average crystallite size is attributed to the difference in the energies imparted to the powders through impacts with milling balls. The milling energy has a significant effect on the texture values of ball-milled samples. Table 4.2 shows the variation of the texture values (I_{002}/I_{111}) with milling time for samples obtained after milling at 200, 400 and 800 rpm with 10 wt.% oleic

Table 4.2 Effect of milling energy on texture values of $SmCo_5$ flakes obtained after ball milling with 10 wt.% oleic acid + 60 wt.% n-heptane at 200, 400 and 800 rpm.

Milling time (h)	**I_{002}/I_{111}**		
	800 rpm	**400 rpm**	**200 rpm**
1	16.0	no (111) peak	
2	8.5	no (111) peak	1030
4	4.0	25	
6	2.5	10	
10			no (111) peak
25			no (111) peak
35			50
60			6
80			4

acid and 60 wt.% heptane. It is evident from Table 4.2 that the texture value continuously decreases from 16 for 1 h of milling to 2.5 for 6 h of milling at 800 rpm. In case of 400-rpm-milled samples no (*111*) or other XRD peaks were visible except the (*00l*)-type peaks, for 1- and 2-h-milled samples, indicating that the flakes were very well oriented in this case. The (*111*) diffraction peaks appeared after further milling and texture values of 25 and 10 were obtained after 4 and 6 h of milling, respectively. This decrease in the texture value is mainly due to the increase in the degree of polycrystallization of flakes with successive ball milling. The texture value for 200-rpm-milled samples increases first and then decreases with further milling. As shown in Table 4.2 a texture value (I_{002}/I_{111}) of 1030 is obtained for 2-h-milled samples which increases with further milling because no (*111*) peaks are visible for the samples milled from 10 to 25 h. This indicates that the particles obtained for these milling times are mostly single-crystalline in nature, which was also reflected in terms of 93 % of degree of texture for the 10-h-milled sample estimated from magnetic measurements. Continued milling results in the development of the (*111*) peak and texture values of 50, 6, and 4 are obtained for milling times of 35, 60, and 80 h, respectively. This suggests that during the early stage of milling bigger polycrystalline particles are crushed to smaller polycrystalline particles as the significantly intense peak of (*111*) was observed for the sample milled for 2 h at 200 rpm. Further milling results in breaking of small polycrystalline particles to single-crystalline particles, as a result no (*111*) peak was obtained for milling from 10 to 25 h at 200 rpm and 1 to 2 h at 400 rpm (table 4.2). This is in contrast to the results obtained by Cui *et al.* [*Ciu11*] and Zheng *et al.* [*Zhe11*], where the texture decreases continuously with relatively small values. Furthermore, the milling results in a decrease of grain size and yields small flakes consisting of nanoparticles which might not be oriented in 2 T field and results in the decrease of the texture value.

Figure 4.10 shows the variation of coercivity, remanence and energy-density with ball milling time for 800- and 200-rpm-milled samples. The coercivity first increases to maximum values of 2.30 T after 1 h, 2.25 T after 4 h and 2.14 T after 35 h of ball milling at 800, 400 and 200 rpm, respectively. The maximum values of coercivity decrease and the milling times corresponding to the maximum value of coercivity increase with decreasing milling energy. This indicates that smaller particles are formed easily at higher milling energy (see figure 4.9) which results in maximum coercivity value due to size effect. It was also observed in the microstructure that flakes obtained after 1 h of milling at 800 rpm were thinner than those obtained after 35 h of milling at 200 rpm, the larger aspect ratio can result in the increased maximum coercivity at higher milling energy. Furthermore, the particles milled for 35 h at 200 rpm see over 8 times more collisions with milling balls than those of 1 h milling at 800 rpm. The higher number of collisions are expected to cause increased surface damage which can attribute to the decrease of the maximum value of coercivity for 200-rpm-milled samples. As shown in figures 4.10 (a) and (b), the remanence values of 200-rpm-milled samples were more than 80 emu/g, whereas 800-rpm-milled samples showed

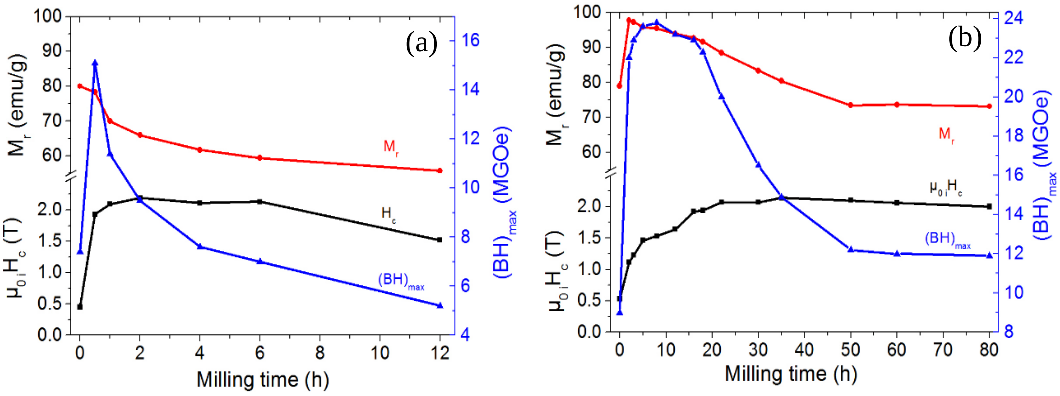

Figure 4.10 Effect of milling energy on coercivity, remanence and energy density of $SmCo_5$ flakes obtained after ball milling with 10 wt.% oleic acid + 60 wt.% n-heptane at (a) 800 rpm and (b) 200 rpm. The error bars are within the dimension of the symbols.

remanence values less than 80 emu/g, just after 1 h of ball milling. This indicates that the fraction of small nanometer-sized flakes and particles was larger in case of samples milled at 800 rpm than that for samples milled at 200 rpm. These nanometer-sized flakes and particles might not be oriented in magnetic field due to their small size and insufficient torque produced by the magnetic field, and hence result in lower remanence values. The faster decrease in remanence in case of 800-rpm-milled samples as compared to those of 200 rpm can be attributed to the fast increase in the amount of nanometer-sized flakes and particles and also due to the accelerated rate of degree of polycrystallization and amorphization because of the higher impact energy imparted to the particles. The coercivity and remanence values stay nearly constant at 2.25 T and 73 emu/g, respectively, after a ball milling of 50 h at 200 rpm, whereas, in case of 800-rpm-milled samples the coercivity and remanence values decrease continuously to 1.52 T and 55.6 emu/g, respectively, after 12 h of milling. This indicates that the intense milling energy at 800 rpm is able to significantly influence the magnetic properties by changing the structure and morphology of the flakes, the milling energy at 200 rpm is not sufficient to alter the magnetic properties. The energy-density of $SmCo_5$ samples was calculated by using the theoretical density of $SmCo_5$ (8.5 g/cc). The milling energy has nearly the same effect on energy-density ($(BH)_{max}$) as the remanence. The maximum value of energy densities of 23 and 15 MGOe were obtained for 200- and 800-rpm-milled samples, respectively (figures 4.10 (a) and (b)). The higher energy-density value in case of milling with 200 rpm is attributed to the increased remanence due to the mostly single-crystalline nature of the particles and reduced fraction of nanometer-sized flakes and particles.

Chapter 5

Heat-treatment and hot-compaction

Ultrafine single-crystalline and textured polycrystalline particles prepared by wet or SA – ball milling have the potential to be used as a hard magnetic phase along with soft magnetic nanoparticles for the preparation of textured nanocomposite magnets [*Pou13, Sko93*]. The mixture of magnetically-hard and -soft phases has to go through high temperature processing in order to achieve exchange-coupling and densely compacted samples. So it is important to study the behavior of these particles after heat-treatment and hot-compaction. It is discussed in the previous chapters that the type of surfactants and/or solvents, the nature of polarity and their amount have some effects on the structural, morphological and magnetic properties. In this chapter, the effects of different heat-treatments and hot-compactions on the structural, morphological and magnetic properties of wet and SA – ball-milled samples are discussed.

The isolated single-crystalline $Nd_2Fe_{14}B$ particles were prepared after ball milling in *abs*. ethanol and n-heptane + oleic acid. Due to differences in the molecular chain length and the polarity of the milling media, the milling time to obtain single-crystalline particles was optimized to 4 h for n-heptane + oleic acid and 2.5 h for *abs*. ethanol. Figures 5.1 (a) and (b) show the SEM images of single-crystalline particles obtained after 4 and 2.5 h of milling in n-heptane + oleic acid and ethanol, respectively. The images show that almost all grains of the original polycrystalline particles are disintegrated into single-crystalline particles of 200 to 500 nm size. These single-crystalline powder samples were heat-treated under high vacuum (~10^{-4} mbar) at 200, 400, 650 and 750 ^{0}C for 0.5 h. No significant difference in morphology was observed in the 200 and 400 ^{0}C heat-treated samples, whereas the particles started to form small agglomerates after 650 and 750 ^{0}C heat-treatments (figures 5.1 (c)-(f)). The agglomeration is expected to be due to the sintering of ultrafine particles. Figure 5.1 shows that the as-milled and heat-treated samples prepared in *abs*. ethanol show nearly the same morphological change except a little increased agglomeration

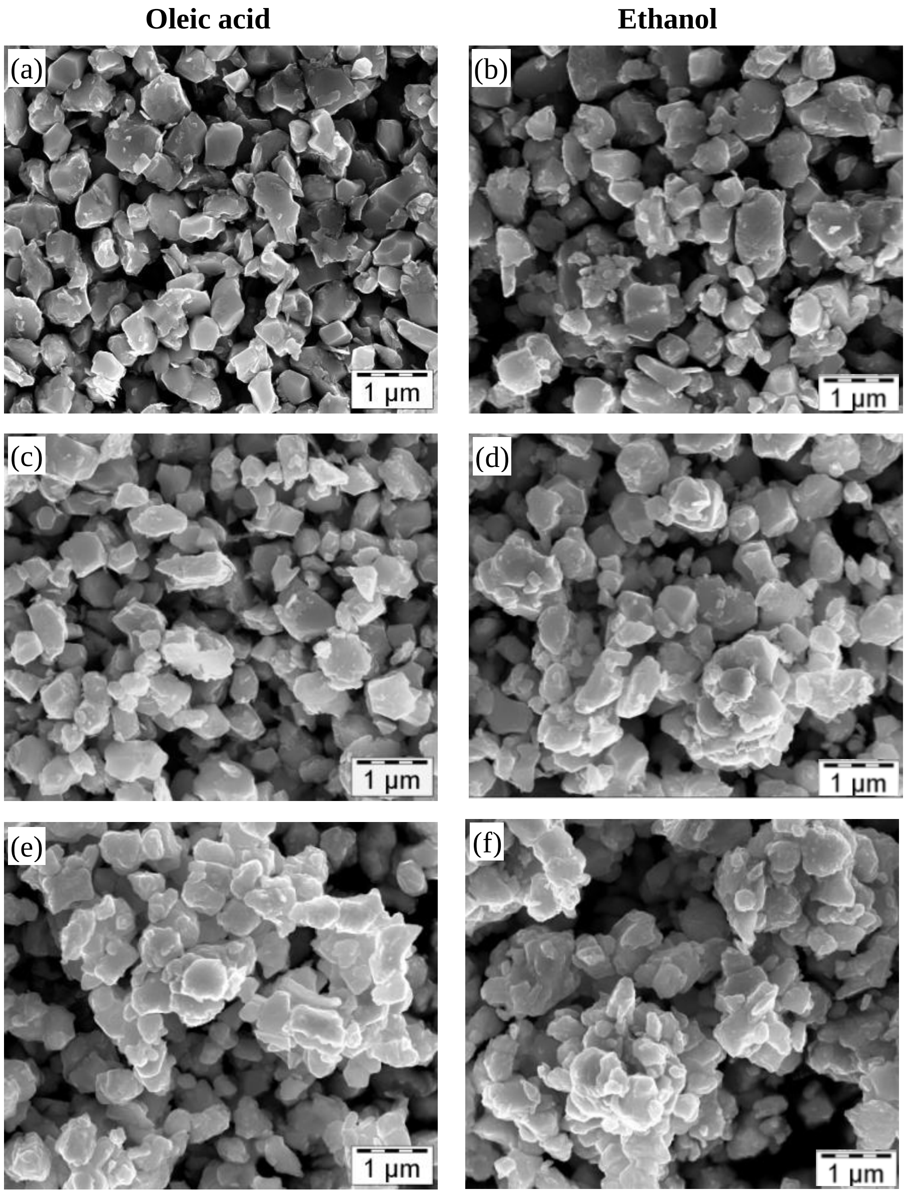

Figure 5.1 Secondary electron SEM images of (a), (b) as-milled, and (c), (d) 400 ^{0}C, (e), (f) 750 ^{0}C heat-treated samples. Left column for oleic acid + n-heptane and right column for *abs*. ethanol ball-milled samples.

in case of 400 and 750 ^{0}C heat-treated ethanol-milled samples, which is possibly due to more surface damage as compared to the oleic-acid-milled samples (see section 4.1.2).

Figure 5.2 shows XRD patterns of un-milled, as-milled and heat-treated samples obtained after milling in *abs*. ethanol and oleic acid + n-heptane. It was observed that for as-milled samples the XRD peaks slightly broaden and shift towards lower 2θ values as compared to the un-milled sample (figure 5.3). The broadening and shift was enhanced in case of ethanol-milled samples compared to those of oleic acid, indicating more induced strain [*Cul01*]. The strain values of 0.14(3)% and 0.21(5)% were calculated using

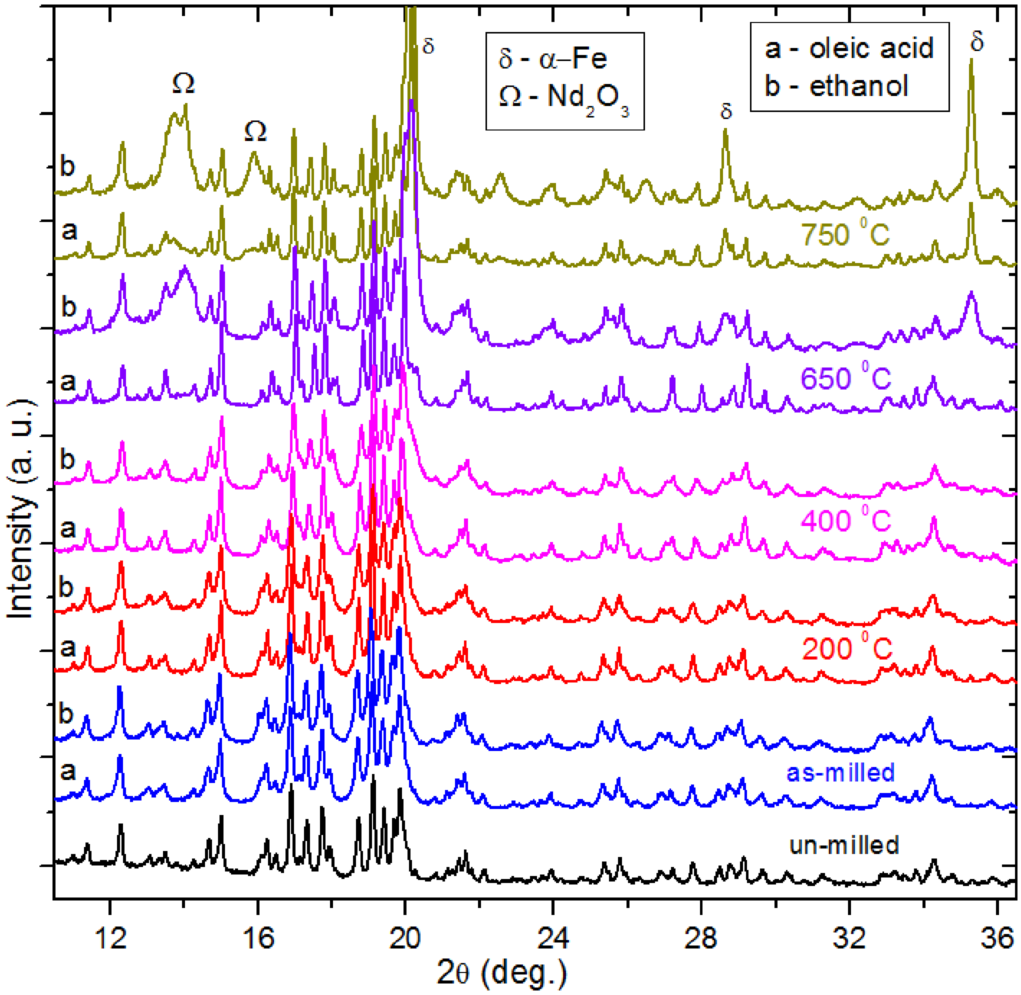

Figure 5.2 XRD patterns of un-milled, as-milled and heat-treated samples of single-crystalline $Nd_2Fe_{14}B$ particles obtained after ball milling in oleic acid + n-heptane and ethanol, showing the presence of α-Fe and Nd_2O_3 phases for annealing temperatures 650 and 750 ^{0}C.

Williamson-Hall method for the as-milled samples ball-milled in oleic acid and *abs.* ethanol, respectively. There was no significant difference in the XRD patterns of ethanol- and oleic-acid-milled samples after 200 ^{0}C heat-treatment which is expected to be due to the removal of induced strain after the heat-treatment. The values of micro-strain obtained for both oleic-acid- and ethanol-milled and 200 ^{0}C heat-treated samples were around 0.08(3)%. The ethanol- and oleic-acid-milled and 400 ^{0}C heat-treated samples also show the same patters except a small hump at $2\theta = 20.15^0$ in case of ethanol samples (figures 5.2 and 5.3). This hump is consistent with the presence of a very small fraction of α-Fe phase. Higher temperature heat-treatments (650 and 750 ^{0}C) cause partial decomposition of the $Nd_2Fe_{14}B$ phase into α-Fe and Nd_2O_3, however the $Nd_2Fe_{14}B$ structure exists at all the stages. Figure 5.4 shows the variation of fractions of α-Fe, Nd_2O_3 and $Nd_2Fe_{14}B$ phases with heat-treatment temperature, obtained after Rietveld refinement with the help of X'Pert HighScore Plus

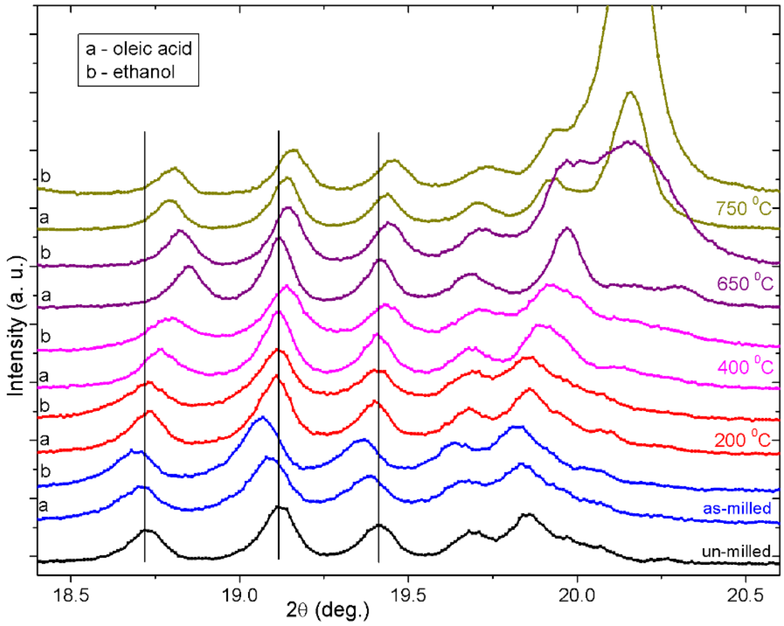

Figure 5.3 Enlarged view of XRD patterns of un-milled, as-milled and heat-treated samples of single-crystalline $Nd_2Fe_{14}B$ particles presented in figure 5.2 showing the shift of XRD peaks at different processing steps.

software. There is no detectable amount of α-Fe and Nd_2O_3 present in oleic-acid-milled samples heat-treated at 200-400 ^{0}C, whereas in case of ethanol-milled samples the fraction of α-Fe and Nd_2O_3 is visible just after the 200 ^{0}C heat-treatment. The level of oxidation and decomposition increases with increase in heat-treatment temperature and is more prominent

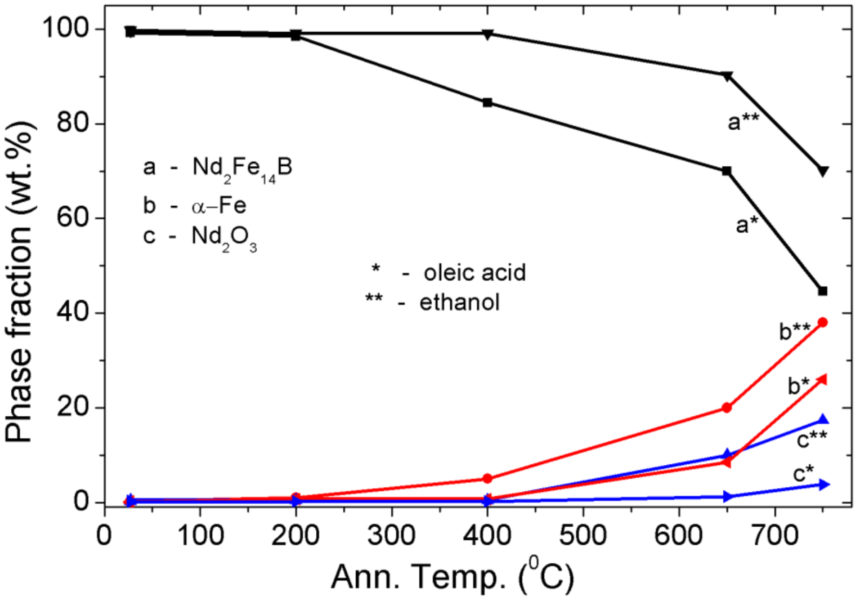

Figure 5.4 Variation of the fraction of α-Fe, Nd_2O_3 and $Nd_2Fe_{14}B$ with heat-treatment temperature of samples obtained after milling in n-heptane + oleic acid and in ethanol. The error in the data are within ±5%.

for ethanol-milled samples than that for oleic-acid-milled samples. The carbon chain length of ethanol (with 2 carbon atoms) is smaller than that of oleic acid (with 18 carbon atoms) and thus more ethanol molecules can get adsorbed on the particle surfaces than oleic acid molecules [*Hub02*, *Bar03*]. The molecules attach to the particle surface through the polar head group containing oxygen [*Idr04*]. Thus, the samples milled in ethanol have more oxygen and so the particles covered with ethanol molecules oxidize more than those in the case of oleic acid. The accelerated decomposition and oxidation at lower temperature for ethanol-milled samples can be due to the lower boiling point of ethanol (boiling point = 78.4 ^{0}C) compared to oleic acid (boiling point = 360 ^{0}C).

The lattice parameters of un-milled, as-milled and differently heat-treated samples were obtained after Rietveld refinement with the help of X'Pert HighScore Plus software. As shown in figure 5.5, the lattice parameters increase after milling, the increase is more pronounced in case of ethanol-milled samples than that for oleic-acid-milled samples, which is possibly due to the increased strain values that were calculated as 0.14(3)% and 0.21(5)% for oleic-acid- and ethanol-milled samples, respectively. The ball milling can possibly result in increased surface damage due to smaller chain length and lower capping ability of ethanol molecules, and therefore the induced micro-strain is increased. After the 200 ^{0}C heat-treatment, the lattice parameters of ethanol milled samples come closer to the value of the starting un-milled powder (figure 5.5) which can attributed to the removal of the induced

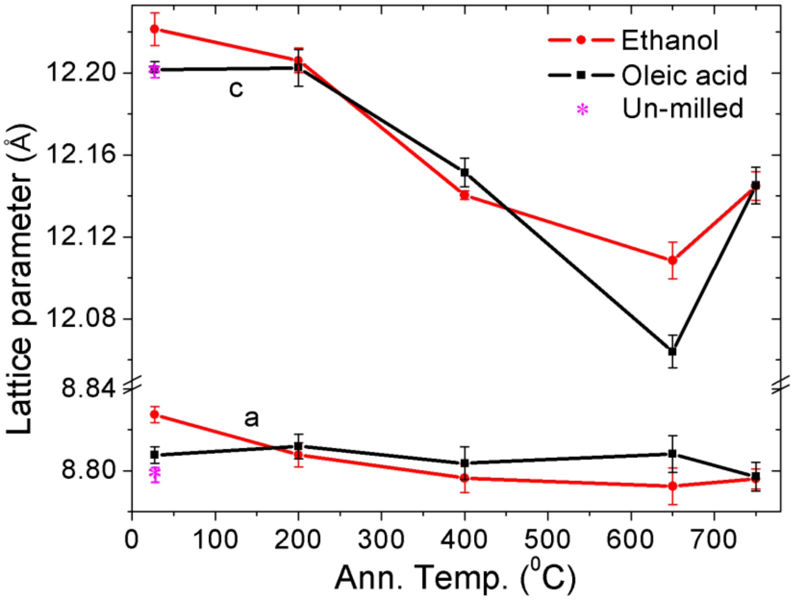

Figure 5.5 Variation of lattice parameters with heat-treatment temperature for $Nd_2Fe_{14}B$ samples obtained after milling in n-heptane + oleic acid and ethanol.

strains that is around 0.08(3)% for both oleic-acid- and ethanol-milled samples. Figure 5.5 shows that the lattice parameter *a* remains nearly constant whereas the lattice parameter *c* changes very rapidly with a maximum decrease at 650 ^{0}C. Nevertheless, all the samples preserve the standard $Nd_2Fe_{14}B$ tetragonal structure (figure 5.2). A similar heat-treatment was carried out on the un-milled HDDR powder and no visible effect was observed on the lattice parameter values which indicates that the decrease in the lattice parameter *c* is not due to Ga and Nb atoms present in very small amount. Carbon atoms present in oleic acid and ethanol are susceptible to diffuse into the $Nd_2Fe_{14}B$ particles after high temperature heat-treatments. As reported by Kou *et al.* [*Kou89*] and de Boer *et al.* [*Boe88*]; $Nd_2Fe_{14}B_{0.5}C_{0.5}$ and $Nd_2Fe_{14}C$ compounds possess the $Nd_2Fe_{14}B$ type tetragonal structure with lattice parameter *c* values of 12.11 and 12.02 Å, respectively (PDF cards 04-005-2203 and 04-005-1187). Additionally, a decrease in lattice parameter *c* with increase of carbon content in the $Nd_{14}Fe_{78}B_{8-x}C_x$ compound was observed by Feng *et al.* [*Fen91*]. Thus, in the present study the fast decrease of the lattice parameter *c* is expected to be due to the substitution of carbon atoms for boron atoms, which results in formation of intermetallic $Nd_2Fe_{14}B_{1-x}C_x$ compound [*Fen91*]. The fact that the lattice parameter *c* decreases due to substitution of carbon atoms for boron atoms can be explained by carbon (r = 70 pm) having a smaller atomic radius than that of boron (r = 90 pm) [*Dan03*].

Demagnetization curves for as-milled and heat-treated samples are presented in figure 5.6 (a) for oleic-acid-milled samples. The initial magnetization curves of as-milled and 200 ^{0}C heat-treated oleic-acid-milled samples are flat at low fields, whereas 400 ^{0}C and higher temperature heat-treated samples show steep initial magnetization curves. This difference in initial magnetization curves at low magnetic field represents the difference in susceptibility of differently heat-treated samples. The coercivity decreases from 1.5 T for un-milled HDDR powder to 0.51 T and 0.26 T for oleic-acid- and ethanol-milled single-crystalline particles, respectively. Similar low coercivities of 0.35 T and 0.44 T have been reported by Cui *et al.* [*Cui12a*] for $Nd_2Fe_{14}B$ nanoflakes (0.5-3 μm) and by Simeonidis *et al.* [*Sim11*] for elongated $Nd_2Fe_{14}B$ nanoparticles (~15 nm), respectively, obtained using SA – ball milling. This sharp drop in coercivity is attributed to a morphological change due to splitting of large hundred-micrometer-sized particles to single-crystalline sub-micrometer particles. The lower coercivity for ethanol-milled samples as compared to that of oleic-acid-milled samples is expected to be due to an increased amount of surface damage and

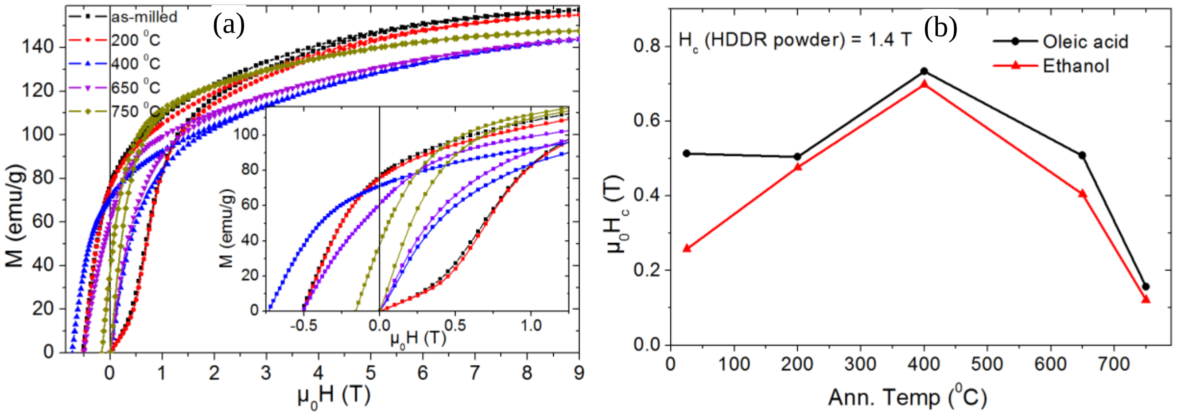

Figure 5.6 (a) Demagnetization curves for as-milled and heat-treated samples obtained after milling in oleic acid + n-heptane and (b) variation of coercivity with heat-treatment temperature for oleic acid + n-heptane and ethanol milled samples. The error bars are within the dimension of the symbols.

increased density of defect sites. Coercivity increases from 0.51 T to 0.73 T for oleic-acid-milled sample and from 0.26 T to 0.70 T for ethanol-milled samples after an optimal heat-treatment at 400 ^{0}C and decreases with further increase in heat-treatment temperature. In previous reports a maximum coercivity enhancement from 0.37 T to 0.51 T for olylamine-milled $Nd_2Fe_{14}B$ flakes (0.5-10 μm) and from 0.23 T to 0.28 T for ethanol-milled $Nd_2Fe_{14}B$ flakes (0.7-18 μm) has been observed after an optimal heat-treatment at 450 ^{0}C [*Cui12a*]. In the present study of single-crystalline particles, the improvement in coercivity is far higher. The initial increase in coercivity till 400 ^{0}C heat-treatment can be attributed to the removal of induced micro-strain and defects, and smoothening of grain surfaces. It is mentioned earlier in this section that the micro-strain values decrease from 0.14(3)% and 0.21(5)% for oleic-acid- and ethanol-as-milled samples, respectively, to around 0.08(3)% after a heat-treatment at 200 ^{0}C for both oleic-acid- and ethanol-milled samples. The micro-strain value for both oleic-acid- and ethanol-milled and 400 ^{0}C heat-treated samples were about 0.05(3)% which is very less as compared to that for the as-milled samples. This observation indicates that almost all the micro-strains are removed after a heat-treatment at 400 ^{0}C. It was reported by Vial *et al.* [*Via02*], Menushenkov *et al.* (*Men03*) and Woodcock *et al.* [*Woo14*] that the coercivity of sintered $Nd_2Fe_{14}B$ magnets increase after post-sinter annealing at low temperature in the range of 400-600 ^{0}C due to smoothening and homogeneity of the Nd-rich grain boundaries. The peak in coercivity value after a heat-treatment at 400 ^{0}C in this study is consistent with the above results and is expected to be due to smoothening of the particle surfaces which are covered with Nd-rich layer [*Güt11, Gut03*]. As mentioned earlier in this section, a carbon diffusion is possible at higher temperature heat-treatments [*Dan03, Fen91, Boe88*]. The decrease in coercivity in this study after 650 and 750 ^{0}C heat-treatments (figure 5.6 (b)) is in agreement to the decrease in coercivity with increasing carbon-content reported by Daniil *et al.* [*Dan03*] and Feng *et al.* [*Fen91*], again indicating a possible carbon substitution for boron in $Nd_2Fe_{14}B$ crystals after heat-treatments. Further, the decrease in coercivity can be attributed to the increased oxidation and formation of magnetically-soft α-Fe phase. These phases act as low anisotropy sites and can form reverse magnetizations which results in the sharp drop in coercivity due to a reverse domain nucleation effect (see section 1.3.3 and 3.2.1.2). An insignificant change in coercivity for the 200 ^{0}C sample as compared to that of the as-milled oleic acid sample was observed which may be because of very small amount of micro-strain present in the as-milled sample (discussed earlier in this section). The magnetization at 9 T decreases with increasing heat-treatment temperature which can be attributed to partial oxidation. The initial magnetization increases rapidly at low applied field for 650 and 750 ^{0}C heat-treated samples and the changes are rapid for the 750 ^{0}C sample than for the 650 ^{0}C sample. This can be attributed to the increased fraction of soft magnetic α-Fe phase at higher heat-treatment temperature, as shown in figure 5.2 and discussed earlier. However, a decrease of

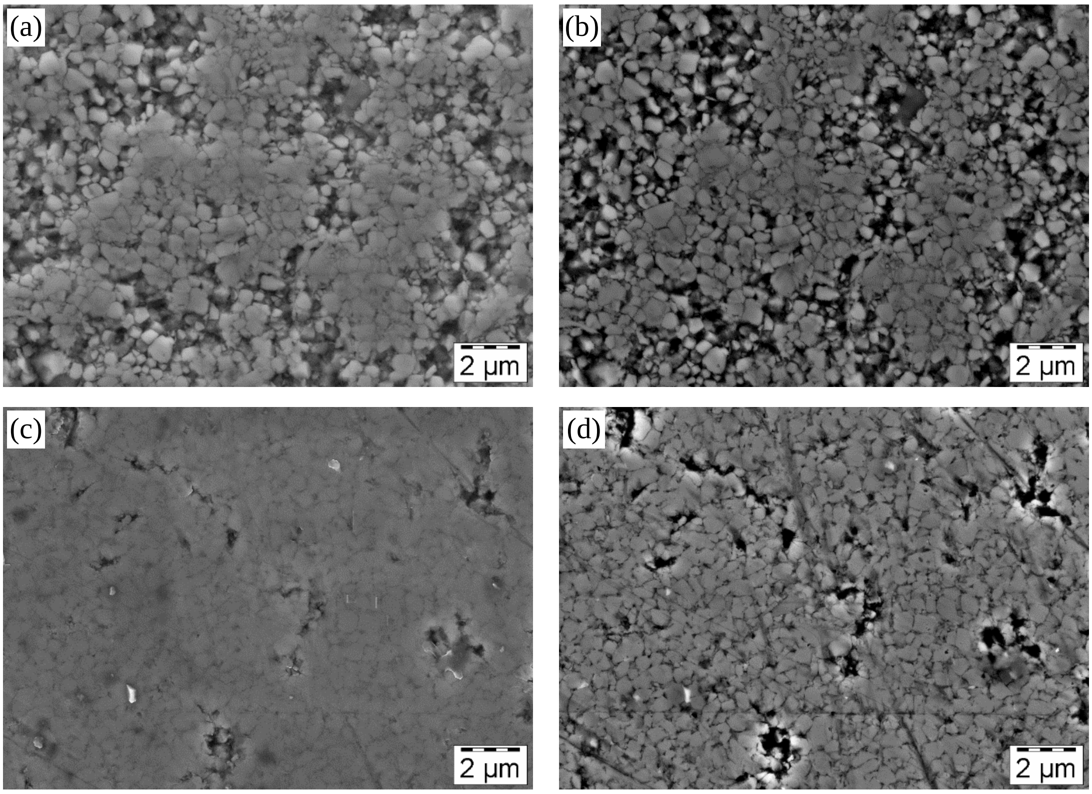

Figure 5.7 Secondary electron (left column) and back scattered electron (right column) SEM images of hot compacted single-crystalline $Nd_2Fe_{14}B$ particles at temperature (a), (b) 650 ^{0}C and (c), (d) 750 ^{0}C obtained after milling in oleic acid + n-heptane.

saturation magnetization is expected with the increase of carbon atom replacement for boron atoms in $Nd_2Fe_{14}B$ crystals [*Dan03, Bol85*], the presence of significantly large fraction of α-Fe phase leads to higher magnetization at 9 T. The hysteresis loop and coercivity of heat-treated ethanol-milled samples were nearly the same as that of oleic-acid-milled samples, except a fast decrease of magnetization at 9 T which is attributed to the increase oxidation as compared to that of oleic-acid-milled samples (see figures 5.2 and 5.3).

Figure 5.7 shows SEM images of hot-compacted single-crystalline particles obtained after ball milling in oleic acid + n-heptane. The samples were hot-compacted at temperatures 650 and 750 ^{0}C under vacuum at a pressure of 300 MPa. Figure 5.7 shows that the 650 ^{0}C compacted sample has a very porous structure. Increasing the temperature to 750 ^{0}C results in a better compaction, the density of compacted samples increases from around 6 gm/cc for 650 ^{0}C to around 7 gm/cc for 750 ^{0}C. It is well known that Nd-Fe-B MQ powders can be fully compacted at around 725 ^{0}C at a pressure of 150 MPa [*Bro02b, Lie98, Sai98*]. In the case of ball-milled powder, where the particle size is far less than that for MQ powder,

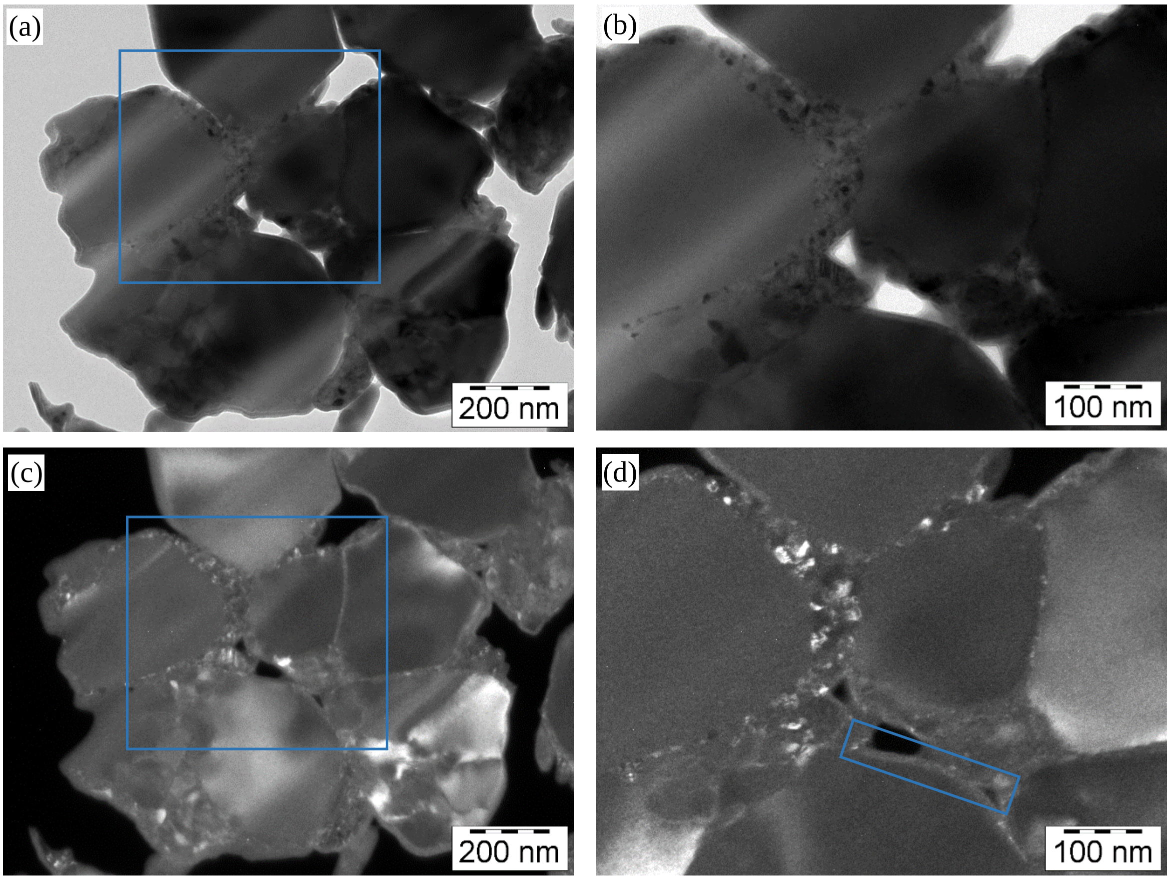

Figure 5.8 (a), (b) bright field and (c), (d) dark field TEM images of single crystalline $Nd_2Fe_{14}B$ particles hot compacted at 750 ^{0}C obtained after milling in n-heptane + oleic acid. (b) and (d) give a magnified view of a selected region in (a) and (c) , respectively.

the compaction at 150 MPa is very poor and the sample could be broken by pressing between fingers. So, here a higher compaction pressure of 300 MPa was used. The full compaction at 725 ^{0}C for Nd-Fe-B MQ powder is reported to be due to the melting of the Nd-rich phase [*Mat85*, *Dav01*]. The back scattered electron (BSE) image (figure 5.7) of samples compacted at 650 ^{0}C shows very small compacted (dense) regions, while the rest of the particles seem to be loose in the sample. Figures 5.7 (c) and (d) show that increasing the temperature of compaction to 750 ^{0}C results in better compaction of the powder without loose particles but some pores are still visible in the compacted sample. The BSE image in figure 5.7 (d) with a better phase contrast reveals that the individual particles are separated by a thin grain boundary phase which could be the Nd-oxide phase due to the partial surface oxidation during compaction. TEM analysis was performed in order to investigate the interface region of hot-compacted samples. Figure 5.8 shows the bright field and dark field images of the sample hot-compacted at 750 ^{0}C. It was observed that the grain size remains the same as the particle size of the original powder. Some small crystallites (< 10 nm) with different contrast are visible in the interface regions in both BF and DF images. The width of the interfacial region varies from 10 to 50 nm, the larger width can be due to accumulation of small nanoparticles (~10 nm) between two particles. As shown in the marked region of figure 5.8 (d), the bright edge of a single particle is around 5 nm which is likely to be the oxide phase around the particle.

Chapter 6

Summary and outlook

Summary

Hard magnetic ($SmCo_5$ and $Nd_2Fe_{14}B$) nanometer-sized particles and flakes have been prepared by SA – ball milling. The work was focused on understanding the formation mechanism of nanoparticles and nanoflakes and studying their microstructural and magnetic properties with the perspective of using them for fabrication of high-energy-density nanocomposite permanent magnets. The influence of different milling media and milling energy on the characteristics of ball-milled powder was investigated. Sub-micrometer-sized single-crystalline $Nd_2Fe_{14}B$ particles were subjected to thermal treatments and the changes in microstructural and magnetic properties were studied.

SA – ball milling of starting $SmCo_5$ particles resulted in fracturing of the tens of micrometer-sized particles to single-micrometer-sized particles. In the early stage of milling single-crystalline particles were formed by inter-granular fracture while successive ball milling causes transformation of single-crystalline particles into flakes and simultaneous thinning of flakes occurs by splitting along easy-glide planes. Flakes of around 2 μm diameter and around 500 nm thickness were obtained after 0.5 h of ball milling in oleic acid and n-heptane at 800 rpm. The thickness decreased with further ball milling and the flakes were arranged face-to-face in form of a ring structure due to strong texture and magnetostatic attraction. Single-crystalline particles and textured polycrystalline flakes of $Nd_2Fe_{14}B$ were obtained after SA – ball milling of d-HDDR processed $Nd_2Fe_{14}B$ powder. The starting d-HDDR particles consisting of 200-500 nm grains were fully disintegrated *via* inter-granular fracture into isolated single-crystalline particles after 4 h of SA – ball milling at 400 rpm. Intensive ball milling at 800 rpm resulted in a transformation of single-crystalline particles into textured polycrystalline flakes of diameter 0.2 μm to 1.0 μm. More importantly, using SA – ball milling, ultrafine single-crystalline $Nd_2Fe_{14}B$ particles were prepared in bulk amount of tens of grams. The $SmCo_5$ flakes showed [*00l*] out-of-plane

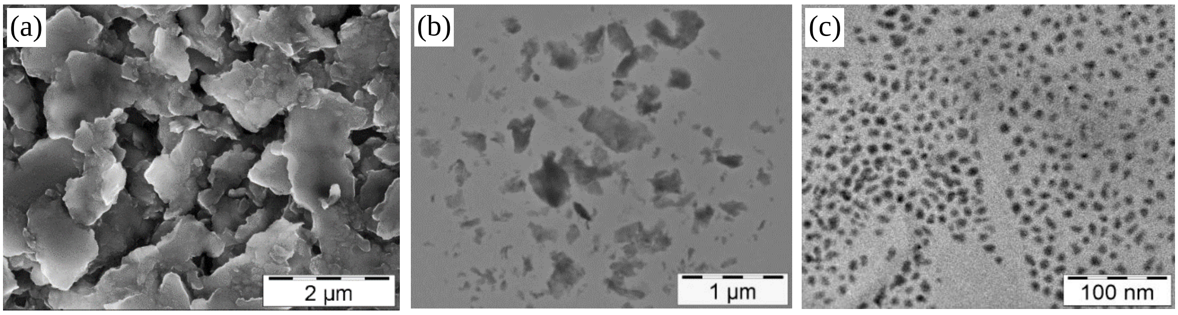

Figure 6.1 (a) Secondary electron SEM image showing single micron size flakes, bright field TEM images of (b) smaller nanoflakes and (c) nanoparticles of $SmCo_5$ separated by size-selection process after SA – ball milling in 10 wt.% oleic acid and 60 wt.% heptane.

orientation and aligned face-to-face in form of a chain under an external magnetic field, whereas the $Nd_2Fe_{14}B$ flakes had [*00l*] in-plane orientation and were aligned edge-to-edge in an external magnetic field. Prolonged ball milling resulted in breaking of these micrometer long polycrystalline flakes into smaller flakes (< 500 nm) due to the presence of defects, dislocations and deformations introduced by ball milling. Nanoparticles of around 15 nm size were formed by breaking of smaller flakes along grain boundaries. Different sizes of nanoflakes and nanoparticles were separated using a size-selection process and are shown in figure 6.1 for $SmCo_5$ samples. The characteristics of the liquid media such as polarity and chain length of solvents and surfactants play a critical role on the formation and properties of flakes and nanoparticles. The use of ethanol (polar solvent) prevented re-welding during ball milling, by attaching on the particle surfaces through the oxygen in the polar head groups. The effect of ball milling in n-heptane (non-polar solvent) was similar to that of dry ball milling and resulted in agglomerated and re-welded particles. Surfactants which are less polar than ethanol provide better capping to the particles due to their long molecular chains and as a result, the flakes and particles are well dispersed. High-aspect-ratio flakes and nanoparticles were obtained after SA – ball milling. A significantly reduced degree of surface damage and improved magnetic properties were observed for samples obtained after ball milling in the presence of surfactants as compared to those of milling in non-surfactants. The difference in morphologies of $Nd_2Fe_{14}B$ samples obtained after ball milling in the presence of ethanol and oleic acid + n-heptane are shown in figure 6.2.

Room temperature coercivity of SA – ball-milled $SmCo_5$ powders increased first to a peak value of 2.3 T which is attributed to a decrease in particle size. The decline in coercivity with further ball milling can be due to partial amorphization and formation of nanometer-sized crystallites. The peak values of coercivity of SA – ball-milled $SmCo_5$

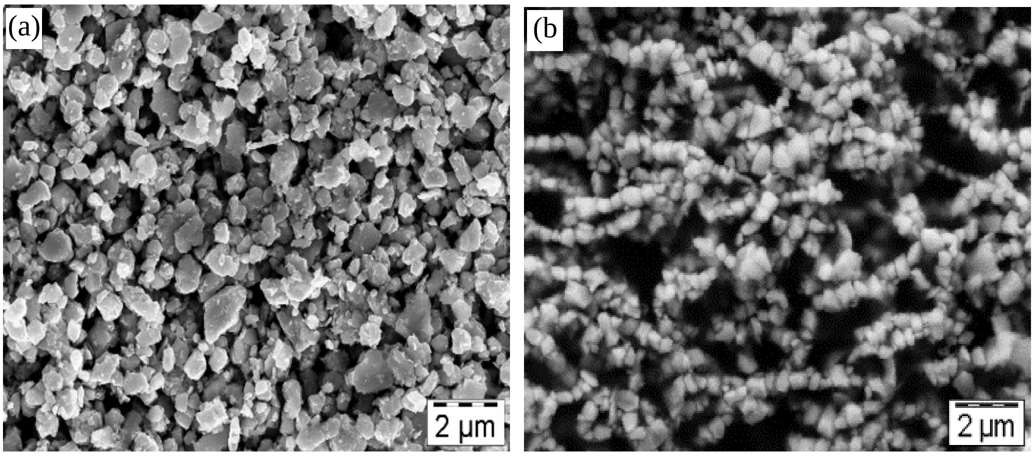

Figure 6.2 Secondary electron SEM images of $Nd_2Fe_{14}B$ particles obtained after ball milling in (a) 100 wt. % ethanol and (b) 50 wt. % oleic acid + 60 wt. % n-heptane at 400 rpm.

powders were nearly the same for varied amount of surfactant (5, 10, 50 wt.%); a rapid drop in coercivity was observed for a lower amount of surfactants. The increased amount of surfactants provides a better capping over the particles and reduces the milling energy having the result that amorphization and formation of nanometer-sized crystallites start late and so the drop in coercivity with milling time was slower for higher amount of surfactants. The coercivity of SA – ball-milled $Nd_2Fe_{14}B$ particles decreased drastically from 1.4 T for un-milled d-HDDR powders to 0.44 T after 0.5 h of SA – ball milling. A coercivity of 0.34 T was obtained for isolated single-crystalline $Nd_2Fe_{14}B$ particles, whereas polycrystalline nanoflakes showed a very small coercivity of 0.11 T. The result of this low coercivity deviates from the Stoner-Wohlfarth-prediction for single-domain particles. The low coercivity is possibly due to an introduction of low anisotropy defect sites on the surfaces of ball-milled $Nd_2Fe_{14}B$ particles.

A direct correlation between the spin reorientation temperature and the intergrain exchange-coupling was observed in the $Nd_2Fe_{14}B$ samples. The spin reorientation temperature increased from 129 K for un-milled d-HDDR powder to 136.5 K for single-crystalline particles, polycrystalline flakes with grain size of around 12 nm showed a spin reorientation temperature of 128.5 K. The reduced value of the spin reorientation temperature for d-HDDR powder as compared to bulk single-crystalline samples (135 K) is due to exchange-coupling between fine grains. Splitting of the grains eliminates the exchange-coupling and as a result the spin reorientation increases to the bulk single-crystal value. The intergrain exchange-coupling becomes predominant in case of polycrystalline

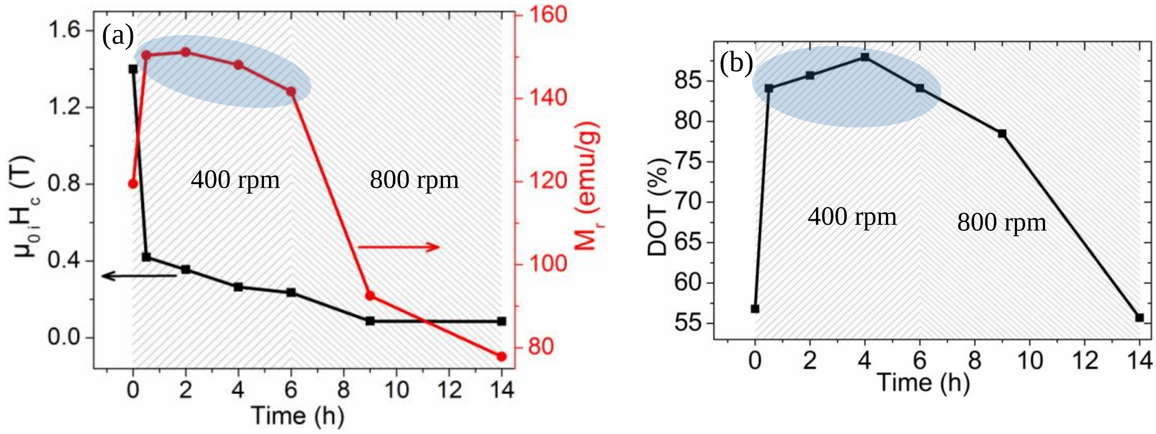

Figure 6.3 Variation of (a) coercivity and remanent magnetization measured in parallel direction to orienting magnetic field and (b) degree of texture with milling time for $Nd_2Fe_{14}B$ particles SA – ball-milled with 50 wt.% oleic acid + 60 wt.% heptane. The error bars in (a) are within the dimension of the symbols.

flakes (with ~12 nm grain size) obtained after SA – ball milling of single-crystalline particles and as a result the spin reorientation temperature was decreased.

A high degree of texture (DOT) was observed in magnetically-oriented samples of SA – ball-milled particles and flakes. The remanent magnetization increased from 48 emu/g for randomly-oriented samples to 97.8 emu/g for magnetically-oriented $SmCo_5$ samples obtained after milling in 10 wt.% oleic acid + 60 wt.% n-heptane at 200 rpm. The DOT values estimated from the demagnetization curves measured in parallel and perpendicular direction of magnetically-oriented samples showed a maximum value of 93 % for $SmCo_5$ samples. The DOT values obtained from magnetic measurements were in agreement with the texture values estimated from the XRD patterns of magnetically-oriented samples. The remanence value was increased to 148 emu/g for magnetically-oriented isolated single-crystalline $Nd_2Fe_{14}B$ particles, which was far higher than those for oriented un-milled powder (120 emu/g). A DOT value of 88 % was obtained for single-crystalline $Nd_2Fe_{14}B$ particles which was reduced for polycrystalline flakes to a value of 55 %, nearly the same as for un-milled powder. The variation of coercivity, remanent magnetization and DOT values with milling time for SA – ball-milled $Nd_2Fe_{14}B$ samples is shown in figure 6.3.

The isolated single-crystalline $Nd_2Fe_{14}B$ particles started to agglomerate at high temperature (> 400 ^{0}C) heat-treatments. An increase of α-Fe and Nd_2O_3 phases and a sharp change of the lattice parameter *c* of $Nd_2Fe_{14}B$ was observed when heat treating above 400 ^{0}C. The change in lattice parameter after higher temperature heat-treatment is thought to be due to partial substitution of carbon atoms present in the surfactants or solvents for boron atoms. No significant difference in morphology was observed for low temperatures heat-treatments. The coercivity was increased at low temperature heat-treatment and hot-compaction. A remarkable enhancement of 169 % (from 0.26 T to 0.70 T) and 43 % (from 0.51 T to 0.71 T) in coercivity of ethanol- and oleic-acid-milled samples, respectively, was observed after the 400 ^{0}C heat-treatment.

It has been shown that SA – ball milling is a very useful and efficient technique to fabricate various size and shape of nanoparticles and nanoflakes of RETM compounds. Fabrication mechanism, influence of different milling parameter and effect of thermal treatments on the characteristics of ball-milled particle and flakes have been investigated.

Outlook

The technique of SA – ball milling results in a broad size distribution of particles ranging from 10 nm to 10 μm. Only a small fraction (~10 wt.%) of nanoparticles could be separated using a size-selection process. An alternative method needs to be developed for separating the nanoparticles from the mixture and to increase the yield of nanoparticles. As it has been shown in the case of d-HDDR powders, the production of nanoparticles in bulk amount can be possible by choosing nanocrystalline starting materials for ball milling. Furthermore, the nanometer-sized particles get amorphous and possibly the composition and crystal structure change.

The investigation of a rapid drop in coercivity of single-domain-sized single-crystalline $Nd_2Fe_{14}B$ particles needs to be addressed. It would be interesting to understand the origin of coercivity, anisotropy and the change in susceptibility of ball-milled nanoparticles and flakes. The study of surface morphology, composition and inter-granular region of polycrystalline flakes is of great importance for a better understanding of SA – ball-milled nanoparticles and flakes.

The presence of surfactants and/or solvents over the particles and flakes causes a partial decomposition or a surface oxidation after high temperature heat-treatments. There is a great need to find a suitable route to completely wash out the organics from the ball-milled particles. An alternate route for the preparation of nanometer- or sub-micrometer-sized particles by jet-milling can be useful, where grinding takes place only by particle-to-particle collision. Additionally, soft magnetic nanoparticles without any coating of organics are needed, which can later be combined with the hard magnetic particles to prepare the textured nanocomposite permanent magnets. A state of the art technique has to be developed in order to form a homogeneous mixture of magnetically-hard and -soft phases and then to compact the mixture for nanocomposite magnets. Single-crystalline and textured polycrystalline hard magnetic nanoparticles and flakes prepared by surfactant- and non-surfactant-assisted ball milling have great potential for the preparation of high-energy-density textured nanocomposite magnets but there are several problems to be solved before realizing a real high-energy-density nanocomposite permanent magnet.

Acknowledgements

With regards and profound respect, I avail this opportunity to express my deep sense of gratitude to Prof. Ludwig Schultz for providing me the opportunity to work at the Institute for Metallic Materials, IFW Dresden.

I thank Dr. Karl-Hartmut Müller for valuable and fruitful discussions during group meetings and individually. His vast knowledge and immense experiences inspired me to learn magnetism. I would like to thank Prof. O. Gutfleisch for his support during this work, reading the thesis and providing with the valuable suggestions.

I thank Bernhard Gebel, Monika Herrich, Kerstin Pitruff, Dr. Konstantin Nenkov, Christina Damm, Almut Pöhl, Tina Sturm, Katja Berger and Alexander Schubert for their invaluable technical help and kindness that made my lab work enjoyable and simple.

I would like to thank my colleagues and friends at the IFW, who through their competent help, scientific and non-scientific discussions, created a nice atmosphere both at work and outside the lab: Dr. Thomas George Woodcock, Maria Krautz, Inge Lindemann, Juliane Thielsch, Konrad Güth, Konrad Löwe, Simon Sawatzki, Imants Dirba, Christian Bonatto Minella, Florian Bittner, Torsten Mix, Dr. James David Moore, Dr. Martina Moore, Dr. Volker Neu, Dr. Silke Hampel, Dr. Santosh Kumar Bhandari, Prashanth, Sujeet.

I gratefully acknowledge the *Siemens /DAAD post graduate fellowship* provided by Siemens AG and Deutscher Akademicher Austausch Dienst (DAAD) for pursuing my Ph.D. study. I thank Dr. Manfred Rührig, Siemens AG., for his support and fruitful discussions.

Finally, I am grateful to my parents, brother and sister for their continuous encouragement, love and support.

References:

[*Akd10*] N. G. Akdogan, G. C. Hadjipanayis and D. J. Sellmyer, *Novel $Nd_2Fe_{14}B$ nanoflakes and nanoparticles for the development of high energy nanocomposite magnets*, Nanotechnology 21 (2010) 295705.

[*Alb78*] R. Alben, J. J. Becker and M. C. Chi, *Random anisotropy in amorphous ferromagnets*, J. Appl. Phys. 49 (1978) 1653.

[*Bal12*] B. Balamurugan, D. J. Sellmyer, G. C. Hadjipanayis and R. Skomski, *Prospects for nanoparticle-based permanent magnets*, Scripta Materialia, 67 (2012) 542.

[*Bar03*] S. M. Barlow and R. Raval, *Complex organic molecules at metal surfaces: bonding, organization and chirality,* Surf. Sci. Rep. 50 (2003) 201.

[*Blu01*] S. Blundell, *Magnetism in condensed matter*, Oxford master series in condensed matter physics, University Press, NY (2001). (book)

[*Boe88*] F. R. de Boer, R. Verhoef, Z. Zhi-dong, D. B. de Mooij and K. H. J. Buschow, *Magnetic properties of $Nd_2Fe_{14}C$ and some related pseudoternary compounds*, J. Magn. Magn. Mater. 73 (1988) 263.

[*Bol02*] A. Bollero, O. Gutfleisch, K. -H. Mueller, L. Schultz and G. Drazic, *High-performance nanocrystalline PrFeB-based magnets produced by intensive milling*, J. Appl. Phys. 91 (2002) 8159.

[*Bol85*] F. Bolzoni, F. Leccabue, L. Pareti, and J. Sanchez, *Magnetic anisotropy of carbon doped $Nd_2Fe_{14}B$*, J. Phys. Colloques 46 (1985) C6-305.

[*Bro02a*] F. J. A. den Broeder, W. Hoving and P. J. H. Bloemen, *Magnetic anisotropy of multilayers,* J. Magn. Magn. Mater. 93 (2002) 562.

[*Bro02b*] D. Brown, B. M. Ma and Z. Chen, *Developments in the processing and properties of NdFeB-type permanent magnets,* J. Magn. Magn. Mater. 248 (2002) 432.

[*Cal07*] W. D. Callister, *Materials Science and Engineering: An Introduction*, 7th Edition, John Wiley & Sons., Inc., New York (2007). (book)

[*Cam05*] M. F. de Campos and F. J. G. Landgraf, *Determination of intrinsic magnetic parameters of* $SmCo_5$ *phase in sintered samples*, Mater. Sci. Forum 498-499 (2005)129.

[*Cam06*] M. F. de Campos, *Effect of grain size, lattice defects and crystalline orientation on the coercivity of sintered magnets*, Mater. Sci. Forum 530-531 (2006) 146.

[*Cam94*] S. J. Campbell, W. A. Kaczmarek, E. Wu and K. D. Jayasunya, *Surfactant assisted ball-milling of barium ferrite*, IEEE Trans. Magn. 30 (1994) 742.

[*Cha06*] V. M. Chakka, B. Altuncevahir, Z. Q. Jin, Y. Li and J. P. Liu, *Magnetic nanoparticles produced by surfactant-assisted ball milling*, J. Appl. Phys. 99 (2006) 08E912.

[*Cha07a*] G. S. Chaubey, C. Barcena, N. Poudyal, C. B. Rong, J. Gao, S. Sun and J. P. Liu, *Synthesis and stabilization of FeCo nanoparticles*, J. Am. Chem. Soc. 129 (2007) 7214.

[*Cha07b*] H. G. Cha, Y. H. Kim, C. W. Kim, H. W. Kwon and Y. S. Kang, *Characterization and magnetic behavior of Fe and Nd-Fe-B nanoparticles by surfactant-capped high-energy ball mill*, J. Phys. Chem. C 111 (2007) 1219.

[*Cha11*] G. S. Chaubey, N. Poudyal, Y. Liu, C. B. Rong and J. P. Liu, *Synthesis of Sm-Co and Sm-Co/Fe nanocrystals by reductive annealing of nanoparticles*, J. Alloy Comp. 509 (2011) 2132.

[*Che11*] C. H. Chen, S. J. Knutson, Y. Shen, R. A. Wheeler, J. C. Horwath and P. N. Barnes, *The effect of particle size on coercivity and crystallinity of* $SmCo_5$, Appl. Phys. Lett. 99 (2011) 012504.

[*Chi97*] S. Chikazumi and C. D. Graham, *Physics of Ferromagnetism* 2^{nd}*. Ed.*, Oxford University Press (1997). (book)

[*Coc66*] A. Cochardt, *Recent ferrite magnet developments*, J. Appl. Phys. 37 (1966) 1112.

[*Coe10*] J. M. D. Coey, *Magnetism and Magnetic Materials*, Cambridge University Press (2010). (book)

[*Coe11*] J. M. D. Coey, *Hard Magnetic Materials: A Perspective*, IEEE Trans. Magn. 47 (2011) 4671.

[*Coe12*] J. M. D. Coey, *Permanent magnets: Plugging the gap*, Scripta Materialia 67 (2012) 524.

[*Coe88*] R. Coehoorn, D. B. de Mooij, J. P. W. B. Duchateau and K. H. J. Buschow, *Novel permanent magnetic materials made by rapid quenching, J. Phys. Colloques 49 (1988) C8-669.*

[*Coe94*] J. M. D. Coey, K. O'Donnell, Q. Qi, E. Touchais and K. H. Jack, *The magnetism of* α''*-*$Fe_{16}N_2$, J. Phys.: Condens. Matter. 6 (1994) L23.

[*Coe95*] J.M.D. Coey, *Rare-earth magnets*, Endeavor 19 (1995), 146.

[*Coe96*] J. M. D. Coey, *Rare-earth iron permanent magnets*, Oxford university press (1996). (book)

[*Cro12*] C. A. Crouse, E. Michel, Y. Shen, S. J. Knutson, B. K. Hardenstein, J. E. Spowart, S. O. Leontsev, S. L. Semiatin, J. Horwath, Z. Turgut and M. S. Lucas, *Effect of surfactant molecular weight on particle morphology of* $SmCo_5$ *prepared by high energy ball milling*, J. Appl. Phys. 111 (2012) 07A724.

[*Cro84*] J. J. Croat, J. F. Herbst, R. W. Lee and F. E. Pinkerton, *Pr-Fe and Nd-Fe based magnets: A new class of high-performance permanent magnets*, J. Appl. Phys. 55 (1984) 2079.

[*Cui11*] B. Z. Cui, W. F. Li and G. C. Hadjipanayis, *Formation of* $SmCo_5$ *single-crystal submicron flakes and textured polycrystalline nanoflakes,* Acta Mater. 59 (2011) 563.

[*Cui12a*] B. Z. Cui, L. Y. Zheng, W. F. Li, J. F. Liu and G. C. Hadjipanayis, *Single-crystal and textured polycrystalline* $Nd_2Fe_{14}B$ *flakes with a submicron or nanosize thickness,* Acta Materialia 60 (2012) 1721.

[*Cui12b*] W. -B. Cui, Y. K. Takahashi and K. Hono, $Nd_2Fe_{14}B/FeCo$ *anisotropic nanocomposite films with a large maximum energy product*, Adv. Mater. 24 (2012) 6530.

[*Cul01*] B. D. Cullity and S. R. Stock, *Elements of X-ray diffraction*, Addison-Wesley (2001). (book)

[*Cul72*] B. D. Cullity, *Introduction to magnetic materials*, Reading, MA, USA: Addison-Wesley (1972). (book)

[*Dan03*] M. Daniil, H. Okumura, G.C. Hadjipanayis and D.J. Sellmyer, *Effect of carbon substitution on the magnetic properties of Nd-Fe-(B,C) nanocomposite magnets*, J. Magn. Magn. Mater. 267 (2003) 316.

[*Das69*] D. DAS, *Twenty million energy product samarium-cobalt magnet*. Magnetics, IEEE Trans. Magn. 5 (1969) 214.

[*Dav01*] B. E. Davies, R. S. Mottram and I. R. Harris, *Recent developments in the sintering of NdFeB*, Mater. Chem. Phys. 67 (2001) 272.

[*Doe11*] U.S. Department of Energy, *Critical materials strategy*, December 2011.

[*Elk05*] K. Elkins, D. Li, N. Poudyal, V. Nandwana, Z. Q. Jin, K. Chen and J. P. Liu, *Monodisperse face-centred tetragonal FePt nanoparticles with giant coercivity*, J. Phys. D: Appl. Phys. 38 (2005) 2306.

[*Ege05*] R. F. Egerton, *Physical principles of electron microscopy*, Springer (2005). (book)

[*Eur14*] European Commission, *Report on critical raw materials for the EU* (2014).

[*Fec95*] H. J. Fecht, *Nanostructure formation by mechanical attrition*. Nanostruct. Mater. 6 (1995) 33.

[*Fen91*] X. Feng and H. W. Wang, *Intrinsic properties of the ferromagnetic* $R_{14}Fe_{78}B_{8-x}C_x$ *compounds*, J. Magn. Magn. Mater. 94 (1991) 49.

[*Gab10*] A. M. Gabay, N. G. Akdogan, M. Marinescu, J. F. Liu and G. C. Hadjipanayis, *Rare earth-cobalt hard magnetic nanoparticles and nanoflakes by high-energy milling*, J. Phys.: Condens. Matter 22 (2010) 164213.

[*Gar00*] L. M. García, J. Chaboy and F. Bartolomé, *Orbital magnetic moment instability at the spin reorientation transition of* $Nd_2Fe_{14}B$, Phys. Rev. Lett. 85 (2000) 429.

[*Get08*] M. Getzlaff, *Fundamentals of magnetism*, Springer, (2008). (book)

[*Giv84*] D. Givord, H. S. Li, and J. M. Moreau, *Magnetic properties and crystal structure of* $Nd_2Fe_{14}B$, Solid State Commun. 50 (1984) 497.

[*Giv92*] D. Givord, M. F. Rossignol, D. W. Taylor and A. E. Ray, *Coercivity analysis in Sm(Co, Cu, Fe, Zr)$_{7\text{-}8}$ magnets***,** J. Magn. Magn. Mater. 104-107 (1992) 1126.

[*Grö86*] R. Grössinger, X. K. Sun, R. Eibler, K. H. J. Buschow and H. R. Kirchmayr, *Temperature dependence of anisotropy fields and initial susceptibilities in* $R_2Fe_{14}B$ *compounds*, J. Magn. Magn. Mater. 58 (1986) 55.

[*Grö90*] R. Grössinger, X. C. Kou, R. Krewenka, H. R. Kirchmayr and M. Tokunaga, *Studies on* $Nd(Fe_{0.92-x}B_{0.08}Ga_x)_{5.5}$ *sintered permanent magnets*, IEEE Trans. Magn. 26 1954 (1990) 563.

[*Gut00*] O. Gutfleisch, D. Eckert, R. Schäfer, K. -H. Müller and V. Panchanathan, *Magnetization processes in two different types of anisotropic, fully dense NdFeB hydrogenation, disproportionation, desorption, and recombination magnets*, J. Appl. Phys. 87 (2000) 6119.

[*Gut03*] O. Gutfleisch, K. Khlopkov, A. Teresiak, K. -H. Müller, G. Drazic, C. Mishima and Y. Honkura, *Memory of texture during HDDR processing of NdFeB*, IEEE Trans. Magn. 39 (2003) 2926.

[*Gut06*] O. Gutfleisch, K. -H. Müller, K. Khlopkov, M. Wolf, A. Yan, R. Schäfer, T. Gemming and L. Schultz, *Evolution of magnetic domain structures and coercivity in high performance SmCo 2:17-type permanent magnets*, Acta Materialia, 54 (2006) 997.

[*Gut11*] O. Gutfleisch, M. A. Willard, E. Bruck, C. H. Chen, S. G. Sankar and J. P. Liu, *Magnetic Materials and Devices for the 21st Century: Stronger, Lighter, and More Energy Efficient*, *Adv. Mater.* 23 (2011) 821.

[*Güt11*] K. Güth, T. G. Woodcock, L. Schultz and O. Gutfleisch, *Comparison of local and global texture in HDDR processed Nd-Fe-B magnets*, Acta Materialia 59 (2011) 2029.

[*Gwm*] http://www.gwmg.ca

[*Haa85*] F. Haaf, A. Sanner and F. Straub, *Polymers of n-vinylpyrrolidone: synthesis characterization and uses*, J. Polymer 17 (1985) 143.

[*Had94*] G. C. Hadjipanayis and R. W. Siegel, *Nanophase materials: synthesis-properties-applications*. NATO ASI Series. 260 (1994). (book)

[*Har90*] I. R. Harris and P. J. McGuiness. In: Proc. of the 11th Int. workshop on rare-¬earth magnets and their applications. Pittsburgh (1990) 29.

[*Her14*] F. Herranz, B. Salinas, H. Groult, J. Pellico, A. V. Lechuga-Vieco, R. Bhavesh and J. Ruiz-Cabello, *Superparamagnetic Nanoparticles for Atherosclerosis Imaging*, Nanomaterials 4 (2014) 408.

[*Her75*] C. Herget and R G. Domazer, Goldschmidt informiert 35 (1975) 3-33.

[*Her90*] G. Herzer, *Grain size dependence of coercivity and permeability in nanocrystalline ferromagnets*, IEEE trans. Magn. 26 (1990) 1397.

[*Her91*] J. F. Herbst, *$R_2Fe_{14}B$ materials: intrinsic properties and technological aspects*, Rev. Mod. Phys. 63 (1991) 819.

[*Hir86*] S. Hirosawa, Y. Matsuura, H. Yamamoto, S. Fujimura, M. Sagawa and H.Yamauchi, *Magnetization and magnetic anisotropy of $R_2Fe_{14}B$ measured on single crystals*, J. Appl. Phys. 59 (1986) 873.

[*Hsp*] http://www.panalytical.com/Xray-diffraction-software/HighScore-with-Plus-option.htm

[*Hua09*] S. Huang, S. Zhang, T. Belytschko, S. S. Terdalkar and T. Zhu, *Mechanics of nanocrack: Fracture, dislocation emission, and amorphization*, J. Mech. Phys. Solids 57 (2009) 840.

[*Hub02*] A. T. Hubbard, *Encyclopedia of Surface and Colloid Science – Vol. 1*, CRC Press (2002). (book)

[*Hub09*] A. Hubert and R. Schäfer, *Magnetic Domains*, Springer (2009). (book)

[*Hur10*] C. Hurst, *China's rare earth element industry: what can the west learn*, Institute for the analysis of global security (IAGS), March 2010.

[*Idr04*] H. Idriss, *Ethanol reactions over the surfaces of noble metal/cerium oxide catalysts*, Platinum Metals Rev. 48 (2004) 105.

[*Jia01*] J. Jiang, Z. Zheng, J. Yu, J. Wu and M. Tokunaga, *The effect of cobalt addition on the fracture strength of NdFeB sintered magnets*, Intermetallics 9 (2001) 269.

[*Jia04*] B. Jiang and G. J. Weng, *A theory of compressive yield strength of nano-grained ceramics*, Int. J. Plast. 20 (2004) 2007.

[*Jai05*] T. K. Jain, M. A. Morales, S. K. Sahoo, D. L. Leslie-Pelecky and V. Labhasetwar, *Iron oxide nanoparticles for sustained delivery of anticancer agents*, Mol. Pharm. 2 (2005) 194.

[*Kac95*] W. A. Kaczmarek and B. W. Ninham, *Surfactant-assisted ball milling of $BaFe_{12}O_{19}$ ferrite dispersion*, Mater. Chem. Phys. 40 (1995) 21.

[*Kah93*] O. Kahn, *Molecular magnetism*, VCH publishers, Inc. (1993). (book)

[*Kel05*] R. W. Kelsall, I. W. Hamley and M. Geoghegan, *Nanoscale Science and Technology*, John Wiley & Sons, Ltd, (2005) (book)

[*Kim99*] G. Kimmel and D. Dayan, *X-ray diffraction broadening effects in material characterization*, in book: R. Synder, J. Fiala, H. J. Bunge, *Defect and Microstructure analysis by diffraction*, Oxford University Press (2000). (book)

[*Kir96*] E. M. Kirkpatrick, S. A. Majetich and M. E. McHenry, *Magnetic properties of single domain samarium cobalt nanoparticles*, IEEE Trans. Magn. 32 (1996) 4502.

[*Kit46*] C. Kittel, *Theory of the structure of ferromagnetic domains in films and small particles*, Phys. Rev. 70 (1946) 965.

[*Kne91*] E. F. Kneller and R. Hawig, *The Exchange-Spring Magnet: A new material principle for permanent magnets*, IEEE Trans. Magn. 27 (1991) 3588.

[*Knu11*] S. J. Knutson, Y. Shen, J. C. Horwath, P. Barnes, and C. H. Chen, *The effect of flake thickness on anisotropic $SmCo_5$ nanoflakes/submicron-flakes with high energy product*, J. Appl. Phys. 109 (2011) 07A762.

[*Kod99*] R. H. Kodama, *Magnetic nanoparticles*, J. Magn. Magn. Mater. 200 (1999) 359.

[*Kok11*] A. Kokalj, *Electrostatic model for treating long-range lateral interactions between polar molecules adsorbed on metal surfaces*, Phys. Rev. B 84 (2011) 045418.

[*Kot11*] N. Kotake, M. Kuboki, S. Kiya and Y. Kanda, *Influence of Dry and Wet Grinding Conditions on Fineness and Shape of Particle Size Distribution of Product in a Ball Mill*, Adv. Pow. Techn. 22 (2011) 86.

[*Kou89*] X. C. Kou, X. K. Sun, Y. C. Chuang, R. Grössinger and H. R. Kirchmayr, *Structure and magnetic properties of* $R_2Fe_{14}B_{1-x}C_x$ *compounds (R=Y, Nd)*, J. Magn. Magn. Mater. 80 (1989) 31.

[*Kou97*] X. C. Kou, M. Dahlgren, R. Grössinger and G. Wiesinger, *Spin-reorientation transition in nano-, micro- and single-crystalline* $Nd_2Fe_{14}B$, J. Appl. Phys. 81 (1997) 4428.

[*Kub82*] O. Kubaschewski, *Iron binary phase diagrams*, Springer Verlag, Berlin (1982). (book)

[*Kuz14*] M. D. Kuz'min, K. P. Skokov, H. Jian, I. Radulov and O. Gutfleisch, *Towards high performance permanent magnets without rare earths*, J. Phys.: Condens. Matter 26 (2014) 064205.

[*Lee08*] J. I. Lee, H. W. Kwon and Y. S. Kang, *Preparation of* $Nd_2Fe_{14}B$ *single domain particles from Nd-Fe-B alloy ingot using a combination of HDDR and mechanical milling*, J. Magn. 13 (2008) 102.

[*Lew12*] L. H. Lewis and F. J. Villacorta, *Perspectives on Permanent Magnetic Materials for Energy Conversion and Power Generation*, Metall. Mater. Trans. A 44 (2013) 2.

[*Lew14*] L. H. Lewis, J. E. Shield and K. Barmak, *Rare earth-free permanent magnetic material*, US Patent Application No. 14/232,830, July 2014.

[*Lew14a*] L. H. Lewis, A. Mubarok, E. Poirier, N. Bordeaux, P. Manchanda, A. Kashyap, R. Skomski, J. Goldstein, F. E. Pinkerton, R. K. Mishra, R. C. Kubic and K. Barmak, *Inspired by nature: investigating tetrataenite for permanent magnet applications*, J. Phys.: Condens. Matter 26 (2014) 064213.

[*Lid09*] D. R. Lide, *CRC Handbook of Chemistry and Physics, 89th Edition,* CRC Press/Taylor and Francis, Boca Raton, FL, (2009). (book)

[*Lie98*] S. Liesert, A. Kirchner, W. Grunberger, A. Handstein, P. Rango, D. Fruchart and L. Schultz, *Preparation of anisotropic NdFeB magnets with different Nd contents by hot deformation (die-upsetting) using hot-pressed HDDR powders*, J. Alloy Compd. 266 (1998) 260.

[*Liu11*] J. P. Liu, E. Fullerton, O. Gutfleisch and D. J. Sellmyer, *Nanoscale magnetic materials and applications,* Springer (2011). (book)

[*Liv81*] J. D. Livingston, *A review of coercivity mechanisms*, J. Appl. Phys. 52 (1981) 2544.

[*Low10*] M. Lowe, R. Golini and G. Gereffi, *U.S. adoption of high-efficiency motors and drives: lessons learned*, Center on Globalization, Governance & Competitiveness, Duke University (2010).

[*Lyu05*] J. Lyubina, I. Opahle, K. -H. Mueller, O. Gutfleisch, M. Richter, M. Wolf, L. Schultz, *Magnetocrystalline anisotropy in* $L1_0$ *FePt and exchange-coupling in FePt/*Fe_3Pt *nanocomposites*, J. Phys.: Condens. Matter 17 (2005) 4157.

[*Mat06*] Y. Matsuura, *Recent development of Nd-Fe-B sintered magnets and their applications*, J. Magn. Magn. Mater. 303 (2006) 344.

[*Mat85*] Y. Matsuura, S. Hirosawa, H. Yamamoto, S. Fujimura and M. Sagawa, *Phase diagram of the Nd-Fe-B ternary system*, Jpn. J. Appl. Phys. 24 (1985) L635.

[*Men03*] V. P. Menushenkov and A. G. Savchenko, *Effects of post-sintering annealing on magnetic properties of Nd-Fe-B sintered magnets*, J. Magn. .Magn. Mater. 258-259 (2003) 558.

[*Mie07*] S. L. Mielke, T. Belytschko and G. C. Schatz, *Nanoscale Fracture Mechanics*, Annu. Rev. Phys. Chem. 58 (2007) 185.

[*McG90a*] P. J. McGuiness, X. J. Zhang, X. У. Yin and I. R. Harris, *Hydrogenation, disproportionation and desorption (HDD): An effective processing route for* $Nd_2Fe_{14}B$*-type magnets*, J. Less Common Metals 158 (1990) 359.

[*McG90b*] P. J. McGuiness, X. J. Zhang, H. Forsyth and I. R. Harris, *Disproportionation in* $Nd_{16}Fe_{76}B_8$*-type hydrides*, J. Less Common Metals 162 (1990) 379.

[*Mis31*] T. Mishima, Stahl u. Eisen, 53 (1931) 79.

[*Mpi*] http://www.mpie.de/index.php?id=3356

[*Nan07*] V. Nandwana, K. E. Elkins, N. Poudyal, G. S. Chaubey, K. Yano, and J. P. Liu, *Size and shape control of monodisperse FePt nanoparticles*, J. Phys. Chem. C 111 (2007) 4185.

[*Nee62*] J. Needham, *Science and Civilization in China. Vol. 4: 1*, Cambridge University Press (1962). (book)

[*Nèe64*] L. Nèel, L. Pauleve´, R. Pauthenet, J. Laugier and D. Dautreppe, *Magnetic properties of an iron-nickel single crystal ordered by neutron bombardment*, J. Appl. Phys. 35 (1964) 873.

[*Nes59*] E. A. Nesbitt, J. H. Wernick and E. Corenzwit, *Magnetic moments of alloys and compounds of iron and cobalt with rare earth metal additions*, J. Appl. Phys. 30 (1959) 365.

[*Ode02*] S. Odenbach, *Ferrofluids-magnetically controllable fluids and their applications*, Springer, Berlin (2002). (book)

[*Pal10*] S. K. Pal and D. Bahadur, *Shape controlled synthesis of iron-cobalt alloy magnetic nanoparticles using soft template method*, Mater. Lett. 64 (2010) 1127.

[*Pal13*] S. K. Pal, K. Güth, T. G. Woodcock, L. Schultz and O. Gutfleisch, *Properties of isolated single crystalline and textured polycrystalline nano/sub-micron* $Nd_2Fe_{14}B$ *particles obtained from milling of HDDR powder*, J. Phys. D: Appl. Phys. 46 (2013) 375004.

[*Pou04*] N. Poudyal, B. Altuncevahir, V. Chakka, K. Chen, T. D. Black, J. P. Liu, Y. Ding and Z. L. Wang, *Field-ball milling induced anisotropy in magnetic particles,* J. Phys. D: Appl. Phys. 37 (2004) L45.

[*Pou10*] N. Poudyal, C. B. Rong and J. P. Liu, *Effects of particle size and composition on coercivity of Sm-Co nanoparticles prepared by surfactant-assisted ball milling*, J. Appl. Phys. 107 (2010) 09A703.

[*Pou11*] N. Poudyal, V. N. Vuong, C. B. Rong and J. P. Liu, *Anisotropic bonded magnets fabricated via surfactant-assisted ball milling and magnetic-field processing*, J. Phys. D: Appl. Phys. 44 (2011) 335002.

[*Pou13*] N. Poudyal and J. P. Liu, *Advances in nanostructured permanent magnets research,* J. Phys. D: Appl. Phys. 46 (2013) 043001.

[*Ram88*] R. Ramesh, G. Thomas and B. M. Ma, *Magnetization reversal in nucleation controlled magnets. II. Effect of grain size and size distribution on intrinsic coercivity of Fe-Nd-B magnets*, J. Appl. Phys. 64 (1988) 6416.

[*Rie69*] H. M. Rietveld, *A profile refinement method for nuclear and magnetic structures*, J. Appl. Cryst. 2 (1969) 65.

[*Ron10a*] C. B. Rong, V. V. Nguyen and J. P. Liu, *Anisotropic nanostructured magnets by magnetic-field-assisted processing,* J. Appl. Phys. 107 (2010) 09A717.

[*Ron10b*] C. B. Rong, Y. Zhang, N. Poudyal, X. Xiong, M. J. Kramer and J. P. Liu, *Fabrication of bulk nanocomposite magnets via severe plastic deformation and warm compaction*, Appl. Phys. Lett. 96 (2010) 102513.

[*Ron10c*] C. B. Rong, N. Poudyal and J. P. Liu, *Size-dependent spin-reorientation transition in* $Nd_2Fe_{14}B$ *nanoparticles*, Phys. Lett. A 374 (2010) 3967.

[*Ron11*] C. B. Rong, Y. Zhang, N. Poudyal, D. Wang, M. J. Kramer, and J. P. Liu, *Bulk* $SmCo_5/\alpha$*-Fe nanocomposite permanent magnets fabricated by mould-free joule-heating compaction*, J. Appl. Phys. 109 (2011) 07A735.

[*Ros85*] R. E. Rosensweig, *Ferrohydrodynamics*, Cambridge University Press, Cambridge, U.K. (1985). (book)

[*Row76*] G. Rowlands, *The variation of coercivity with particle size,* J. Phys. D: Appl. Phys. 9 (1976) 1276.

[*Rui08*] X. Rui, J. E. Shield, Z. Sun, R. Skomski, Y. Xu, D. J. Sellmyer, M. J. Kramer and Y. Q. Wu, *Intra-cluster exchange-coupled high-performance permanent magnets*, J. Magn. Magn. Mater. 320 (2008) 2576.

[*Sai98*] T. Saito, M. Fujita, T. Kuji, K. Fukuoka, and Y. Syono, *The development of high performance Nd-Fe-Co-Ga-B die upset magnets,* J. Appl. Phys. 83 (1998) 6390.

[*Sag84*] M. Sagawa, S. Fujimura, N. Togawa, H. Yamamoto, and Y. Matsuura, *New material for permanent magnets on a base of Nd and Fe*, J. Appl. Phys. 55 (1984) 2083.

[*Sar07*] P. Saravanan, R. Gopalan, N. V. R. Rao, M. M. Raja, and N. V. Chandrasekaran, $SmCo_5$*/Fe nanocomposite magnetic powders processed by magnetic field-assisted ball milling with and without surfactant*, J. Phys. D: Appl. Phys. 40 (2007) 5021.

[*Saw11*] S. Sawatzki, R. Heller, C. Mickel, M. Seifert, L. Schultz and V. Neu, *Largely enhanced energy density in epitaxial* $SmCo_5/Fe/SmCo_5$ *exchange spring trilayers*, J. Appl. Phys. 109 (2011) 123922.

[*Sch90*] J. Schneider, D. Eckert, K.-H. Müller, A. Handstein, H. Mühlbach, H. Sassik, H.R. Kirchmayr, *Magnetization processes in* $Nd_4Fe_{77}B_{19}$ *permanent magnetic materials*, Mater. Lett. 9 (1990) 201.

[*Sch90a*] C. M. Schneider, P. Bressler, P. Schuster and J. Kirschner, *Curie temperature of ultrathin films of fcc-cobalt epitaxially grown on atomically flat Cu(100) surfaces*, Phys. Rev. Lett. 64 (1990) 1059.

[*Sim11*] K. Simeonidis, C. Sarafidis, E. Papastergiadis, M. Angelakeris, I. Tsiaoussis and O. Kalogirou, *Evolution of* $Nd_2Fe_{14}B$ *nanoparticles magnetism during surfactant-assisted ball-milling*, Intermetallics 19 (2011) 589.

[*Sko01*] R. Skomski, *Micromagnetic spin structure*. In: M. Ziese, M. J. Thornton (eds.) Spin electronics, lecture notes in physics. Springer, Berlin (2001) 204. (book)

[*Sko93*] R. Skomski and J. M. D. Coey, *Giant energy product in nanostructured two-phase magnets*, Phys. Rev. B 48 (1993) 15812.

[*Sko99*] R. Skomski and J. M. D. Coey, *Permanent magnetism*, Institute of physics publishing Ltd. (1999). (book)

[*Spa11*] N. A. Spaldin, Magnetic materials: *Fundamentals and applications*, Cambridge university press (2011). (book)

[*Stä82*] H. Stäblein. *Hard Ferrites and Plastoferrites*. In: *Ferromagnetic materials*, edited by E. P. Wohlfarth, Amsterdam, North-Holland, (1982). (book)

[*Sug97*] S. Sugimoto, O. Gutfleisch and I. R. Harris, *Resistivity measurements on hydrogenation disproportionation desorption recombination phenomena in Nd-Fe-B alloys with Co, Ga and Zr additions*, J Alloy. Compd. 260 (1997) 284.

[*Sug06*] S. Sugimoto and D. Brook, *HDDR process for the production of high performance rare earth magnets.* In: Handbook of advanced magnetic materials Vol. 3, Tsinghua University Press, Springer (2006). (*book*)

[*Sur01*] V. Suryanarayana, *Mechanical alloying and milling*, Prog. Mater. Sci. 46 (2001) 1.

[*Sur04*] V. Suryanarayana, *Mechanical alloying and milling*, Marcel Dekker (2004). (book)

[*Tak89*] T. Takeshita, and A. Nakayama In:. Proc. of the 10th Int. workshop on rare-earth magnets and their applications. Kyoto, Japan, (1989) 551.

[*Tak90*] T. Takeshita and A. Nakayama. In: Proc. of the 11th Int. workshop on rare-earth magnets and their applications. Pittsburgh, USA, (1990) 49.

[*Tak00*] M. Takahashi and H. Shoji, *α-$Fe_{16}N_2$: giant magnetic moment or not?,* Philos. Mag. B 80 (2000) 215.

[*Thi12*] J. Thielsch, H. Stopfel, U. Wolff, V. Neu, T. G. Woodcock, K. Güth, L. Schultz, and O. Gutfleisch, *In situ magnetic force microscope studies of magnetization reversal of interaction domains in hot deformed Nd-Fe-B magnets*, J. Appl. Phys. 111 (2012) 103901.

[*Vas04*] L. S. Vasil'ev and S. F. Lomayeva, *On the analysis of mechanism of supersaturation of metal powders with interstitial impurities during mechanical activation*, J. Mater. Sci. 39 (2004) 5411.

[*Via02*] F. Vial, F. Joly, E. Nevalainen, M. Sagawa, K. Hiraga and K. T. Park, *Improvement of coercivity of sintered NdFeB permanent magnets by heat treatment*, J. Magn. Magn. Mater. 242-245 (2002) 1329.

[*Wan07a*] C. Wang, Y. Hou, J. Kim and S. Sun, *A General Strategy for Synthesizing FePt Nanowires and Nanorods*, Angew. Chem. Int. Edn. 46 (2007) 6333.

[*Wan07b*] Y. P. Wang, Y. Li, C. B. Rong and J. P. Liu, *Sm-Co hard magnetic nanoparticles prepared by surfactant-assisted ball milling*, Nanotechnology 18 (2007) 465701.

[*Wan12*] Y. Wang, X. Su and S. Lu, *Shape-controlled synthesis of TiO_2 hollow structures and their application in lithium batteries,* J. Mater. Chem. 22 (2012) 1969.

[*Web10*] W. Weber, *Springer Proceedings in Physics*, 133 (2010) 1. (book)

[*Wil53*] G. K. Williamson and W. Hall, *X-ray line broadening from filed aluminum and wolfram,* Acta Metallurgica 1 (1953) 22.

[*Wil09*] D. B. Williams and C. B. Carter, *Transmission Electron Microscopy: A Textbook for Materials Science*, Springer (2009). (book)

[*Woo14*] T. G.Woodcock, F. Bittner, T. Mix, K. -H. Müller, S. Sawatzki and O. Gutfleisch, *On the reversible and fully repeatable increase in coercive field of sintered Nd-Fe-B magnets following post sinter annealing*, J. Magn. Magn. Mater. 360 (2014) 157.

[*WWW1*] *http://www.gitam.edu/eresource/Engg_Phys/semester_2/magnetic/types.htm*

[*WWW2*] *http://magician.ucsd.edu/essentials/WebBookse20.html*

[*Yam02*] T. Yamamoto, H. Inui and M. Yamaguchi, *Effects of lattice defects on hydrogen absorption-desorption pressures in* $LaNi_5$, Mater. Sci. Eng. A 329-331 (2002) 367.

[*Yan07*] M. -M. Yang, X. -H. Bao and W. -X. Li, *First Principle study of ethanol adsorption and formation of hydrogen bond on Rh(111) surface*, J. Phys. Chem. C 111 (2007) 7403.

[*Yan08*] H. Yang, D. Hasegawa, S. Ozaki, T. Sato, M. Takahashi and T. Ogawa, *Gram-scale synthesis of monodisperse Fe nanoparticles in one pot*, Scripta Materialia 58 (2008) 822.

[*Yek01*] M. Yekeler, A. Ozkan and L. G. Austin, *Kinetics of fine wet grinding in a laboratory ball mill*, Powder Technology 114 (2001) 224.

[*Yos96*] K. Yoshida, *Theory of magnetism*, 122 springer series in solid-state sciences, Springer-verlag (1996). (book)

[*You93*] R. A. Young, *The Rietveld method*, Oxford University Press, Oxford, UK, (1993). (book)

[*Yue09*] M. Yue, Y. P. Wang, N. Poudyal, C. B. Rong and J. P. Liu, *Preparation of Nd-Fe-B nanoparticles by surfactant-assisted ball milling technique*, J. Appl. Phys. 105 (2009) 07A708.

[*Zen02*] H. Zeng, J. Li, J. P. Liu, Z. L. Wang and S. Sun, *Exchange-coupled nanocomposite magnets by nanoparticle self-assembly*, Nature 420 (2002) 395.

[*Zha01*] Y. -P. Zhao, R. M. Gamache, G. -C. Wang, T. -M. Lu, G. Palasantzas and J. T. M. De Hosson,, *Effect of surface roughness on magnetic domain wall thickness, domain size, and coercivity*,” J. Appl. Phys. 89 (2001) 1325.

[*Zha07*] S. Zhang, H. Xu, J. Ni, H. Wang, Q. Bai and Y. Dong, *Effect of gallium addition on magnetic properties of* $Nd_2Fe_{14}B$*-based/α-Fe nanocomposite magnets*, J. Rare Earths 25 (2007) 74.

[*Zha10*] Y. Zhang, M. J. Kramer, C. Rong and J. P. Liu, *Microstructure and intergranular diffusion in exchange-coupled Sm-Co/Fe nanocomposites*, Appl. Phys. Lett. 97 (2010) 032506.

[*Zha98*] Z. D. Zhang, X. C. Kou and F. R. De Boer, *The spin reorientation in* $Nd_2Fe_{14}B$ *in the presence of inter-grain exchange-coupling*, J. Alloy Compd. 274 (1998) 274.

[*Zhe10*] L. Zheng, B. Cui, N. G. Akdogan, W. Li and G. C. Hadjipanayis, *Influence of octanoic acid on SmCo5 nanoflakes prepared by surfactant-assisted high-energy ball milling*, J. Alloy Compd. 504 (2010), 391.

[*Zhe11*] L. Zheng, B. Cui and G. C. Hadjipanayis, *Effect of different surfactants on the formation and morphology of* $SmCo_5$ *nanoflakes*, Acta Materialia 59 (2011) 6772.

List of Publications:

- S. K. Pal, L. Schultz and O. Gutfleisch, *´´Effect of milling parameters on $SmCo_5$ nanoflakes prepared by surfactant-assisted high energy ball milling*``, Journal of Applied Physics 113 (2013) 013913-8.
- S. K. Pal, K. Güth, T. G. Woodcock, L. Schultz and O. Gutfleisch, *´´Properties of isolated single crystalline and textured polycrystalline nano/sub-micron $Nd_2Fe_{14}B$ particles obtained from milling of HDDR powder*``, Journal of Physics D: Applied Physics 46 (2013) 375004-11.
- S. K. Pal, L. Schultz and O. Gutfleisch, *´´Structural and magnetic properties of heat-treated ultrafine single crystalline $Nd_2Fe_{14}B$ particles obtained by ball milling of d-HDDR powder``,* Scripta Materialia 78-79 (2014) 33-36.
- S. K. Pal, K.-H. Müller, L. Schultz and O. Gutfleisch, "*Influence of intergrain exchange-coupling on spin reorientation temperature of ultrafine $Nd_2Fe_{14}B$ particles*" under review in Journal of Magnetism and Magnetic Materials.